Ph.D. Thesis

Study on direct detection of low-frequency gravitational waves with pulsar timing array

Naoyuki Yonemaru

Graduate School of Science and Technology (GSST)
Kumamoto University

March 2020

Contents

Abstract

Gravitational waves (GWs) are ripples in space-time traveling at the speed of light predicted in general relativity. In 2015, GWs from two colliding black holes (BHs) with tens of solar masses were detected by the Laser Interferometer Gravitational-wave Observatory (LIGO). Moreover, LIGO and the Virgo interferometers detected GWs from the merger of a neutron star binary in 2017, that opened the era of multi-messenger astrophysics since their electromagnetic counterpart was identified due to precise localization of the GW source. Ground-based interferometers such as LIGO and Virgo are sensitive to GWs from compact binaries at relatively high frequencies of 10 Hz - 10 kHz, whereas GWs at lower frequencies could be but have never detected by the space-based interferometer, pulsar timing array (PTA) and searching for the B-mode polarization in the cosmic microwave background. In this thesis, we focus on detection of low-frequency GWs with PTA.

Currently, a few tens of millisecond pulsars with periods of less than 30 ms have been monitored to detect GWs. Sensitivity of PTA improves as the number of pulsars increases. However, searching for pulsars takes much time and is very computationally expensive since we need to resolve narrow pulses with high time resolution. We then introduce artificial neural network (ANN) which is one of machine learning methods to selection of pulsar candidates from radio continuum survey catalogs. In chapter 1, we describe the architecture and training method of ANNs constructed in this work, test performance of the trained networks and present pulsar candidates obtained from the unidentified objects in two radio continuum survey catalogs, the TIFR GMRT Sky Survey and NRAO VLA Sky Survey, by applying them.

Cosmic strings are one of detectable GW sources for PTA experiments. Cosmic strings are one-dimensional defects, which naturally arise in field theories as well as in scenarios of the early Universe based on superstring theory. They have enormous mass, so that strong GW bursts are emitted, in particular, from non-smooth structures such cusps, and their superposition forms the GW background (GWB). Although they have not been detected before, therefore, the detection of GWs with PTAs is powerful tool to test the existence and investigate nature of them. So far, the GWB from cosmic strings has been studied. However, their single sources also could be detected with PTAs so that, then, we search for them with the second Parkes PTA data release. In chapter 2, we detail the cosmic string, give a description of the data set used in this work and detection algorithm, and show our search results.

The main targets of PTA are inpiraling supermassive BH (SMBH) binaries. The frequency range of PTA of $10^{-9} - 10^{-7}$ Hz corresponds to orbital periods of SMBH binaries with the sub-pc orbital radii that means only the binaries in the late stage of the evolution could be proved. The evolution of SMBH binaries after the stage where the transfer of angular momentum by stars and gas is no longer effective to shrink their orbits is not well understood, this is called “the final parsec problem”, thus

observation of binaries in the earlier stage, or GWs at lower frequency, is meaningful. Our previous work [115] proposed a new detection method for such ultra-low-frequency GWs from a single source, and we estimate the expected sensitivity of our method quantitatively in chapter 3.

Chapter 1

Pulsar candidate selection from radio continuum surveys with artificial neural networks

1.1 Pulsar

Pulsars are rapidly-rotating neutron stars (NSs) that emit weak radio beams from their magnetic poles which can be seen as pulses with very stable periods when the directions of emission and line of sight coincide. There are several models of a mechanisms for pulsar radiation (e.g. the Goldreich-Julian model [45] which is the simplest one), but it is not still well understood. Here, NSs are partially supported by neutron degeneracy pressure described by the Pauli exclusion principle, and are the smallest with radii of about 10 km and densest objects expect black holes (BHs). They originate from the supernova explosions of massive stars with masses of 10 to 29 $M_\odot$ (solar mass). In this section, we describe features of the pulsars and the method to search for them briefly.

Categories

Since the discovery of the pulsar in 1968 [51], 2,800 pulsars were found. They have diversity which can be seen in the $P - \dot{P}$ diagram shown in Fig. 1.1. Most of normal pulsars are concentrated at a period of 1 sec, but there are some populations with characteristic features;

- **Millisecond pulsars (MSPs)**: Pulsars with periods of less than 30 ms. Most of these pulsars are binary systems, so that these are regarded as being re-cycled pulsars, having been "spun-up" by accreting matter from their companions. Currently, 360 MSPs were discovered and the majority of them are in globular clusters. MSPs with very stable periods are used for test of gravity theory and direct detection of gravitational waves (GWs) with pulsar timing array (PTA) mentioned in section 2.1.1.
- **Magnetars**: Pulsars with exceedingly strong magnetic fields of about 10^{15}G. They are observed with mainly X- and γ-rays. They are further categorized to the Anomalous X-Ray Pulsars

(AXPs) and the Soft Gamma-Ray Repeaters (SGRs). These were considered to be different objects before, but both of them have been confirmed to be pulsars at present.

- **Central compact objects (CCOs)**: Pulsars in the centers of young supernovae remnants emitting thermal X-ray. They can not be observed in other wavelengths and do not form binaries. Furthermore, since they do not have the pulsar wind nebulae, they are considered to be very young neutron stars so that have not begun to emit pulses.
- **Rotating Radio Transients (RRATs)**: Pulsars emitting pulses at intervals of from a few minutes to a few hours. Their pulse periods are generally longer than those of the normal ones.
- **Intermittent Pulsars**: Pulsars emitting pulses for a couple of days a month. The spin-down rate in the "turn-on" phase is larger than the "turn-off" phase, which implies that the radiant energy of pulsars originates in the rotational energy.

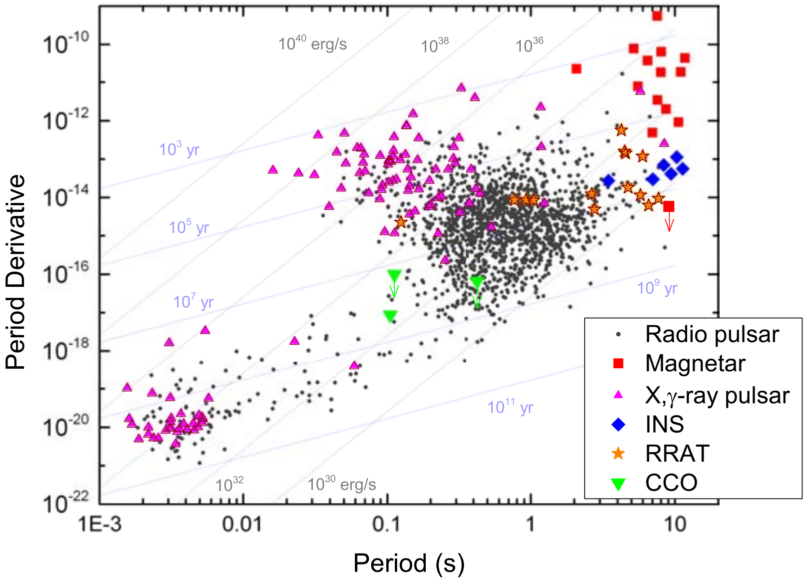

Figure 1.1: Pulsar distribution on the pulse period P-its time derivative, or the spin-down rate, $\dot{P}$ plane ($P - \dot{P}$ diagram) [49]. INS, RRAT and CCO stand for Isolated Neutron Star, Rotating Radio Transient and Central Compact Object, respectively.

Spin evolution

Pulse periods increase with time. The time derivative of the pulse period, or the spin-down rate, is considered to be given by the loss of the rotational energy

$$\dot{E} \equiv -\frac{dE_{\mathrm{rot}}}{dt} = -\frac{d}{dt}\frac{1}{2}I\Omega^2 = -I\Omega\dot{\Omega} = 4\pi^2 I\dot{P}P^{-3}, \tag{1.1}$$

where I is the moment of inertia and $\Omega = 2\pi/P$ is the angular frequency. This energy loss $\dot{E}$ is called "the spin-down luminosity" and describes the total energy emitted from a neutron star. For the moment of inertia of $I = 10^{45}$ g cm^2, the spin-down luminosity is given by

$$\dot{E} \simeq 3.95 \times 10^{31}\ \mathrm{erg\ s^{-1}} \left(\frac{\dot{P}}{10^{-15}}\right)\left(\frac{P}{\mathrm{s}}\right). \tag{1.2}$$

Most of this energy is translated into high energy radiation, the pulsar wind and especially the magnetic dipole radiation.

A dipole with the magnetic moment of $|\mathbf{m}|$ emits electromagnetic waves with a frequency same as its spin frequency. The luminosity emitted from a magnetic dipole is given by

$$\dot{E}_{\mathrm{dipole}} = \frac{2}{3c^3}|\mathbf{m}|^2\Omega^4 \sin^2\alpha, \tag{1.3}$$

where α is the angle between the dipole and spin axes. Assuming that this emissivity is equal to the spin-down luminosity (1.1), we get

$$\dot{\Omega} = -\left(\frac{2|\mathbf{m}|^2\sin^2\alpha}{3Ic^3}\right)\Omega^3. \tag{1.4}$$

With using the spin frequency $\nu = 1/P$, this equation could be generalized to the power law given by

$$\dot{\nu} = -K\,\nu^n, \tag{1.5}$$

where n is called "the braking index", and K is generally constant. Note that $n = 3$ corresponds to the dipole radiation. Practically, however, there would be other factors extracting the rotational energy, for example the pulsar wind which the energy loss by this is also given by the scaling law same as Eq. (1.5), so that we can not simplify the spin evolution as Eq. (1.5). Differentiating Eq. (1.5) and eliminating K, we can determine the braking index given by

$$n = \nu\ddot{\nu}/\dot{\nu}^2. \tag{1.6}$$

In general, it is hard to measure $\ddot{\nu}$ precisely. But, some have been measured, and the range of their braking indices is 1.4 - 2.9. This means that the assumption of $n = 3$, or the dipole radiation, is incorrect. Nevertheless, $n = 3$ is often used since it is useful to characterize radio pulsars.

Characteristic age

Eq. (1.5) is expressed as $\dot{P} = KP^{2-n}$ with using the pulse period P. This is the first order differential equation that allows us to integrate and obtain the age of a pulsar assuming that K is constant and $n \neq 1$. The pulsar age is given by

$$T = \frac{P}{(n-1)\dot{P}}\left[1 - \left(\frac{P_0}{P}\right)^{n-1}\right], \tag{1.7}$$

where P_0 is the initial pulse period. Under assumption that the initial period is much smaller than the present one and the spin-down is caused by the dipole radiation ($n = 3$), Eq. (1.7) could be simplified as

$$\tau_c \equiv \frac{P}{2\dot{P}} \simeq 15.8\ \mathrm{Myr}\left(\frac{P}{\mathrm{s}}\right)\left(\frac{\dot{P}}{10^{-15}}\right)^{-1}. \tag{1.8}$$

This τ_c is called "the characteristic age" and gives rough estimate of the pulsar's age.

Magnetosphre

If radiation from pulsars is the magnetic dipole radiation, measurement of P and $\dot{P}$ gives estimate of the strength of the magnetic field at the surfaces of pulsars. With using the relation between the magnetic moment and the strength of the magnetic field of $B \approx |\mathbf{m}|/r^3$, Eq. (1.4) could be rewritten as

$$B_S \equiv B(r = R) = \sqrt{\frac{3c^3}{8\pi^2}\frac{I}{R^6 \sin^2\alpha}P\dot{P}}. \tag{1.9}$$

For a pulsar with the moment of inertia of $I = 10^{45}$ g cm^2, radius of $R = 10$ km and $\alpha = 90°$, the strength of the magnetic field at the surface is given by

$$B_S = 3.2 \times 10^{19}\,\mathrm{G}\sqrt{P\dot{P}} \simeq 10^{12}\,\mathrm{G}\left(\frac{\dot{P}}{10^{-15}}\right)\left(\frac{P}{\mathrm{s}}\right). \tag{1.10}$$

Note that α is unknown and the radius and moment of inertia have uncertainties so that this strength is just an estimate.

1.1.1 Pulsar search

In the case that individual pulses from pulsars can be seen, pulsar search would be fairly easy since we should have to just look for objects which flush on and off in the sky. For most of pulsars, however, single pulses are not strong enough to detect individually and get buried in the background radio noise. Such weak pulses are detected by integrating or folding several hundred to thousand individual pulses using the fact that noise is a random process which partially cancels itself out in each fold. Besides long observation time (e.g. 30 - 60 minutes per a pointing), however, the folding requires the knowledge of the pulse period ahead of time. We then perform a Fourier transform to search for periodic signals, or obtain the pulse period.

Furthermore, we have another problem with observation of pulsars. Pulses from a pulsar suffer from the dispersion when they travel to Earth through the interstellar medium (ISM). By interacting with the free electrons in the ISM, pulses at higher frequencies travel faster than their lower frequency counterparts. Therefore, propagation through the ISM causes delay in arrival times of pulses depending on frequencies which is described as

$$\Delta t = 4.15 \times 10^6 (f_{\mathrm{low}}^{-2} - f_{\mathrm{high}}^{-2})\mathrm{DM}, \tag{1.11}$$

where f is the frequency, which smears the pulse profile. Here, DM is the dispersion measure that represents the integrated column density of free electrons along the line-of-sight to the pulsar, and is given by

$$\mathrm{DM} = \int_0^d n_e \, dl, \tag{1.12}$$

where d is the distance to the pulsar and n_e is the free electron density. This effect should be removed, which the process of dispersion removal is called “de-dispersion”, before performing the Fourier transform to find periodic signals. But, we do not have the knowledge of the DM ahead of time, thus we have to perform the de-dispersion for a large number of trial DM values when searching for new pulsars. Therefore, pulsar searching takes much time and is very computationally expensive.

So far, several blind surveys have been performed, e.g. the Parkes Multi-beam Pulsar Survey (PMPS) [82] and the Arecibo Pulsar using the Arecibo L-band Feed Array (PALFA) survey [29]. But, as mentioned above, those blind surveys have taken much observation time, e.g. 35 minutes per a pointing and the number of pointings is 2,670 in the region of $50^\circ \leq l \leq 260^\circ$ and $|b| \leq 5^\circ$ where l and b are the galactic longitude and latitude by the PMPS, and 17.1 hours for 919 points in the Galactic anticenter and 32.2 hours for 865 pointings in the inner Galaxy, covering 15.8 and 14.8 deg^2 in each region respectively by the PALFA survey.

Then, we introduce artificial neural networks (ANNs) described in section 1.3 in details to selection of pulsar candidates from radio continuum survey data.

1.2 Radio Source Catalog

In this section, we provide a description of the radio continuum surveys, the TIFR GMRT Sky Survey (TGSS) and NRAO VLA Sky Survey (NVSS), and a radio source catalog developed by [35] used in this work.

TGSS ADR1 - The TIFR GMRT Sky Survey [54] is a radio continuum survey at 147 MHz carried out with the Giant Metrewave Radio Telescope (GMRT). This survey covers the north sky of $\delta = -53^\circ$ visible from the GMRT (90 per cent of the celestial sphere). The resolution of this survey is $25''$ and the median rms noise is 3.5 mJy beam^{-1}. The overall astrometric accuracy is better than $2''$ in RA and Dec, while the flux density accuracy is estimated to be about 10 per cent for most of the survey area. The higher resolution of GMRT, combined with the data reduction strategy that down-weights the short baselines, reduced both the sensitivity of TGSS to extended emission as well as the presence of artefacts along the Galactic plane due to bright and extended sources. The largest detectable angular scale in TGSS is of order a few arcmin.

NVSS - The NRAO VLA Sky Survey [27] is a radio continuum survey at 1.4 GHz carried out with the Very Large Array (VLA). This survey covers the sky north of $\delta = -40^\circ$ (82 per cent of the celestial sphere). The survey was made with the Very Large Array (VLA) in D and DnC configurations in full polarization. However, for this work we used only Stokes I images. The resolution is $45''$ and the background rms noise is nearly uniform at 0.45 mJy beam^{-1}. The overall astrometric accuracy is better than $1''$ in RA and Dec. Due to the compactness of the VLA configuration used, the surface brightness of extended sources is fairly well reconstructed up to scales of about $16'$. At the same time, extended and unmodeled surface brightness from the Galactic plane lower the fidelity of images at low galactic latitude.

In [35], radio sources are cross-matched and objects with a separation less than $15''$ are regarded as the same object. Besides these cross-matched sources, we use radio sources detected by only the

TGSS as well. This is because pulsars with steep spectra could be dimmer than the detection limit of the NVSS and appear only in the TGSS catalog. For these sources, we allocate the upper bound on the NVSS flux and spectral index. Hereafter, we call these objects ("S", "M" and "U" in [35]) the "Gasperin catalog" and it has 470,052 sources.

In order to construct ANNs, we need training data set with radio sources which are already known to be pulsars or non-pulsars, which this approach is categorized as supervised machine learning. To extract pulsars from the Gasperin catalog, we cross-match it with the ATNF pulsar catalogue [81] and 127 sources are identified as pulsars. The ATNF pulsar catalogue consists of 2,253 normal pulsars and 360 millisencond pulsars, whereas our training data includes 107 normal ones and 20 millisencond ones. Although the ratio of pulsars in the training data to the whole pulsars in the ATNF pulsar catalogue is just 4.9%, there is not significant bias in the ratio of millisecond pulsars to normal pulsars in the training data. The Gasperin catalog is further cross-matched with the Million Quasar (MILLIQUAS) catalog [40] which consists of various types of radio point sources such as AGN, quasars and BL Lac objects, and Seyfert galaxies (radio galaxies) which are mainly observed by the SDSS [7]. As a result, 13,166 sources are cross-matched and then identified as non-pulsars.

Fig. 1.2 shows the celestial distribution of the identified pulsars and non-pulsars in the galactic coordinate. The distribution of pulsars and non-pulsars are highly biased reflecting the survey region of the TGSS, NVSS and MILLIQUAS. Despite the bias of the survey region, we use these data sets as they are since unbiased data are currently unavailable. Fig. 1.3 shows the scatter plot of the TGSS and NVSS fluxes. We can see that pulsars have smaller NVSS flux than TGSS flux compared with non-pulsars and many of pulsars are not observed by the NVSS. This means that pulsars have steeper spectra, which can be confirmed in Fig. 1.4 which represents the histogram of spectral index. In these figures, pulsars and non-pulsars are clearly separated and these quantities will be useful to select pulsar candidates [80]. Fig. 1.5 shows the histogram of compactness. Although the distribution looks very similar for pulsars and non-pulsars, they can give some useful information when combined with other quantities.

1.3 Artificial neural networks

ANN is one of machine learning methods, which is a mathematical model inspired by human brain and has recently been attracting much attention. The purpose of ANN is to construct a suitable network, or optimize the network parameters with training data set (x_i, t_k) where x_i and t_k are the input and correct output, respectively. In our case, x_i represents observed quantities which characterize a radio source such as flux, spectral index, sky position and compactness, while t_k is unity/zero for a pulsar/non-pulsar, respectively. In this work, we employ the simplest case of the multilayer perceptron with three layers because of the relatively small number of input quantities mentioned above.

In this section, we describe the network architecture and the process of optimizing the network parameters (the training process) briefly.

1.3.1 Architectures

We consider ANNs which consist of three layers: the input, hidden and output layers. Each layer has neurons which are described as x_i, y_j and z_k, respectively. Here, a neuron is the basic element of

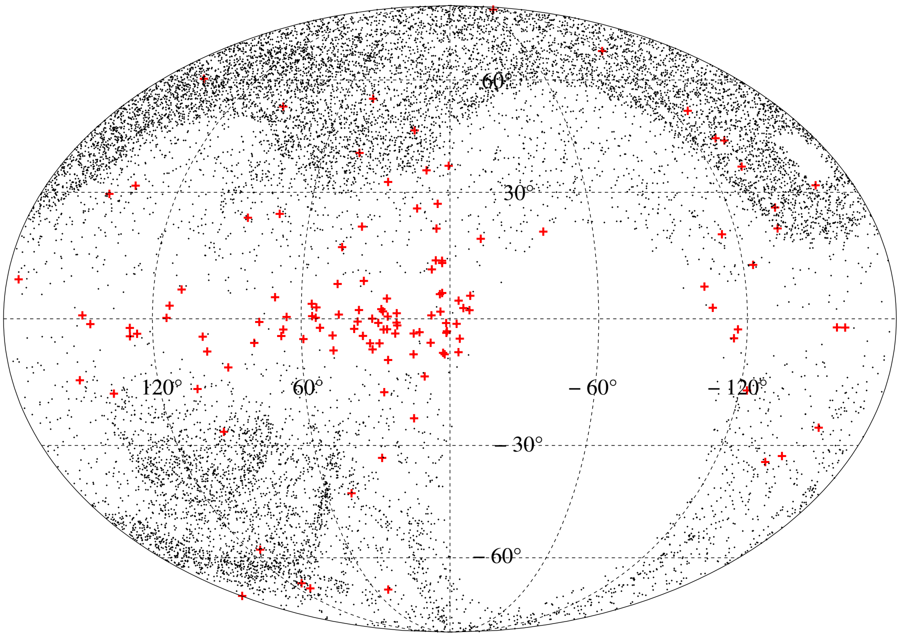

Figure 1.2: Distribution of pulsars and non-pulsars in the galactic coordinate. The red and black crosses represent the position of pulsars and non-pulsars, respectively. Objects observed by only the TGSS are given the upper limit of 2.5mJy as the NVSS flux.

an ANN which generates one output from multiple inputs. An output from a neuron in the hidden layer, y_j, is written as

$$y_j = f(u_j), \tag{1.13}$$

where u_j is given by a linear combination of the input x_i and weight $w_{ij}^{(1)}$ and the bias $b_j^{(1)}$ as,

$$u_j = \sum_i x_i \cdot w_{ij}^{(1)} + b_j^{(1)}. \tag{1.14}$$

Here, $f(x)$ is the activation function and we adopt the sigmoid function, which is used commonly in the field of ANNs, given by

$$f(u_j) = \frac{1}{1 + \exp(-u_j)}. \tag{1.15}$$

In the output layer, an output z_k is written as

$$z_k = g(v_k), \tag{1.16}$$

where v_k is given by a linear combination of the output from the hidden layer y_j and weight $w_{jk}^{(2)}$ and the bias $b_k^{(2)}$ as,

$$v_k = \sum_j y_j \cdot w_{jk}^{(2)} + b_k^{(2)}. \tag{1.17}$$

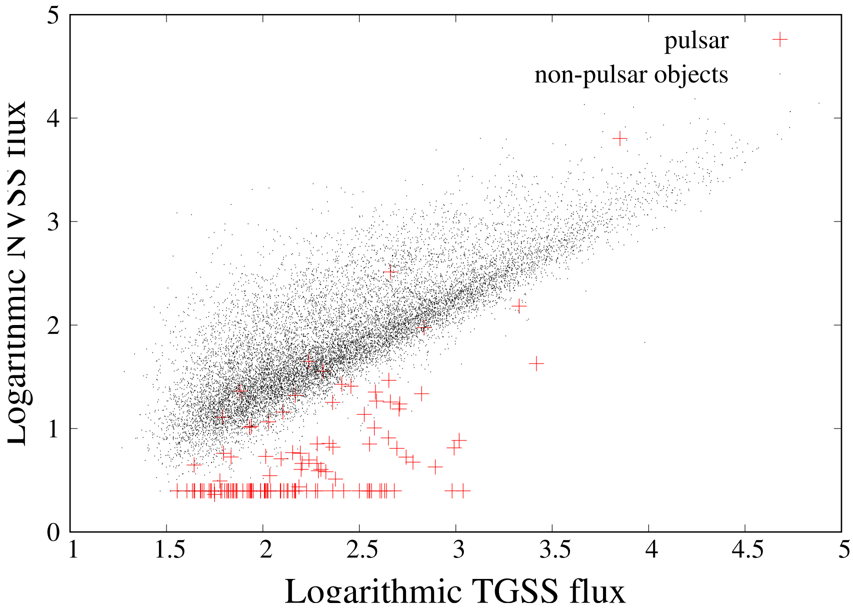

Figure 1.3: Scatter plot of the TGSS and NVSS fluxes. The red crosses and black dots correspond to pulsars and non-pulsar objects, respectively.

We adopt the softmax function as the activation function in the output layer in this paper

$$g(v_k) = \frac{\exp(v_k)}{\sum_m \exp(v_m)}, \tag{1.18}$$

which is commonly used for classification problems. In our case, the values of z_k for $k = 1$ and 2 represent the scores which are degrees of resemblance of the source to a pulsar and non-pulsar, respectively.

Here we note that, although our network includes only one hidden layer, any functional form could be approximated as long as non-linear functions are used as the activation functions and the hidden layer consists of a sufficient number of neurons. This fact is known as the universal approximation theorem [30, 53].

1.3.2 Training

Appropriate values of the network parameters (the weights and biases) are searched by minimizing the loss function (or the cost function) and this process is called "training". The loss function characterizes difference between z_k obtained from the network and the correct value t_k. In the classification problem, the cross entropy error is often used and defined as

$$CE = -\frac{1}{N}\sum_n^N \sum_k t_{n,k} \log z_{n,k}, \tag{1.19}$$

where $n = 1, \cdots, N$ is the number of training data. In the process of training, we need to avoid "overfitting", where a network is too fitted for training data. There are several methods to suppress

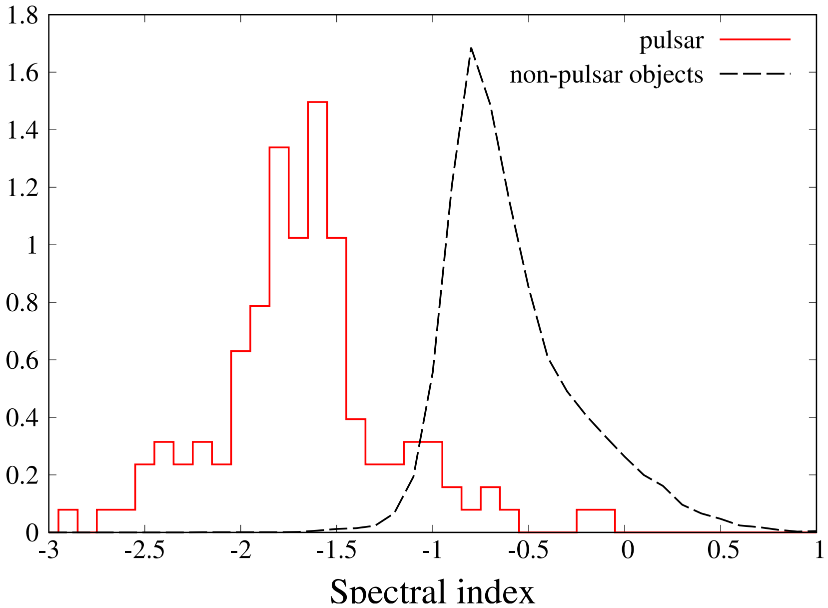

Figure 1.4: Histogram of spectral index calculated from the TGSS and NVSS fluxes. The red solid and black dashed lines correspond to pulsars and non-pulsar objects, respectively. This histogram includes upper limits for objects observed by only the TGSS.

overfitting, and we adopt the weight decay method for our ANNs. The weight decay is a method that imposes a penalty on the weights. In this work, the loss function is given by the sum of the cross entropy error and the sum of the squared weights,

$$L = -\frac{1}{N}\sum_{n}^{N}\sum_{k} t_{n,k}\log z_{n,k} + \frac{1}{2}\lambda\left[\sum_{i,j}\left(w_{ij}^{(1)}\right)^2 + \sum_{j,k}\left(w_{jk}^{(2)}\right)^2\right], \tag{1.20}$$

where λ is a hyper parameter called the “weight decay term” representing the penalty of the weight and is determined by a method explained in subsection 1.4.2.

The network parameters are optimized by the “Momentum” method described as follows. First, let $\xi(t) = (w_{ij}^{(1)}(t), b_j^{(1)}(t), w_{jk}^{(2)}(t), b_k^{(2)}(t))$ be the network parameters at t-th step of training. In the next step $t+1$, they are updated as

$$v(t+1) = \mu v(t) - \eta \left.\frac{\partial L}{\partial \xi}\right|_t, \tag{1.21}$$

$$\xi(t+1) = \xi(t) + v(t+1), \tag{1.22}$$

where η and μ are the learning rate and friction coefficient, which are fixed to 0.01 and 0.9, respectively. These two are also hyper parameters, so that they could be determined in the same way as λ. However, they affect only the efficiency of the training and not the performance of the network. Further, the number of training steps is also a hyper parameter and too many steps tend to induce overfitting. Thus, in addition to λ, we optimize the number of training steps by the method described in section

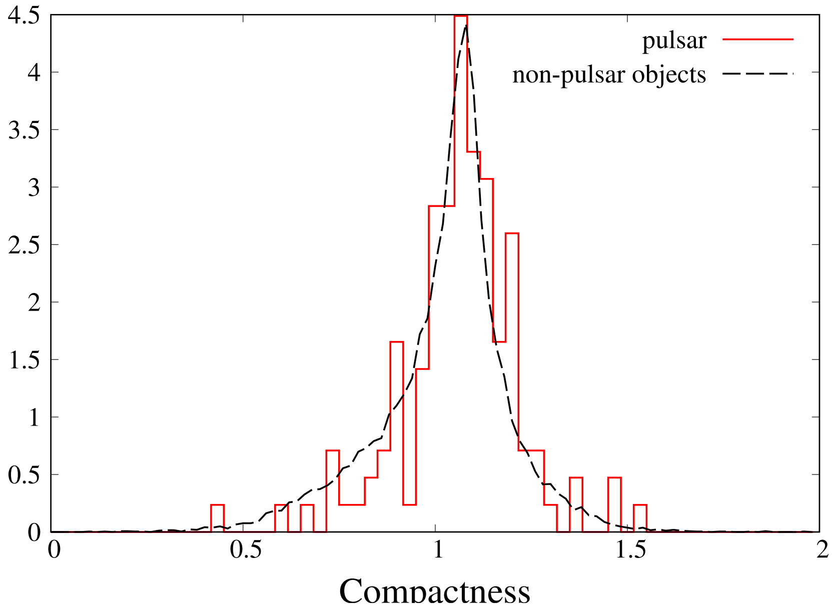

Figure 1.5: Histograms of the compactness. The red solid and black dashed lines correspond to pulsars and non-pulsar objects, respectively.

1.4.2 fixing η and μ. Here, the initial values of $v(t)$ and $\xi(t)$ are set to $v(0) = 0$ and random values with normal distribution of zero mean and standard deviation of 0.1, respectively. We evaluate the derivative of the loss function in Eq.(1.21) by the backpropagation algorithm [98], which is a very computationally efficient method.

The training process is summarized as follows:

1. Initialize the network parameters $(w_{ij}^{(1)}, b_j^{(1)}, w_{jk}^{(2)}, b_k^{(2)})$.
2. Compute output z_k with Eqs.(1.13) - (1.18), and then the loss function (1.20).
3. Compute the derivative of the loss function with respect to the weights, and update the network parameters according to Eqs.(1.21) and (1.22).
4. Go back to 2 and iterate the number of times determined by the method explained in section 1.4.2.

1.4 Implication of artificial neural networks for pulsar candidate selection

1.4.1 Input parameters

In this paper, we consider the following 7 quantities as the inputs:

(A) Galactic longitude l normalized to [-1:1].

(B) Galactic latitude b normalized to [-1:1].

These quantities (A) and (B) represent the sky position in the galactic coordinate. The majority of pulsars are expected to be located on the Galactic plane as can be seen from Fig. 1.2 since they are formed inside the Galaxy, while non-pulsar objects in the distance should distribute uniformly in the sky. Thus, these quantities are potentially informative for pulsar candidate selection.

(C) Absolute value of galactic latitude $|b|$ normalized to [0:1]. We consider this as an alternative to (B), because as mentioned above pulsars are located near the Galactic plane in the sky so that $|b|$ rather than b may be more useful.

(D) Logarithmic TGSS total flux [mJy] normalized so that the mean value is 0 and standard deviation is 0.5.

(E) Logarithmic NVSS total flux [mJy] normalized in the same way as (D). Here, objects below the detection limit of the NVSS are given the value of upper limit of 2.5 mJy.

(F) Spectral index α normalized in the same way as (D).

As we saw in Fig. 1.4, pulsars tend to have steep spectra [57, 55, 35]. Although the spectral index (F) is a direct measure of the steepness, the pair of quantities (D) and (E) have more information than the index and they are adopted in our fiducial network. They are specific to surveys we use in the current paper, but the fluxes at different frequencies could also be used if some other radio surveys are used. Note that a few pulsars have spectral energy distribution which breaks down at a few MHz [18, 87].

(G) Source compactness C normalized to [-1:1]. It is defined in [35] as,

$$C = \frac{1.071 + 2\sqrt{0.038^2 + 0.39^2\left(S_{\mathrm{peak}}/\sigma_l\right)^{-1.3}}}{S_{\mathrm{total}}/S_{\mathrm{peak}}}, \tag{1.23}$$

where S_{total}, S_{peak} and σ_l are the total flux, peak flux and local rms noise of the TGSS. Pulsars with radii of a few ten km are completely point sources, on the other hand, non-pulsar objects have much more extended structures than pulsars, but there is little difference between pulsars and non-pulsars as seen in Fig. 1.5. Nevertheless we consider this feature since it could have correlation with other features.

Then, four sets of the above quantities are taken as input parameters:

Case 1 (A), (B), (D), (E) and (G)

Case 2 (A), (B), (F) and (G)

Case 3 (A), (C), (D), (E) and (G)

Case 4 (A), (C), (F) and (G)

where Case 1 is our fiducial set and uses original quantities, rather than derived quantities such as (C) and (F). We set the number of neurons in the hidden layer as twice that of the input layer as our fiducial setup. Thus, the input, hidden and output layers have 5, 10 and 2 neurons for Cases 1 and 3, and 4, 8 and 2 neurons for Cases 2 and 4, respectively. We also investigate the networks with five and fifteen neurons in the hidden layer for Case 1 (See section 1.6).

1.4.2 Determination of Hyper-Parameters and Performance Test

In order to construct ANNs, we need to fix the values of hyper-parameters: the weight decay term λ and the number of training steps. In this subsection, we describe the method to determine these hyper-parameters following [38]. First, a subset is selected randomly from the whole data (x_i, t_k). Here the size of the subset is typically 10% of the whole data. The subset and remainder are called validation data and training data, respectively. Then, for a fixed value of λ, ANN is trained with the training data. At each step of training, the ANN is applied to the validation data and the cross entropy error is calculated between the correct value of t_k and the output from the ANN. The cross entropy error tends to decrease at first but eventually turns to increase after a large number of training steps, which indicates overfitting. Thus, it is reasonable to choose the number of steps with which the cross entropy error is minimum. We repeat this process varying the value of λ and choose both λ and the number of steps by comparing the minima of the cross entropy error. We vary the value of λ in the range of its $-10 \leq \log_{10}\lambda \leq -2$ and consider the case of $\lambda = 0$ as well. Finally, the ANN is trained once again with all data and hyper-parameters determined in the above way. The resultant ANN is now ready to be applied to unidentified radio sources to judge if they are likely to be a pulsar or not. It should be noted that timing observation is necessary to confirm whether the pulsar candidates are really pulsars or not.

In this paper, we will not only apply our ANNs to unidentified sources but also demonstrate the performance of our methodology. To do the performance test as well as cross validation, we need to divide the data into three subsets: training data, validation data and test data. In our performance test, we first construct ANNs with training and validation data in the above way, and then the ANNs are applied to the test data. We repeat this process basically 10 times changing the choice of the data sets randomly, which means that we make 10 independent ANNs, (Previously, only the validation and test data were mentioned, but we also chose the training data randomly.) and the performance is statistically checked, which is commonly called the “bootstrap” method.

As we stated in section 1.2, 127 pulsars and 13,166 non-pulsars were identified and they can be used as training, validation and test data. Although the ratio of the training data is unbalanced, we use 10,000 non-pulsars for training. We try cases with 200, and 1,000 non-pulsars as well to see the effect of imbalance of the training data sets. The numbers of pulsars and non-pulsars in training, validation and test data are summarized in Table 1.1.

1.5 Results

1.5.1 Performance test

First, we show the results of performance tests of our ANNs. Fig. 1.6 represents the hyper-parameters determined by the method mentioned in section 1.4.2 for Case 1. Although the distribution of hyper-

Table 1.1: Numbers of samples in the training, validation and test data. The fiducial number of non-pulsar objects in the training data is 10,000 but it is varied as 200 and 1,000.

	Total	Training	Validation	Test
Pulsar	127	107	10	10
Non-pulsar objects	13,166	10,000	100	1,000
		others	100	100

parameters seems diverge, the numbers of training steps are chosen between 10^5 and 10^6 for all of the 10 networks, while the weight decay term λ tends to be less than 10^{-4}.

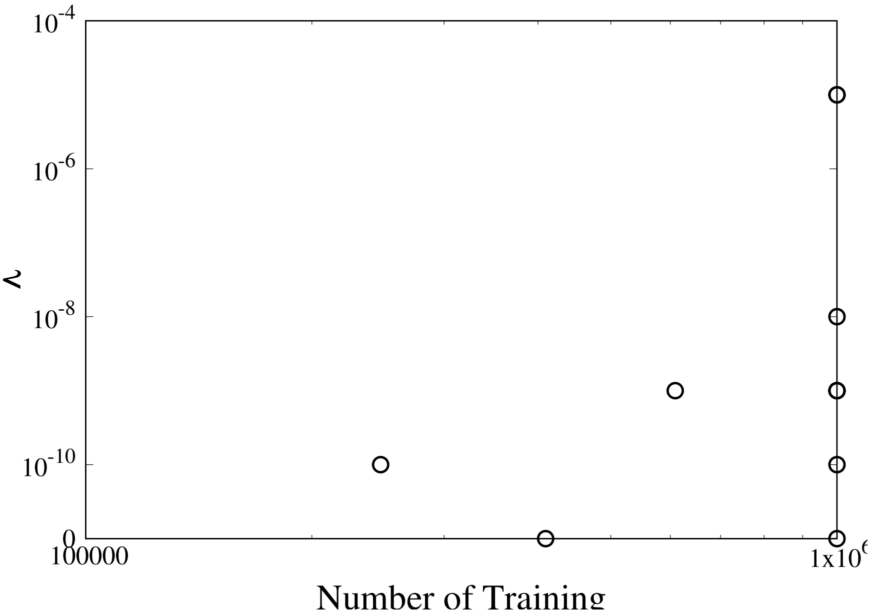

Figure 1.6: Scatter plot of two hyper-parameters, number of training steps and the weight decay term λ, determined by the method mentioned in section 1.4.2 for Case 1. The thick symbols, (10^6, 10^{-5}) and (10^6, 10^{-9}), represent where the hyper-parameters are chosen twice.

Next, we show the test results of trained networks. The outputs of our ANNs are the scores z_1 and z_2 that the input object is a pulsar z_1 and non-pulsar object, respectively, where the sum of them is normalized to unity. Fig. 1.7 shows the histogram of z_1 of the test data obtained from all of the 10 trained ANNs for Case 1. As can be seen, the value of z_1 is almost zero or unity for most objects.

To determine the criterion of z_1 that classifies objects into the pulsars or non-pulsars, we use the

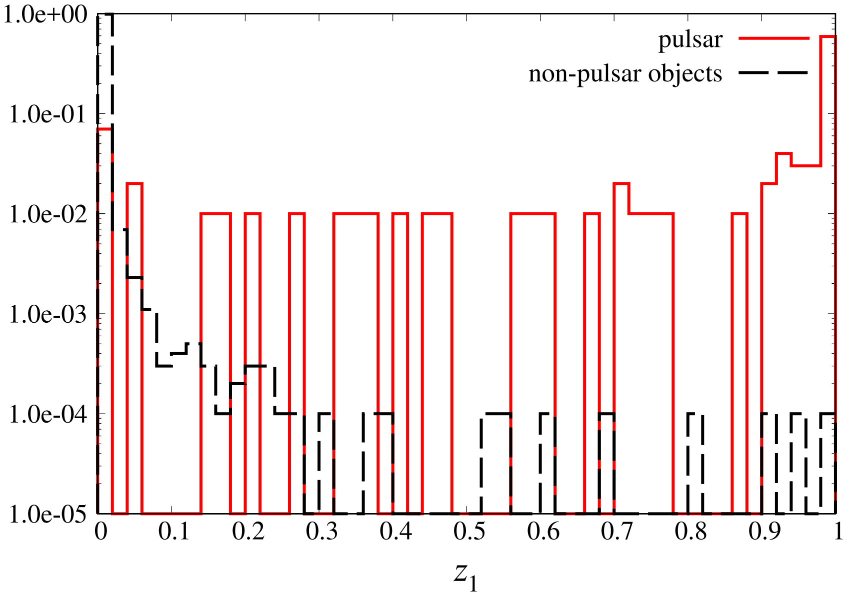

Figure 1.7: Score distribution of z_1 of pulsars and non-pulsars of test data of all of the 10 realizations for Case 1.

following evaluation measures,

$$\text{Recall} = \frac{TP}{TP+FN}, \tag{1.24}$$

$$\text{Precision} = \frac{TP}{TP+FP}, \tag{1.25}$$

$$\text{F1}-\text{score} = \frac{2\times\text{Recall}\times\text{Precision}}{\text{Recall}+\text{Precision}}, \tag{1.26}$$

where TP, FN and FP stand for true positives, false negatives and false positives which represent the numbers of pulsars classified as pulsars, pulsars classified as non-pulsars and non-pulsars classified as pulsars, respectively. Fig. 1.8 shows the averaged Recall, Precision and F1-score over 10 realizations as a function of the criterion of z_1 for Case 1. Although F1-score is the largest at around $z_1 = 0.3$, it is almost flat between 0.1 and 0.9 and drops sharply for $z_1 > 0.9$. In Fig. 1.8, the number of pulsar candidates which are obtained by applying the trained ANN to the unidentified objects in the Gasperin catalog is also shown (see section 5.4). Because non-pulsar objects are considered to dominate the unidentified objects, we choose the threshold to be $z_1 = 0.9$ which gives a high value of Precision and a relatively small number of pulsar candidates. The situation is similar for other Cases, therefore, we take $z_1 = 0.9$ as the criterion of pulsar candidates for all Cases hereafter.

Table 1.2 shows the mean values and standard deviations of three evaluation measures of Recall, or the true positive rate, Precision and F1-score over the trained networks for the fiducial and variant ANNs. Fixing the number of non-pulsar training data to 10,000, Case 3 has the largest evaluation measures, and their variances among the networks are smallest. Thus, Case 3 would be the best ANN of the four. Although, there are uncertainties in the evaluation measures over the networks, it

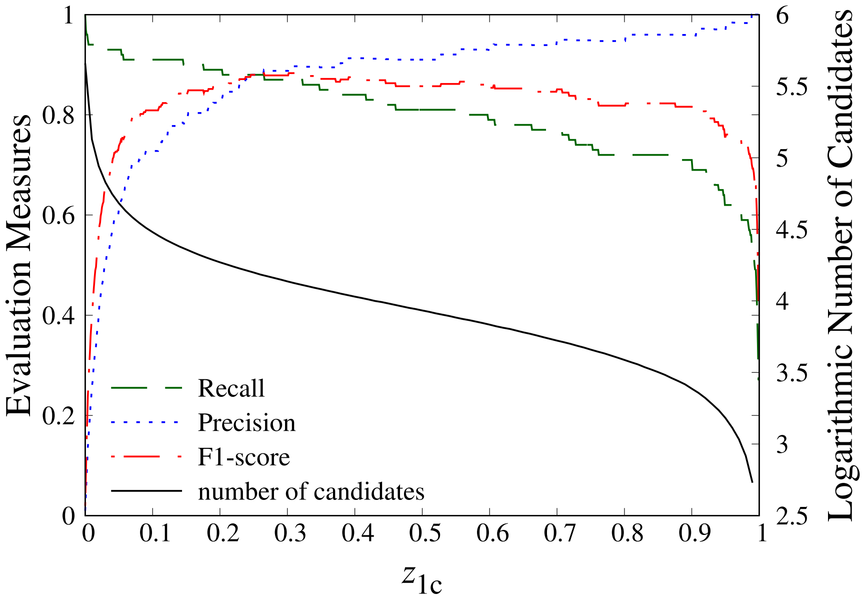

Figure 1.8: Recall, Precision and F1-score averaged over 10 realizations (left axis) and the logarithmic number of pulsar candidates (right axis) which are obtained by applying the trained ANN to the unidentified objects in the Gasperin catalog for Case 1 against the criterion of z_1.

can also be seen from the comparison of the four cases that the absolute value of galactic latitude is a better input than the galactic latitude itself, while individual fluxes of TGSS and NVSS are better than spectral index. Finally, comparing Case 1 with different numbers of non-pulsar training data, it is seen that its increase results in decreasing Recall, but increasing Precision and smaller its variance among the networks. The network in the case of the non-pulsar train data of 200 would be the best in terms of F1-score, but high Precision which means that the ratio of non-pulsars classified as incorrectly pulsars is small is also very important because the number of non-pulsar objects should be much larger than that of pulsars as mentioned above. Table 1.2 represents also the averaged area under the receiver operating characteristic curve (AUC) which the larger area represents a better model for each Case. In view of the AUC, there are little difference among Cases and all of them have quite high performance.

1.5.2 Interpretation of the interior of the trained networks

In this subsection, we try to interpret the behavior of the weights and understand the interior of the trained ANNs by neglecting the activation functions. In this approximation, an output from the hidden layer Eq.(1.14) is given by

$$y_j = a \sum_i x_i \cdot w_{ij}^{(1)} + b_j^{(1)}, \tag{1.27}$$

and therefore, we obtain

$$v_k = a \sum_i x_i \cdot w_{ik} + b_k^{(2)} \tag{1.28}$$

Table 1.2: Recall, Precision and F1-score with a pulsar-candidate criterion of $z_1 \geq 0.9$, averaged area under the receiver operating characteristic curve (AUC) and the number of pulsar candidates with $z_1 \geq 0.9$ obtained by applying the trained ANN to the unidentified objects in the Gasperin catalog described in section 1.5.4 in detail.

Input		Case 1		Case 2	Case 3	Case 4
Number of Non-pulsar Training data	200	1,000	10,000	10,000	10,000	10,000
Recall (%)	85.0±14.9	79.5±16.1	71.0±17.9	52.0±16.9	75.0±14.3	65.0±19.0
Precision (%)	92.6±12.3	96.9±10.9	96.1±6.32	95.4±7.47	98.8±3.95	98.3±5.27
F1-score (%)	87.9±11.7	86.6±13.0	80.3±14.5	65.3±17.9	84.6±9.39	76.4±13.4
Averaged AUC	0.974	0.968	0.976	0.967	0.973	0.989
Number of candidates	20,971	52,615	2,436	3,765	11,675	3,109

by instituting Eq.(1.27) into Eq.(1.17). Here, $a \sim 0.2$ is the coefficient of the linear function, and w_{ik} is the matrix multiplication of the weights between the input and hidden layers $w_{ij}^{(1)}$ and the ones between the hidden and output layers $w_{jk}^{(2)}$

$$w_{ik} = \sum_j w_{ij}^{(1)} \cdot w_{jk}^{(2)}. \tag{1.29}$$

Here, we ignore the bias b_j since we focus on the behavior of the weights in the networks. We can sum up the weights with respect to the hidden layer and the input layer is connected with the output layer directly by approximating the sigmoid function as the linear one. In the following, we study behavior of this w_{ik}.

Fig. 1.9 shows the mean and standard deviation of w_{i1} over the trained networks for each Case of the inputs. The difference of w_{i1} and w_{i2} is just a sign, so that hereafter we refer to only behavior of w_{i1}. The weight of the longitude w_{11} for every Case is consistent with 0, which implies this weight is not significant for the selection, but tends to be slightly positive. On the other hand, the weights of the latitude are basically negative except Case 1, and their variances are larger than the longitude's one. This means that the latitude is important and a small value is preferable for a pulsar since pulsars are often located on the Galactic plane. The negative and positive weights of the TGSS and NVSS fluxes indicate that an object which is bright and dark in the TGSS and NVSS tends to be selected as a pulsar. This behavior is compatible with the fact that an object with a steep spectrum tends to be selected as a pulsar appeared in Fig. 1.9. The weight of the compactness is almost consistent with 0, but is slightly positive for the selection even if the compactnesses of the pulsar and non-pulsar objects look almost the same. This might imply the trained ANNs detect invisible correlation with other parameters.

Finally, it should be noted that, in the above interpretation, possible correlations between the observed quantities are marginalized and only direct correspondence between the quantities and the pulsar score is investigated. Thus, even if the average weight is consistent with zero, it does not necessarily mean the corresponding quantity has no effect on the pulsar selection.

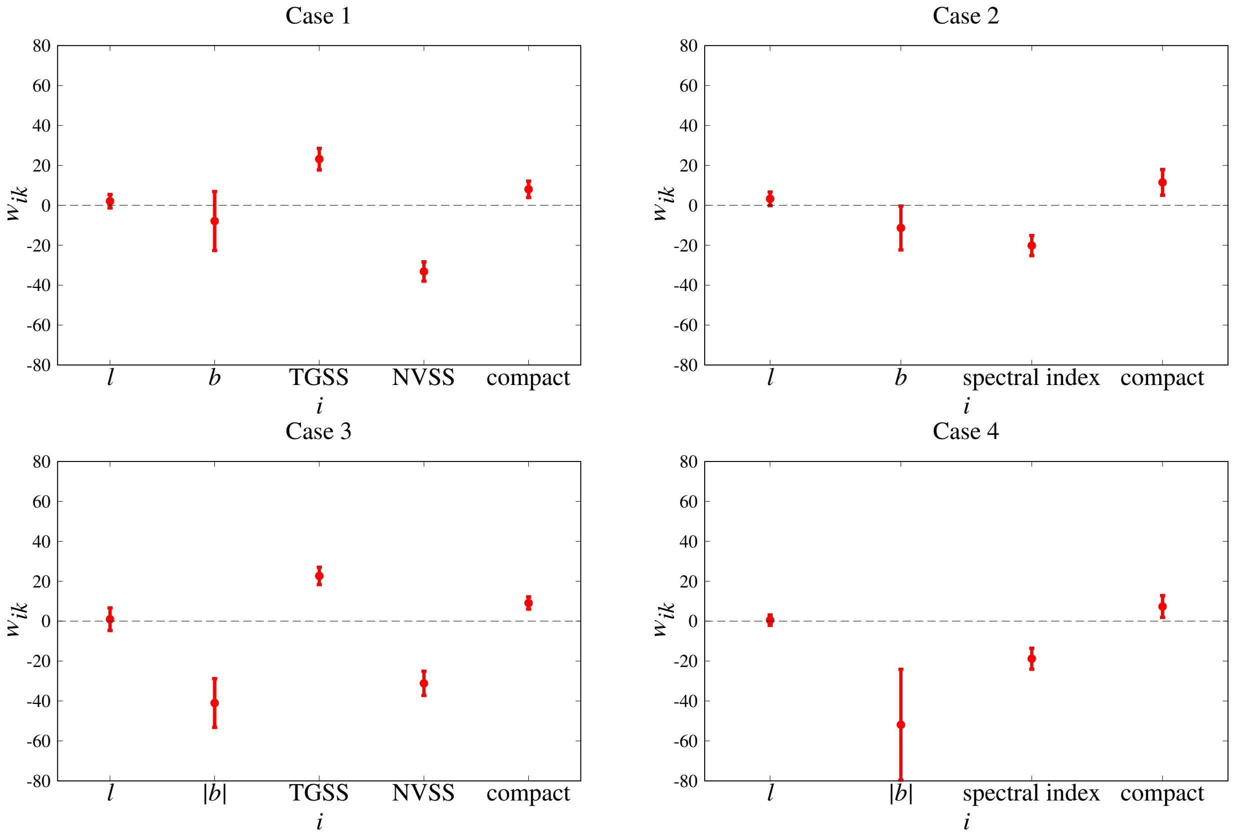

Figure 1.9: Plot of the averaged w_{i1} over realizations with the error bar for each Case.

1.5.3 Missed objects

In this subsection, we show features of the missed objects, which the missed pulsars and non-pulsar objects mean that each of the test data have $z_1 < 0.9$ and $z_1 \geq 0.9$. Fig. 1.10 shows the distribution of the missed pulsars and non-pulsar objects in the galactic coordinate. The thick symbols in Figs. 1.10 and 1.11 represent objects been missed a few times. Although most of pulsars locate in the Galactic plane, the missed ones distribute roughly uniformly, that means pulsars at high latitudes tend to be missed. On the other hand, the number of missed non-pulsars is very small which is very good result, thus their feature does not appear.

Fig. 1.11 shows the scatter plot of the logarithmic TGSS and NVSS fluxes of the missed objects. The missed non-pulsar objects are out of the main part of the non-pulsar objects population, but the missed pulsars look similar to the pulsar distribution in Fig. 1.3.

1.5.4 Selection of pulsar candidates by applying trained networks to unidentified objects

We apply our trained ANNs to the unidentified objects in the Gasperin catalog. In this application, we use the networks of all Cases individually. We choose training and validation data randomly,

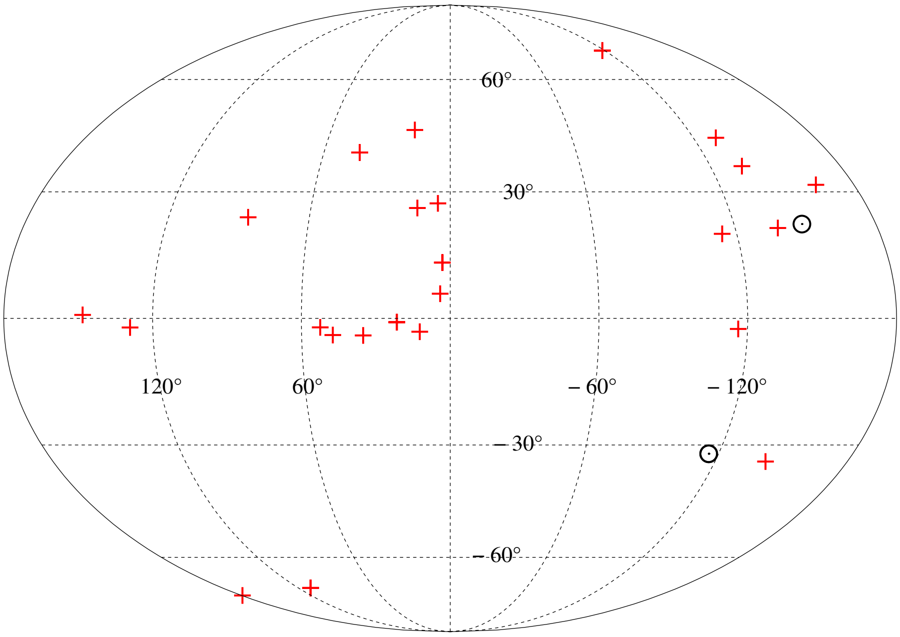

Figure 1.10: Distribution of the "missed" pulsars and non-pulsar objects described by the red crosses and circles in the galactic coordinate.

determine the hyper parameters by the method mentioned in subsection 1.4.2 and train the network with those hyper parameters, and then apply the trained network to the 456,866 unidentified objects. Table 1.2 shows the number of pulsar candidates with $z_1 \geq 0.9$ for each Case. For Case 1, Precision increases as the number of the non-pulsar training data increases and the number of candidates is smallest for the network with the non-pulsar training data of 10,000. Comparing the 4 cases with 10,000 non-pulsar training data, Case 3 has the largest number of candidates which is at least three times more than those for other Cases, while Precisions are comparable within the statistical errors. Because the unidentified objects can be considered to be dominated by non-pulsars, we regard the Case 1 with 10,000 non-pulsar training data as the most effective ANN.

Next, we describe the candidates of Case 1 more in detail. Fig. 1.12 shows the distributions of the known pulsars and non-pulsars which are same in Fig. 1.2 and 2,436 pulsar candidates in the sky. The candidates are mainly located on the Galactic plane, but some of them are also at high latitudes. This distribution seems to be biased by the SDSS-surveyed and non-observed areas especially in the upper right area at $-180° \lesssim l \lesssim -120°$ and $0° \lesssim b \lesssim 30°$ of Fig. 1.12, where the candidates are less than them in the upper left area at $120° \lesssim l \lesssim 180°$ of Fig. 1.12.

Fig. 1.13 shows the logarithmic TGSS and NVSS fluxes of the known pulsars and non-pulsars, and 2,436 candidates. The candidate distribution is not almost overlapped with the non-pulsar's one and some candidates lie on the bottom line of the NVSS detection limit.

To show the validity of our method, we checked if our candidates include newly-found pulsars and candidates in [43, 80], and found that our candidate cross-match twenty one of twenty five

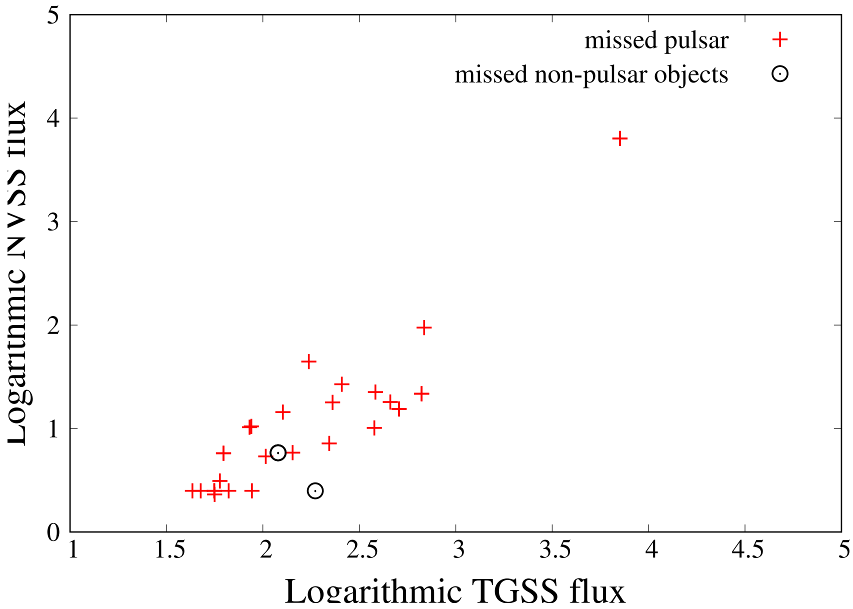

Figure 1.11: Scatter plot of the logarithmic TGSS and NVSS fluxes of the "missed" pulsars and non-pulsar objects described by the red crosses and black circles.

candidates in [80], while three of five new pulsars and three of five candidates in [43] are included in our candidates. One of missed pulsars in [43] has a very steep spectrum and locates in the Galactic center. Verification of our method through timing observation is ongoing and will be presented elsewhere[1]

1.6 Discussion and future works

We applied artificial neural networks (ANNs) for efficient selection of pulsar candidates from continuum surveys, adopting the method in [38] to determine hyper-parameters. From the input quantities such as radio fluxes, sky position and compactness, ANNs were constructed to output a score that represents a degree of likelihood for an object to be a pulsar. We demonstrated ANNs based on existing survey data by the TGSS and the NVSS and tested their performance varying the input parameters and the number of training data. Finally, we obtained pulsar candidates by applying the trained ANNs to unidentified radio sources. In the future, these candidates should be observed with timing measurement to verify whether they are really pulsars or not.

In order to evaluate our trained networks, we utilized the area under the receiver operating characteristic curve (AUC) and the ratio of the test data with $z_1 \geq 0.9$ to all of them. As a result of training, the AUCs and test using the test data indicate that the trained networks have high classification performance and Precision, which is the ratio of pulsars classified correctly as pulsars to objects classified as pulsars, is basically high of more than 95%. This implies that the ratio of non-pulsar objects classified as pulsars to objects classified as pulsars, or pulsar candidates, is less

---

[1] For more information and catalog of our candidates, contact the authors.

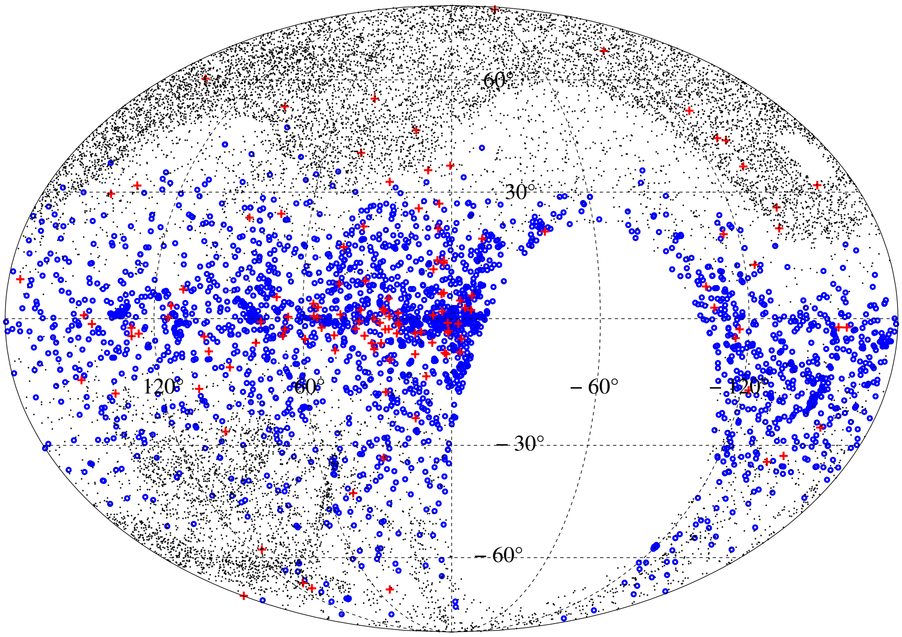

Figure 1.12: Distribution of the known pulsars and non-pulsar objects, and 2,436 candidates with $z_1 \geq 0.9$ described by the red crosses, black crosses and blue circles in the galactic coordinate.

than 5%, albeit non-pulsar objects are considered to dominate radio point sources, thus our ANNs work pretty well for the pulsar candidate selection. The resultant number of pulsar candidates for Case 1 is 2,436 with $z_1 \geq 0.9$ shown in Figs. 1.12 and 1.13.

Let us discuss difference of the biases between training and unidentified object data sets. Although the unidentified objects distribute almost uniformly in the Gasperin catalog covered area, the distribution of non-pulsars in the training data has different bias from the unidentified object one due to the limited SDSS survey area as can be seen in Figs 1.2 and 1.12. In order to investigate the effect of the spatial bias of the training data, we perform the same analysis with 3,639 non-pulsars sampled spatially uniformly in the Gasperin catalog area. We use 3,500 for training and 100 for validation out of 3,638 non-pulsars. Consequently, we obtain 3,636 candidates with $z_1 \geq 0.9$ by applying the ANN to the unidentified objects. The spatial distributions of the training data and candidates are shown in Fig. 1.14. Compared to Fig. 1.12, the candidates are not so concentrated to the Galactic plane. This implies that the spatial distribution of candidates is affected by the spatial bias of the training data. Further study on the effect of the bias is beyond the scope of the current work and will be presented elsewhere.

As mentioned in section 1.3.1, ANNs with sufficient neurons in the hidden layer are known to work well. Here, we vary the number of neurons in the hidden layer to investigate its effect on classification performance. We study cases that the numbers of neurons in the hidden layer are once and thrice those in the input layer. Table 1.3 is same as Table 1.2 showing Recall, Precision, F1-score, the averaged AUC and the number of candidates with $z_1 \geq 0.9$. Although the performance reduces

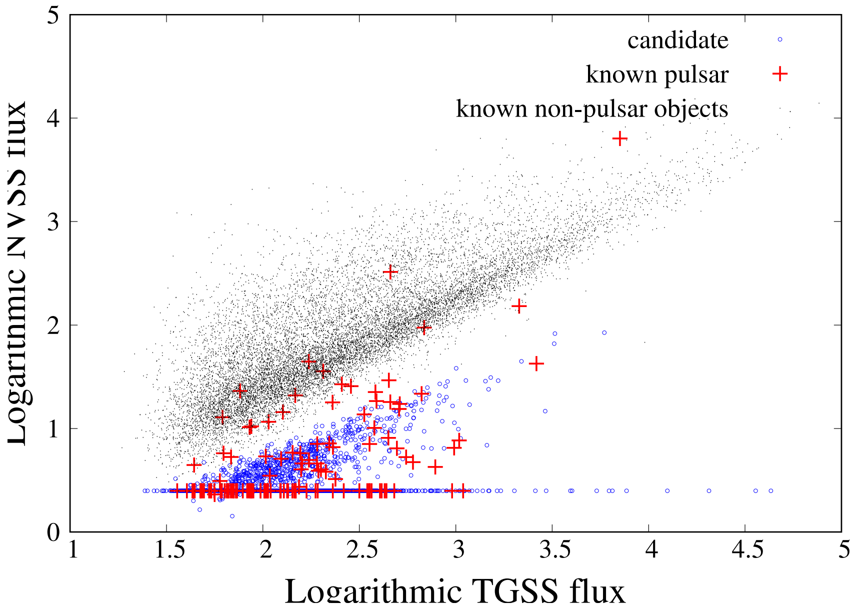

Figure 1.13: Scatter plot of the logarithmic TGSS and NVSS fluxes of the known pulsars and non-pulsar objects, and 2,436 candidates with $z_1 \geq 0.9$ described as the red crosses, black dots and blue circles.

a little in the case of ANNs with five neurons in the hidden layer, the number of neurons is not so effective. From the aspect of the AUC, there is little difference in the performance. Hence, we conclude that it is reasonable to set the number of neurons in the hidden layer to ten which is twice those in the input layer.

Besides ANN, there are some other machine learning methods such as the support vector machine and random forest, which exhibit excellent performances of the pattern recognition. It is worth applying other machine learning methods to the pulsar candidate selection, but it is beyond the scope of this paper and will be pursued elsewhere in future.

In this work, we used objects in the Gasperin catalog cross-matched with the ATNF pulsar catalogue and the MILLIQUAS catalog as training data of the pulsars and non-pulsar objects. Although these are currently the largest available catalogs, the number of cross-matched pulsars is relatively

Table 1.3: Same as Table 1.2 for Case 1 which the ANNs consist of five, ten (fiducial) and fifteen neurons in the hidden layers.

Number of Neurons	5	10	15
Recall (%)	56.0±19.6	71.0±17.9	67.0±19.5
Precision (%)	93.7±8.40	96.1±6.32	97.4±5.72
F1-score (%)	67.6±16.6	80.3±14.5	77.8±14.6
Averaged AUC	0.985	0.976	0.988
Number of candidates	4,325	2,436	9,164

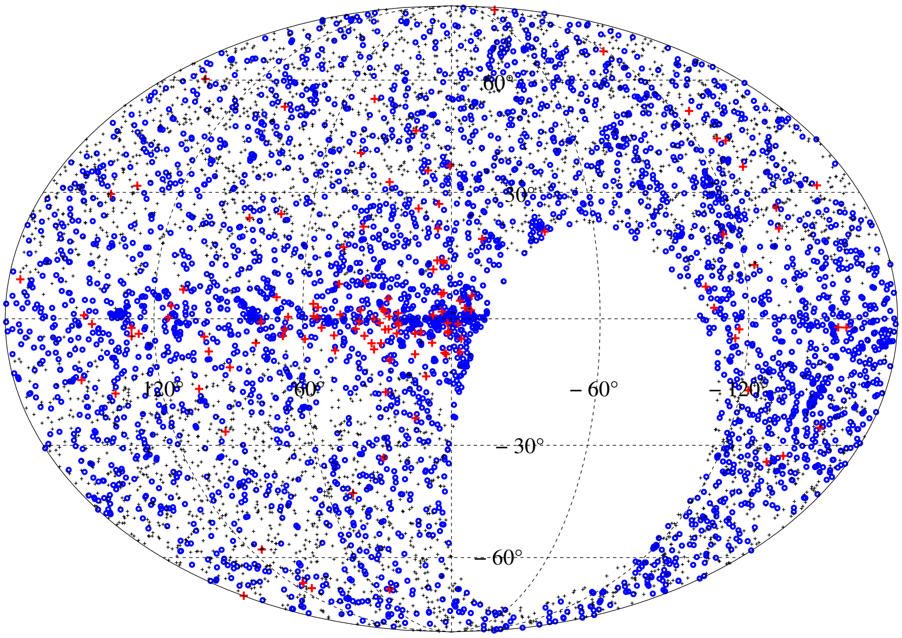

Figure 1.14: Distribution of the known pulsars and 3,639 non-pulsar objects sampled uniformly in the sky, and 3,636 candidates with $z_1 \geq 0.9$ described by the red crosses, black crosses and blue circles in the galactic coordinate.

small and we need a further analysis with future larger catalogs to consider if ANN is effective for the selection of pulsar candidates.

Other observable quantities such as the rotation measure and polarization fraction could be useful as inputs. We did not adopted them because the number of radio sources with them are currently very limited. If we can have a sufficient number of samples with them as it is expected in future large surveys, they will make ANNs more effective and narrow the pulsar candidates down further.

Chapter 2

Searching for gravitational wave bursts from cosmic string cusps with pulsar timing array

2.1 Gravitational waves

In Einstein's general relativity (GR), gravity results from the curvature of space and time, or spacetime, described using Riemannian geometry. GR predicts some exciting phenomena such as the existence of the BH, the expansion of the Universe, etc.. One of the predictions is a GW that propagates at speed of light. For one hundred years since the prediction of its existence, it had not been detected directly due to its extreme weakness of interaction. In 2015, however, the first detection of GWs from the coalescence of a BH-BH binary has been achieved by the Laser Interferometer Gravitational-wave Observatory (LIGO) in the United States. This detection enabled us to test GR in the strong gravitational field and confirm the existence of BHs and formation of their binaries. Furthermore, GWs from a NS-NS binary were detected by three detectors including the Virgo interferometer in 2017 and use of three detectors could allow a precise localization of the event. The subsequent identification of its transient electromagnetic counterpart led to the opening of the era of multi-messenger astrophysics.

While low-frequency GWs at nHz frequencies corresponding to periods of ∼10 years could be detected by PTAs. In the PTA band, the targets are mainly expected to be the incoherent superposition of GWs, called the GW background (GWB), from inspiraling supermassive BH (SMBH) binaries. In the latter part of this section, we describe the detection principle of PTA and current status of observation.

Einstein field equation

First, we introduce derivation of the Einstein field equation briefly. Suppose that the gravitational field action is given by the Einstein-Hilbert action,

$$S_g = \frac{c^3}{16\pi G}\int d^4x\sqrt{-g}\ R, \tag{2.1}$$

where $g = \det(g_{\mu\nu})$ is the determinant of the metric tensor matrix and R is the Ricci scalar. The variation of the action is calculated as

$$\delta S_g = \frac{c^3}{16\pi G}\int \left(\delta g^{\mu\nu} R_{\mu\nu}\sqrt{-g} + g^{\mu\nu}\delta R_{\mu\nu}\sqrt{-g} + g^{\mu\nu}R_{\mu\nu}\delta\sqrt{-g}\right)\, d^4x. \tag{2.2}$$

Using the metric compatibility of the covariant derivative, the second term of the integrand is calculated as

$$\begin{aligned} g^{\mu\nu}\delta R_{\mu\nu} &= (g^{\mu\nu}\delta\Gamma^{\lambda}_{\mu\nu})_{;\lambda} - (g^{\mu\nu}\delta\Gamma^{\lambda}_{\mu\lambda})_{;\nu} \\ &= (g^{\mu\nu}\delta\Gamma^{\lambda}_{\mu\nu} - g^{\mu\lambda}\delta\Gamma^{\nu}_{\mu\nu})_{;\lambda}, \end{aligned} \tag{2.3}$$

which vanishes when integrated because $\delta\Gamma^{\lambda}_{\mu\nu}$ is zero at the boundary of infinity. Consequently, Eq. (2.2) becomes

$$\delta S_g = \frac{c^3}{16\pi G}\int \left(R_{\mu\nu} - \frac{1}{2}Rg_{\mu\nu}\right)\delta g^{\mu\nu}\sqrt{-g}\; d^4x, \tag{2.4}$$

by using the relational expression,

$$\delta\sqrt{-g} = \frac{1}{2}\sqrt{-g}\; g_{\mu\nu}\delta g^{\mu\nu}. \tag{2.5}$$

The stress-energy tensor is defined by the variation of the matter action, which is given by

$$\delta S_m = \frac{1}{2c}\int d^4x\sqrt{-g}\; T^{\mu\nu}\delta g_{\mu\nu}. \tag{2.6}$$

Then, the principle of least action, $\delta S = \delta S_g + \delta S_m = 0$, leads the equation of motion that is the Einstein field equation

$$R_{\mu\nu} - \frac{1}{2}Rg_{\mu\nu} = \frac{8\pi G}{c^4}T_{\mu\nu}. \tag{2.7}$$

Gravitational waves

Einstein's equation is attributed to the wave equation in analogy with electromagnetic waves. For the present, we consider the tiny deviation from the background metric, or "linearized gravity", given by

$$g_{\mu\nu} = \eta_{\mu\nu} + h_{\mu\nu}, \qquad |h_{\mu\nu}| \ll 1, \tag{2.8}$$

where, η is the flat background metric. Here, we define

$$\phi_{\mu\nu} \equiv h_{\mu\nu} - \frac{1}{2}hg_{\mu\nu} = h_{\mu\nu} - \frac{1}{2}h\eta_{\mu\nu}, \tag{2.9}$$

$$h \equiv h^{\mu}{}_{\mu} = g^{\mu\nu}h_{\mu\nu} = \eta^{\mu\nu}h_{\mu\nu}. \tag{2.10}$$

With Eqs. (2.9) and (2.10), we obtain

$$h_{\mu\nu} = \phi_{\mu\nu} - \frac{1}{2}\phi\eta_{\mu\nu}, \tag{2.11}$$

$$\phi = \phi^{\mu}{}_{\mu} = -h. \tag{2.12}$$

For this metric (spacetime), the Christoffel symbol is given by

$$\Gamma_{\alpha\beta\gamma} = \frac{1}{2}\left(\frac{\partial h_{\alpha\beta}}{\partial x^{\gamma}} + \frac{\partial h_{\alpha\gamma}}{\partial x^{\beta}} - \eta_{\alpha}{}^{\mu}\frac{\partial h_{\beta\gamma}}{\partial x^{\mu}}\right), \tag{2.13}$$

and the Riemann curvature tensor, Ricci tensor and Ricci scalar are given by

$$\begin{aligned} R_{\mu\alpha\beta\nu} &= \frac{1}{2}\left(\frac{\partial^2 h_{\mu\nu}}{\partial x^{\alpha}\partial x^{\beta}} + \frac{\partial^2 h_{\alpha\beta}}{\partial x^{\mu}\partial x^{\nu}} - \frac{\partial^2 h_{\alpha\nu}}{\partial x^{\mu}\partial x^{\beta}} - \frac{\partial^2 h_{\mu\beta}}{\partial x^{\alpha}\partial x^{\nu}}\right) && (2.14)\\ R_{\alpha\nu} &= \frac{1}{2}\left\{\frac{\partial}{\partial x^{\alpha}}\left(\frac{\partial h_{\nu}{}^{\beta}}{\partial x^{\beta}} - \frac{1}{2}\frac{\partial h}{\partial x^{\nu}}\right) + \frac{\partial}{\partial x^{\nu}}\left(\frac{\partial h_{\alpha}{}^{\beta}}{\partial x^{\beta}} - \frac{1}{2}\frac{\partial h}{\partial x^{\alpha}}\right) - \Box h_{\alpha\nu}\right\} && (2.15)\\ R &= \frac{\partial^2 \phi^{\alpha\beta}}{\partial x^{\alpha}\partial x^{\beta}} - \frac{1}{2}\Box h, && (2.16) \end{aligned}$$

where $\Box$ represents the d'Alembert operator,

$$\Box = \eta^{\mu\nu}\frac{\partial}{\partial x^{\mu}}\frac{\partial}{\partial x^{\nu}}. \tag{2.17}$$

Substituting Eqs. (2.14) – (2.16) into Eq.(2.7), we obtain

$$\Box\phi_{\mu\nu} - \frac{\partial}{\partial x^{\mu}}\left(\frac{\partial \phi_{\nu}{}^{\alpha}}{\partial x^{\alpha}}\right) - \frac{\partial}{\partial x^{\nu}}\left(\frac{\partial \phi_{\mu}{}^{\alpha}}{\partial x^{\alpha}}\right) + \frac{\partial}{\partial x^{\alpha}}\left(\frac{\partial \phi_{\gamma}{}^{\beta}}{\partial x^{\beta}}\right)\eta^{\alpha\gamma}\eta_{\mu\nu} = -\frac{16\pi G}{c^4}T_{\mu\nu}. \tag{2.18}$$

Einstein's equation holds general covariance which denotes the invariance of forms of physical laws under any differentiable coordinate transformations so that we consider a coordinate transformation below in order to simplify Eq.(2.18),

$$x'^{\mu} = x^{\mu} + \xi^{\mu}. \tag{2.19}$$

Then, $h_{\mu\nu}$ and $\phi_{\mu\nu}$ are transformed as

$$\begin{aligned} h'_{\mu\nu} &= h_{\mu\nu} - \eta_{\mu\alpha}\frac{\partial \xi^{\alpha}}{\partial x^{\nu}} - \eta_{\nu\alpha}\frac{\partial \xi^{\alpha}}{\partial x^{\mu}} && (2.20)\\ \phi'_{\mu\nu} &= \phi_{\mu\nu} - \eta_{\mu\alpha}\frac{\partial \xi^{\alpha}}{\partial x^{\nu}} - \eta_{\nu\alpha}\frac{\partial \xi^{\alpha}}{\partial x^{\mu}} + \eta_{\mu\nu}\frac{\partial \xi^{\alpha}}{\partial x^{\alpha}} && (2.21) \end{aligned}$$

and the derivative of $\phi_{\mu}{}^{\nu}$ is transformed as

$$\frac{\partial \phi'_{\mu}{}^{\nu}}{\partial x'^{\nu}} = \frac{\partial \phi_{\mu}{}^{\nu}}{\partial x^{\nu}} - \eta_{\mu\alpha}\Box\xi^{\alpha}. \tag{2.22}$$

In the following, we adopt ξ which satisfies a condition below

$$\frac{\partial \phi'_{\mu}{}^{\nu}}{\partial x'^{\nu}} = 0. \tag{2.23}$$

In this coordinate, Eq.(2.18) is finally described as the linear wave equation which is given by

$$\Box\phi_{\mu\nu} = -\frac{16\pi G}{c^4}T_{\mu\nu}. \tag{2.24}$$

This equation implies the existence of GWs. The condition of Eq.(2.23) for ${\phi_\mu}^\nu$ is called the gauge condition as well as the electromagnetic four-potential.

Next, let us examine the solution of Eq.(2.24) in a vacuum, or outside the source,

$$\Box\phi_{\mu\nu} = 0, \tag{2.25}$$

and its behavior. The monochromatic plane wave solution of Eq.(2.25) is given by

$$\phi_{\mu\nu} = a_{\mu\nu} \exp(ik_\alpha x^\alpha), \tag{2.26}$$

where $a_{\mu\nu}$ is the amplitude tensor which is symmetric with ten independent components and k_α is the four-wave vector which satisfies $k_\alpha k^\alpha = 0$ which implies the null geodesics. The gauge condition (2.23) requires $a_{\mu\nu}k^\nu = 0$ that describes transverse. For simplicity, we consider GWs propagating at the x^3 direction, or along the z axis, which the wave vectors are given by

$$k_\mu = (-k, 0, 0, k)\,,\ \ k^\mu = (k, 0, 0, k)\,. \tag{2.27}$$

The amplitude tensor $a_{\mu\nu}$ is transformed as

$$a'_{\mu\nu} = a_{\mu\nu} - \epsilon_\mu k_\nu - \epsilon_\nu k_\mu + \eta_{\mu\nu}\epsilon^\alpha k_\alpha \tag{2.28}$$

by an infinitesimal coordinate transformation (gauge transformation) $x^\mu \to x^\mu + \xi^\mu(x)$ where $\xi^\mu(x) = \epsilon^\mu \exp(ik_\alpha x^\alpha)$. We obtain

$$a'_{00} = a'_{01} = a'_{02} = 0 \tag{2.29}$$

$$a'_{11} = -a'_{22} \tag{2.30}$$

by choosing ϵ_μ that satisfies

$$\epsilon_0 = -\frac{2a_{00} + a_{11} + a_{22}}{4k} \tag{2.31}$$

$$\epsilon_1 = \frac{a_{01}}{-k} \tag{2.32}$$

$$\epsilon_2 = \frac{a_{02}}{-k} \tag{2.33}$$

$$\epsilon_3 = \frac{2a_{00} - a_{11} - a_{22}}{4k}. \tag{2.34}$$

Eq.(2.29) and (2.30) reveal that the degree of freedom of $\phi_{\mu\nu}$ reduces to two and, consequently, it is given by

$$\phi_{\mu\nu} = A^+ e^+_{\mu\nu} \exp(ik_\alpha x^\alpha) + A^\times e^\times_{\mu\nu} \exp(ik_\alpha x^\alpha). \tag{2.35}$$

Here, $e^{+,\times}_{\mu\nu}$ is the GW polarization tensor, which is expressed as

$$e^+_{\mu\nu} = \begin{pmatrix} 0 & 0 & 0 & 0 \\ 0 & 1 & 0 & 0 \\ 0 & 0 & -1 & 0 \\ 0 & 0 & 0 & 0 \end{pmatrix},\ e^\times_{\mu\nu} = \begin{pmatrix} 0 & 0 & 0 & 0 \\ 0 & 0 & 1 & 0 \\ 0 & 1 & 0 & 0 \\ 0 & 0 & 0 & 0 \end{pmatrix}, \tag{2.36}$$

and $A^{+,\times}$ is the amplitude for each polarization (oscillation mode). Since the trace of $\phi_{\mu\nu}$ is zero, we obtain

$$\begin{aligned} h_{\mu\nu} &= \phi_{\mu\nu} \\ &= A^{+} e^{+}_{\mu\nu} \exp(ik_\alpha x^\alpha) + A^{\times} e^{\times}_{\mu\nu} \exp(ik_\alpha x^\alpha). \end{aligned} \tag{2.37}$$

Note that the transverse-traceless (TT) gauge which is considered above can not be chosen inside the source because in this case $\Box\phi_{\mu\nu} \neq 0$.

Generation of GWs

In the case that an observer is in a great distance compared to the scale of the source motion, the retarded solution of Eq.(2.24) can be expressed as

$$h^{\mu\nu}(x) = \frac{4G}{c^4 R} \int T^{\mu\nu}(x^0 - R, x'^1, x'^2, x'^3) dx'^1 dx'^2 dx'^3 \tag{2.38}$$

in the TT gauge which leads to $\phi^{\mu\nu} = h^{\mu\nu}$, where R is the distance from the source. The spacial part of Eq.(2.38) is given by

$$h^{ij}(x) = \frac{2G}{c^4 R} \ddot{I}^{ij}(t - R/c). \tag{2.39}$$

Here I^{ij} is the quadrupole moment of the mass distribution which is defined as

$$I^{ij}(t - R/c) = \int \rho(t - R/c) x'^i x'^j dx'^1 dx'^2 dx'^3, \tag{2.40}$$

where ρ is the mass density. Here, note that there could not be monopolar and dipolar gravitational radiations due to conservations of mass and momentum (Newton's third law), respectively. The coefficient of $2G/c^4 \sim \mathcal{O}(10^{-44})$ of the right-hand side of Eq.(2.39) implies that amplitude of GWs is extremely tiny. Therefore, compact and dense objects with large acceleration such as BH, or NS binaries and supernova explosions mentioned in the following section could be detectable GW sources.

Observation of GWs

GWs are observed with different methods depending on their frequencies as well as electromagnetic waves. Fig. 2.1 shows the sensitivity curves for characteristic strain against frequency for a variety of techniques; the ground-based interferometer at 10 Hz to 10 kHz, the space-based interferometer at 0.1 mHz to 1 Hz and pulsar timing array (PTA) at 1 nH to 1 μHz mentioned in section 2.1.1 in detail. Here, characteristic strain is defined as

$$[h_c(f)]^2 = 4f^2 \left|\tilde{h}(f)\right|^2, \tag{2.41}$$

where f is the GW frequency and $\tilde{h}(f)$ is the inverse Fourier transformed GW amplitude $h(t)$.

A representative technique is the Michelson interferometer which is originally designed to measure the ether. The concept of this technique is in principle simple and elegant. An interferometer consists of two orthogonal arms with same lengths, and two laser beams travel in the arms which are separated by a beam-spliter on an intersection of the arms. After traveling once back and forth, the two beams recombine again at the beam-spliter and the resulting beam goes to a photodetector. Quadrupole GWs stretch one arm and squeeze another one, and the arm length modulation caused by GWs which is given by $\Delta L(t) = \delta L_x - \delta L_y = h(t)L$ where L is the arm length is observed as light intensity modulation.

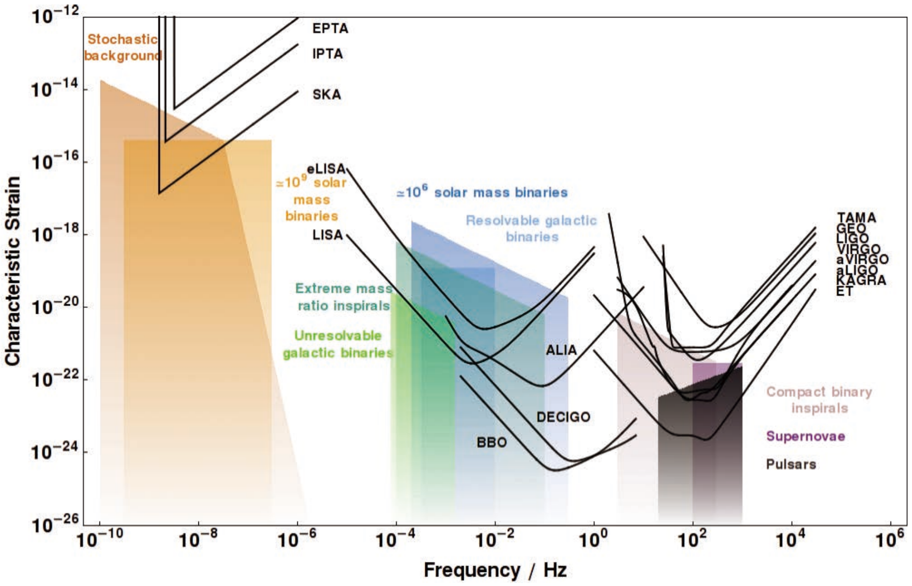

Figure 2.1: Sensitivity for characteristic strain as a function of frequency for each observing technique [85]. Color bars represent the theoretically expected strength of GWs from a variety of sources.

Currently, the Laser Interferometer Gravitational-Wave Observatory (LIGO) in the United States and the Virgo interferometer in Europe have been running and the Kamioka Gravitational Wave Detector (KAGRA), formerly the Large Scale Cryogenic Gravitational Wave Telescope, in Japan will start running in 2020. On September 14th 2015 at the beginning of the first observing run, denoted by O1, the two detectors of the LIGO Observatory have succeeded in the very first detection of GWs emitted by the coalescence of a BH-BH binary, labelled GW150914 [3]. The signal was detected in coincidence between the detectors in Hanford, Washington (H1) and in Livingstone, Louisiana (L1) which the wave-front arrived first at L1 and $6.9^{+0.5}_{-0.4}$ ms later at H1. It was sufficiently strong that the peak GW strain is 1.0×10^{-21} which the corresponding matched-filter signal-to-noise ratio (SNR) is 24 and the significance level is higher than 5.1σ and the waveform can be seen visually just by using a 35-350 Hz bandpass filter where the signal is concentrated, even before performing any detailed data analysis. The top and second rows in Fig. 2.2 show the observed waveform of GW150914, and the numerical relativity waveform with the best-fit parameters (solid line) and its 90% credible regions (gray shaded curves), respectively. The last row represents the signal in the time-frequency plane which shows the frequency increases in time, up to a maximum value, until the signal disappears. At first, the event was detected by a low-latency search for generic GW transients, and then identified as a BH-BH binary and studied subsequently in more detail by performing matched filtering to merging binary waveforms. The matched filter search unveiled as follows. The binary system was composed of two BHs with initial masses of $36M_\odot$ and $29M_\odot$, and they coalesced into a final BH with a mass of $62M_\odot$. The coalescence produced an energy of $3M_\odot c^2$ in the form of GWs in few milliseconds. The event happened at a cosmological distance, with a luminosity distance of around 440 Mpc and a cosmological redshift $z \simeq 0.09$.

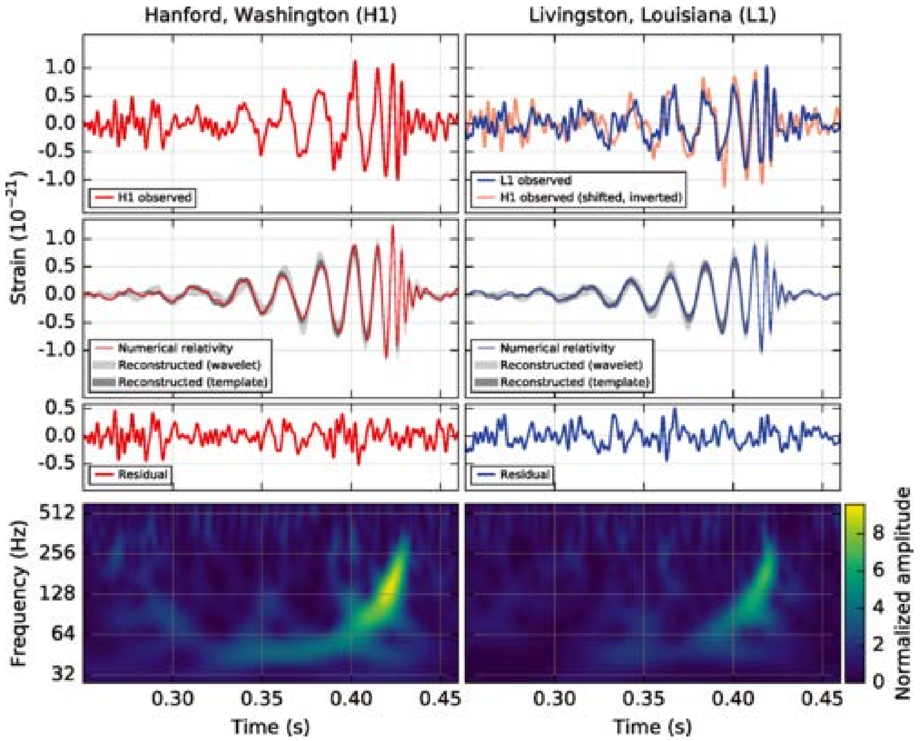

Figure 2.2: The event GW150914 observed by the LIGO Hanford H1 (left column panels) and Livingston (L1, right column panels) detectors. For visualization, all time series are filtered with a 35350 Hz bandpass filter to suppress large fluctuations outside the detectors' most sensitive frequency band. *Top row, left*: H1 strain. *Top row, right*: L1 strain. The signal arrived first at L1 and $6.9^{+0.5}_{-0.4}$ ms later at H1; for a visual comparison, the H1 data are also shown, shifted in time by this amount and inverted (to account for the detectors' relative orientations). *Second row*: GW strain projected onto each detector in the 35350 Hz band. Solid lines show a numerical relativity waveform for a system with parameters consistent with those recovered from GW150914. Shaded areas show 90% credible regions for two independent waveform reconstructions. *Third row*: Residuals after subtracting the filtered numerical relativity waveform from the filtered detector time series. *Bottom row*: A time-frequency representation, or dynamic spectrum, of the strain data, showing the signal frequency increasing over time. From the discovery paper [3].

On August 17th 2017 at the end of the O2 run, another historic milestone in GW research took place; the LIGO and Virgo interferometers detected the signal from the inspiral and merger of a NS-NH binary, labelled GW170817 [6]. The signal was detected with a combined SNR across the three detectors of 32.4 which was the loudest yet observed. The long-duration inspiral signal shown in Fig. 2.3 allows a very precise determination of the chirp mass which characterises GW strain, defined as

$$\mathcal{M} \equiv \frac{(m_1 m_2)^{3/5}}{(m_1 + m_2)^{1/5}}, \tag{2.42}$$

where m_1 and m_2 are the masses of objects composing the binary. The reconstructed chirp mass is $\mathcal{M} = 1.188^{+0.004}_{-0.002} M_\odot$ and the inferred initial component masses are $m_1 = 1.36 - 1.60 M_\odot$ and $m_2 = 1.17 - 1.36 M_\odot$ assuming a low-spin prior $|\chi_z| \equiv \mathbf{\hat{a}} \cdot \mathbf{L} \leq 0.05$ where $\mathbf{\hat{a}}$ is the dimensionless spin parameter and $\mathbf{L}$ is the orbital angular momentum. These initial masses are in the typical range expected for NS and significantly smaller than the masses of known stellar-mass BHs, this leads to a NS-NS binary interpretation. The source had the closest luminosity distance of 40^{+8}_{-14} Mpc, and was localized very precisely within a sky region of 28 deg^2 (90% probability) due the configuration of the interferometers, especially the Virgo detector. In contrast to the high SNRs in the LIGO-L1 and -H1 detectors of 26.4 and 18.8, that in the Virgo detector were only 2.0 since the signal arrived from close to a blind direction of Virgo. GW interferometers have a quite broad angular sensitivity described by the pattern functions which are in principle same as Eq. (2.45). Thus, the low SNR in the Virgo detector made a very precise localization, whereas did not contribute significantly to estimation of the other parameters of the source.

A gamma-ray burst (GRB), GRB 170817A, was observed independently by Fermi Gamma-Ray Burst Monitor (Fermi-GBM) and INTEGRAL soon after the NS-NS merger. The difference between the coalescence and GRB times is $\Delta t = 1.734 \pm 0.054$s. This is consistent with the theoretical expectations which predict that the mechanisms responsible for launching a jet and producing the prompt γ-radiation acts on a time-scale of at most a few seconds after coalescence. The GRBs observed by two detectors of Fermi-GBM and INTEGRAL are proved to be same by the statistical significance of the temporal coincidence between both observations of 4.2σ, the consistency between the observed event fluences (energy per unit area) and the temporal structure. Further, the probability that the coincidence between the GW signal and GRB is due to chance is only 5.0×10^{-8} that means the association of the GW event with the GRB form the rate of the GRB and the agreement in the spatial localization of the events. The electromagnetic counterpart was first detected and announced by the One-Meter, Two-Hemisphere (1M2H) team using the 1 m Swope Telescope at the Las Campanas Observatory in the near-infrared i-band. The identified source was in the galaxy NGC 4993, an elliptical galaxy in the constellation Hydra, at a redshift $z = 0.009680 \pm 0.00079$. This corresponding luminosity distance is $d_L = 40.4 \pm 3.4$ Mpc which is consistent with the estimation from the GW signal. The identification and precise localization of the electromagnetic counterpart allowed detailed follow-up observation in the whole electromagnetic spectrum by a large number of ground- and space-based telescopes. This remarkable event has opened the era of multi-messenger astrophysics.

Before the first direct detection by the LIGO detectors, GWs have been detected indirectly with the observation of decay of the orbital period of the Hulse-Taylor binary pulsar, PSR B1913+16 which was first detected in 1974. The orbital period of this binary is less than 8 hours which means that the orbital velocity is of order $\sim 10^{-3}c$. For such a quite relativistic binary, energy and angular momentum of the binary are extracted by GW emission, and consequently the orbit shrinks and the orbital period decays. The orbital decay rate due to GW emission is given by

$$\dot{P}_{b,\mathrm{GW}} = -\frac{192\pi (G\mathcal{M})^{5/3}}{5c^5} \left(\frac{P_b}{2\pi}\right)^{-5/3} (1 - e^2)^{-7/2} \left(1 + \frac{73}{24}e^2 + \frac{37}{96}e^4\right), \tag{2.43}$$

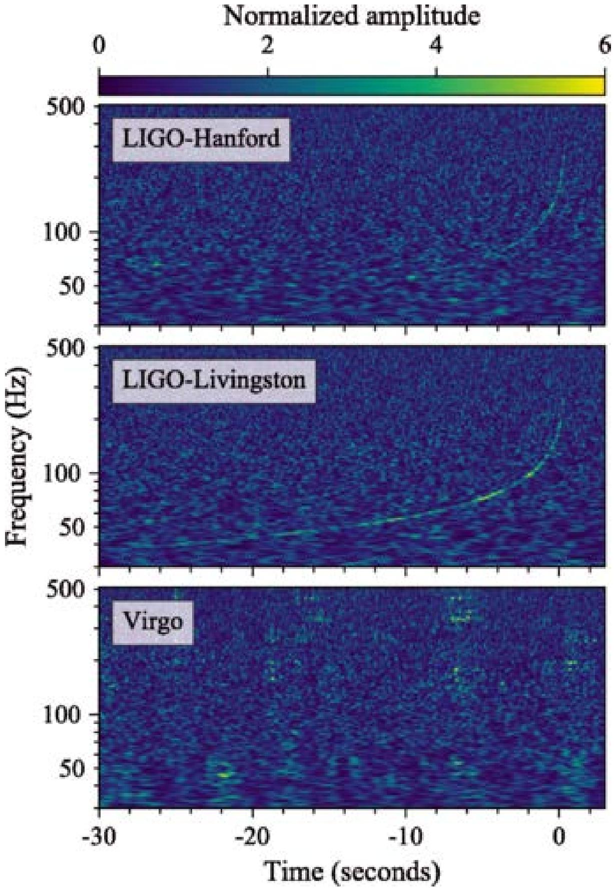

Figure 2.3: Normalized amplitude of data containing the gravitational-wave event GW170817, observed by the LIGO-Hanford (top), LIGO-Livingston (middle), and Virgo (bottom) detectors in the time-frequency domain. Times are shown relative to August 17, 2017 1241:04UTC [6].

where e is the eccentricity. With using the pulsar mass of $m_1 = 1.4414(2)M_{\odot}$, its companion mass $m_1 = 1.3867(2)M_{\odot}$ and other observed orbital elements, we predict $\dot{P}_{b,\mathrm{GW}} = -2.40242(2) \times 10^{-12}$, while the observed decay is $\dot{P}_{b,\mathrm{obs}} = -2.4056(51) \times 10^{-12}$. The agreement between the prediction and observation is at the $(0.13 \pm 0.21)\%$ level, that proves the existence of GWs. Figure 2.4 shows the observed and expected orbital decay of PSR B1913+16. This earned Hulse and Taylor the Nobel Prize in 1993 “for the discovery of a new type of pulsar, a discovery that has opened up new possibilities for the study of gravitation”.

2.1.1 Pulsar timing array

PTA utilizes the fact that pulse periods of MSPs are extremely stable. The detection principle of PTA is basically same as the interferometers. The passage of GWs past the Earth and/or a pulsar causes deviation of pulse times of arrival (ToAs) from the prediction in the absence of GWs, termed

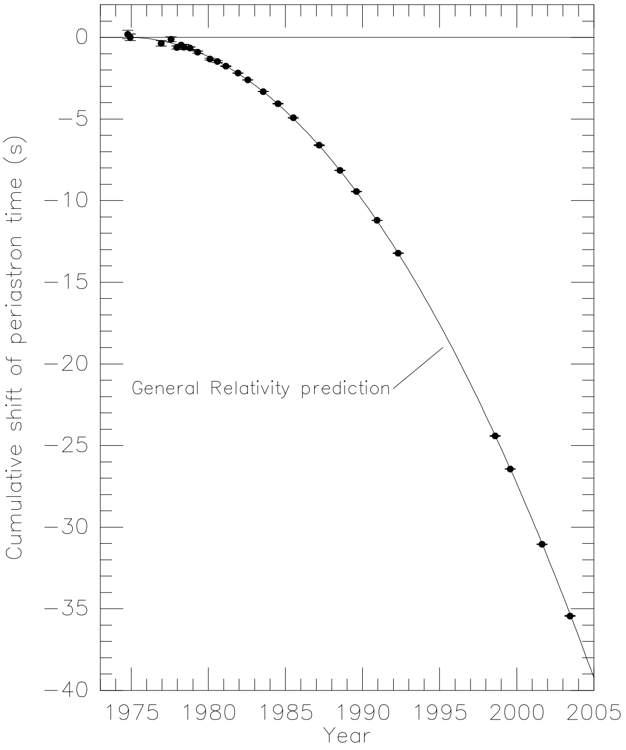

Figure 2.4: Orbital decay of PSR B1913+16 [114]. The points indicates the observed change in the epoch of periastron against data, while the parabola represents the theoretically predicted change in the epoch according to GR.

“timing residual” which is given by [36]

$$r_{\mathrm{GW}}(t) = \sum_{A=+,\times} F^A(\hat{\Omega}, \hat{p}) \int^t \Delta h_A(t', \hat{\Omega}) dt', \tag{2.44}$$

where $\hat{p}$ and $\hat{\Omega}$ are respectively the directions of the pulsar and of the GW propagation. Here, $F^A(\hat{\Omega}, \hat{p})$ is called the antenna pattern which is given by [10]

$$F^A(\hat{\Omega}, \hat{p}) = \frac{1}{2} \frac{\hat{p}^i \hat{p}^j}{1 + \hat{\Omega} \cdot \hat{p}} e^A_{ij}(\hat{\Omega}), \tag{2.45}$$

where e^A_{ij} is the GW polarization tensor given by

$$\begin{aligned} e^+_{ij}(\hat{\Omega}) &= \hat{m}_i\hat{m}_j - \hat{n}_i\hat{n}_j & (2.46)\\ e^\times_{ij}(\hat{\Omega}) &= \hat{m}_i\hat{n}_j + \hat{n}_i\hat{m}_j, & (2.47)\end{aligned}$$

where $\hat{m}$ and $\hat{n}$ are the polarization basis vectors. Here, $\Delta h_A(t,\hat{\Omega})$ is the difference of the metric perturbations, or GW amplitudes, between the Earth and pulsar and is given by

$$\Delta h_A(t,\hat{\Omega}) = h_A(t,\hat{\Omega}) - h_A(t_p,\hat{\Omega}), \tag{2.48}$$

where $t_p = t-\tau$ with $\tau = L/c(1+\hat{\Omega}\cdot\hat{p})$ is the pulse propagation time from the pulsar to the Earth, and L is the distance to the pulsar. In general, we can express Eq.(2.48) in terms of a plane-wave expansion given by

$$\Delta h_A(t,\hat{\Omega}) = \sum_{A=+,\times}\int_{-\infty}^{\infty} df \int_{S^2} d\hat{\Omega} h_A(f,\hat{\Omega}) e^{2\pi i f t}\left[1-e^{-2\pi i f L(1+\hat{\Omega}\cdot\hat{p})}\right]. \tag{2.49}$$

In the case of the stochastic GWB which is composed of a superposition of individually unresolvable single-sources, such a background is stationary, Gaussian and independently polarised, thus the GW amplitudes satisfy the statistical property

$$\langle h^*_A(f,\hat{\Omega}) h_{A'}(f',\hat{\Omega}')\rangle = \delta^2(\hat{\Omega},\hat{\Omega}')\delta(f-f')\delta_{A,A'}P(\hat{\Omega})H(f), \tag{2.50}$$

where $\langle\cdot\rangle$ represents the ensemble average, $H(f) = h_c^2(f)/(16\pi f)$ and $P(\hat{\Omega})$ are the spectral content of the radiation and the angular distribution on the sky. Here, $h_c(f)$ is the characteristic strain of the GWB in a frequency interval centered at f which is defined in the following section. Then, the cross correlation of timing residuals between pulsar a and b is given by

$$\langle r^*_a(t_0) r_b(t_0+t)\rangle = \int_0^{\infty} df\ \Gamma_{ab}(f)\frac{H(f)}{f^2}e^{2\pi i f t}, \tag{2.51}$$

where $\Gamma_{ab}(f)$ is the "overlap reduction function" which is given by

$$\begin{aligned} \Gamma_{ab}(f) &\equiv \int_{S^2} d\hat{\Omega} P(\hat{\Omega})\kappa_{ab}(f,\hat{\Omega})\left[\sum_{A=+,\times} F^A_a(\hat{\Omega})F^A_b(\hat{\Omega})\right] & (2.52)\\ \kappa_{ab}(f,\hat{\Omega}) &\equiv \left[1-e^{2\pi i f L_a(1+\hat{\Omega}\cdot\hat{p}_a)}\right]\left[1-e^{2\pi i f L_b(1+\hat{\Omega}\cdot\hat{p}_b)}\right]. & (2.53)\end{aligned}$$

The overlap reduction function is expanded using the spherical harmonics

$$\Gamma_{ab}(f) = \sum_{l=0}^{\infty}\sum_{m=-l}^{l} c_{lm}\Gamma^{(ab)}_{lm}(f), \tag{2.54}$$

where $\Gamma^{(ab)}_{lm}(f)$ is the "generalized overlap reduction function" or the "correlation bias-function" which is defined as

$$\Gamma^{(ab)}_{lm}(f) \equiv \int_{S^2} d\hat{\Omega}\ Y_{lm}(\hat{\Omega})\kappa_{ab}(f,\hat{\Omega})\left[\sum_{A=+,\times} F^A_a(\hat{\Omega})F^A_b(\hat{\Omega})\right]. \tag{2.55}$$

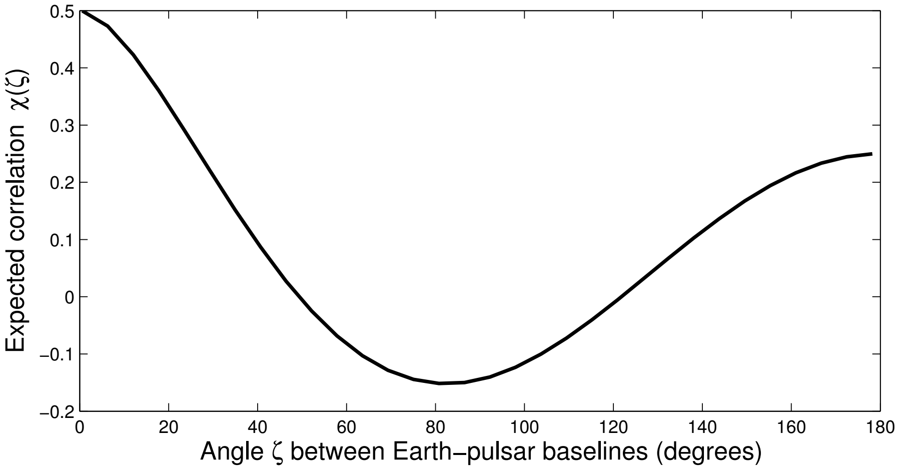

Figure 2.5: Hellings and Downs curve which describes the angular correlation of the isotropic GWB [59].

Here, c_{lm} in Eq.(2.54) describes degree of anisotropy. For all astrophysically relevant situations $fL \gg 1$, we obtain $\kappa_{ab}(f, \hat{\Omega}) \sim 1 + \delta_{ab}$ and $\Gamma_{lm}^{(ab)}(f)$ no longer depends on f. For the isotropic component, or $l = m = 0$, the generalized overlap-reduction function (2.55) is given by

$$\Gamma_{00} = N\frac{\sqrt{\pi}}{2}\left[1 + \frac{\cos\zeta}{3} + 4(-\cos\zeta)\ln\left(\sin\frac{\zeta}{2}\right)\right](1 + \delta_{ab}), \tag{2.56}$$

where ζ is the angle between pulsars a and b, and N is the normalization constant. The GWB is expected to be almost isotropic and therefore the angular correlation of the GWB could be approximated by Eq. (2.56), which this isotropic correlation is especially called "the Hellings and Downs curve" [50].

Constraints on GWs by the current PTA experiments

In the PTA frequency band, the dominant GW signal is expected to be the incoherent superposition of signals from inspiraling SMBH binaries, forming a stochastic GWB. One of the most significant quantities is the GWB spectrum, as a fractional contribution of the GWB to the energy density of the Universe in a logarithmic frequency interval, which is given by

$$\Omega_{\mathrm{GW}} \equiv \frac{1}{\rho_c}\frac{d\rho_{\mathrm{GW}}}{d\ln f} = \frac{\pi f^2 h_c^2(f)}{4G\rho_c}, \tag{2.57}$$

where ρ_c is the critical density for the Universe. Here, $h_c(f)$ is the characteristic strain spectrum given by

$$h_c^2(f) = \frac{4}{\pi f^2}\frac{d\rho_{\mathrm{GW}}(f)}{d\ln f} = \frac{4}{\pi f^2}\int_0^\infty \frac{dz}{1+z}\frac{dn}{dz}\frac{dE_{\mathrm{GW}}}{d\ln f_r}, \tag{2.58}$$

where dn/dz is the number of events generating GW emission (e.g. BH binary mergers) per unit redshift, $dE_{\mathrm{GW}}/d\ln f_r$ is the energy per unit logarithmic frequency emitted from one source, and

$f_r = (1+z)f$ is the GW frequency in the rest frame of the source. In the case the GW sources are SMBH binaries, the energy emitted per logarithmic frequency is given by

$$\frac{dE_{\rm GW}}{d\ln f_r} = \frac{\pi^{2/3}}{3}\mathcal{M}^{5/3} f_r^{2/3} F(e), \tag{2.59}$$

$$F(e) = \left(1-e^2\right)^{-7/2}\left(1+\frac{73}{24}e^2+\frac{37}{96}e^4\right), \tag{2.60}$$

where e is the eccentricity, assuming that the sources are in adiabatic state without interaction with surrounding stars and gas, and their orbits are larger than the innermost stable circular-orbit that allows us to describe the orbital motion with the Newtonian mechanics. Substituting Eq. (2.59) into Eq. (2.58) gives $h_c \propto f^{-2/3}$. The spectra of GWBs from other sources rather that inspiraling SMBH binaries is expected to be power spectra, thus they are generally given by

$$h_c(f) = A\left(\frac{f}{1{\rm yr}}\right)^{-\alpha}, \tag{2.61}$$

where A is the amplitude at $f = 1$ yr^{-1} and constant that depends on models of the GWBs. In the case that sources of the GWB are SMBH binaires, A depends on the mass function and number density of the binaries and the eccentricity. PTAs commonly give constraints on $\Omega_{\rm GW}(f)$, $h_c(f)$ or A.

Currently, three PTAs are in operation; Parkes PTA in Australia, European PTA and the North American Nanohertz Observatory for Gravitational Waves (NANOGrav), and these three PTAs compose the International PTA (IPTA). In the 2020s, the Square Kilometre Array (SKA) will start running. Recently, NANOGrav placed a 95% limit of the amplitude of $A < 1.45\times10^{-15}$ for a fiducial power-law spectrum with $\alpha = -2/3$ [11]. PTAs provide constraints on other GW sources such as continuous GWs from individual SMBH bianries [9, 12, 117] and GW bursts with memory [113], and the dark matter density of ultralight bosons which induce periodic oscillations in gravitational potentials [95].

2.2 Cosmic string

Cosmic strings are hypothetical one-dimensional topological defects which are configurations of scalar and/or gauge fields whose energy density is concentrated along an infinite line or a closed loop. They are predicted by quantum field theory or superstring theory to be formed in the early Universe during a symmetry-breaking phase transitions in extension of the Standard Model. They were first proposed as a possible explanation for early Universe structure formation [37, 61, 63, 100, 111] with symmetry breaking at the grand unification scale. Several cosmological inflationary models based on superstring theory predicted defects such as fundamental strings, D-strings or bound states at cosmological scale that may have left signatures in the early Universe through their nonlinear evolution.

Global and local strings

First, let us discuss the prototype example given by the breaking of a $U(1)$ symmetry, due to a complex scalar field Φ whose potential is the standard Mexican hat potential and given by

$$V(\Phi) = \frac{1}{4}\lambda\left(|\Phi|^2 - \eta^2\right)^2, \tag{2.62}$$

where λ is a dimensionless coupling constant and η is the vacuum expectation value. If we describe $\Phi = |\Phi|e^{i\psi}$, that leads to $|\Phi| = \eta$ at the minimum of the potential, but the phase ψ is undetermined. This means that there is not just a single vacuum state, but a whole vacuum manifold which is a circle parametrized by an angle ψ with $0 \leq \psi \leq 2\pi$ in this case. As we go around a closed path in physical space, the phase ψ must vary by $\Delta\psi = 2\pi n$ for $n = 0, \pm1, \pm2, ...$ since Φ is a single value. In the case of $n \neq 0$, as we go around a close path in physical space, the phase ψ wraps one or more times around this closed path in the field space, and there can be strings which is a configuration that is topologically non-trivial and can not be continuously contracted to the topologically trivial point $\psi = 0$. Notice that at the center of the string $|\Phi| = 0$ and ,thus the energy density is non-zero at the string core.

The simplest theory exhibiting string solutions is described by the Lagrangian density

$$\mathcal{L} = -\partial_\mu\Phi\partial^\mu\Phi^* - V(\Phi). \tag{2.63}$$

For $n \neq 0$, we can have an ansatz

$$\Phi(x) = \left(\eta + \frac{\varphi(x)}{\sqrt{2}}\right)e^{i\psi(x)}, \tag{2.64}$$

and we obtain

$$\begin{aligned}\mathcal{L} &= -\frac{1}{2}\partial_\mu\varphi\partial^\mu\varphi - \frac{\lambda}{4}\left(\sqrt{2}\eta\varphi + \frac{1}{2}\varphi^2\right)^2 - \left(\eta + \frac{\varphi}{\sqrt{2}}\right)^2\partial_\mu\psi\partial^\mu\psi \\ &= \mathcal{L}_2 + \mathcal{L}_{\text{int}},\end{aligned} \tag{2.65}$$

where the quadratic term is given by

$$\mathcal{L}_2 = -\frac{1}{2}\partial_\mu\varphi\partial^\mu\varphi - \frac{1}{2}m_s^2\varphi^2 - \eta^2\partial_\mu\psi\partial^\mu\psi \tag{2.66}$$

with $m_s^2 = \lambda\eta^2$, and $\mathcal{L}_{\text{int}}$ is the interaction term. The expressions above therefore indicate a massive scalar field φ with mass of m_s and a massless scalar field ψ which is the Goldstone boson associated with the breaking of the global $U(1)$ symmetry.

The equation of motion, or the Euler-Lagrange equation, that follows from the Lagrangian (2.63) is

$$\Box\Phi = \frac{\lambda}{2}\left(|\Phi|^2 - \eta^2\right)\Phi. \tag{2.67}$$

Besides the vacuum, we can look for a static solution representing a string along the z axis which is given by

$$\Phi(\rho, \theta) = \eta f(m_s\rho)e^{in\theta}, \tag{2.68}$$

where (ρ, θ) are polar coordinates in the (x, y) plane and the integer n is the winding number of the string. We notice that this solution implies $\psi(\rho, \theta) = n\theta$ in terms of the phase ψ of the field Φ. We then find that $f(m_s\rho) \propto \rho^{|n|}$ near the origin while, for $m_s\rho \gg 1$,

$$f(m_s\rho) \simeq 1 - \mathcal{O}\left(\frac{1}{m_s^2\rho^2}\right). \tag{2.69}$$

The energy density of this configuration is

$$\begin{aligned} \mathcal{E} &= \partial_i\Phi\partial_i\Phi^* + V(\Phi) &(2.70)\\ &= |\partial_\rho\Phi|^2 + \frac{1}{\rho^2}|\partial_\theta\Phi|^2 + V(\Phi), &(2.71) \end{aligned}$$

which is peaked around $\rho \sim m_s^{-1}$ and falls off as $1/\rho^2$ at large distances, and this means that this configuration describes a localized string. When integrating $\mathcal{E}$ over $d\rho d\theta$ in order to obtain the total energy of the string per unit length, however, the $1/\rho^2$ behavior is unntegrable and the energy per unit length diverges weakly. The string tension (i.e. the energy per unit length) is given by

$$\mu = 2\pi n^2\eta^2 \log(m_s R), \tag{2.72}$$

where R is the infrared cutoff, and we have adopted m_s^{-1} as the order of magnitude of the distance where the asymptotic behavior (2.69) is no longer effective. This string solution is known as a "global" string since there are no gauge fields in the model.

Next, let us consider a model of the spontaneous breaking of a local $U(1)$ symmetry. The Lagrangian density could be extended to be the Abelian Higgs model requiring the introduction of a vector field A_μ which is given by

$$\mathcal{L} = -|D_\mu\Phi|^2 - V(\Phi) - \frac{1}{4}F_{\mu\nu}F^{\mu\nu}, \tag{2.73}$$

where again $V(\Phi)$ is given by Eq.(2.62), the covariant derivative is given by $D_\mu\Phi = (\partial_\mu - igA_\mu)\Phi$ and $F_{\mu\nu} = \partial_\mu A_\nu - \partial_\nu A_\mu$. This system has also static string-like solutions in the forms of

$$\begin{aligned} \Phi(\rho, \theta) &= \eta f(\rho)e^{in\theta}, &(2.74)\\ A_A &= -\epsilon_{AB}x_B\frac{n}{g\rho^2}\alpha(\rho), &(2.75) \end{aligned}$$

where ϵ_{AB} is the Levi-Civita symbol, $A, B = 1, 2$ correspond to the x and y directions, and $f(\rho)$ and $\alpha(\rho)$ are two functions. In this case, the problem has two mass scales, $m_s = \lambda^{1/2}\eta$ which is mass of a massive Higgs field that appears in the model of global symmetry breaking and $m_v = g\eta$ which is mass of a massive gauge boson, thus $f(\rho)$ no longer depends on the combination of $m_s\rho$. Taking this ansatz into account we find from the equation of motion that at large distances the field Φ goes asymptotically to the value

$$\Phi \to \eta e^{in\theta}, \tag{2.76}$$

as in the global case, while, simultaneously

$$A_\mu \to \frac{n}{g}\partial_\mu\theta. \tag{2.77}$$

We see that this configuration contains a quantized magnetic flux,

$$\int_S d\mathbf{S}\cdot\mathbf{B} = \int_C d\mathbf{l}\cdot\mathbf{A} = \frac{2\pi n}{g} \tag{2.78}$$

where C is a closed curve bounding the surface S. This configuration is called the Nielsen-Olesen vortex and describes a local string. Since the gauge field contribution cancels the scalar field one, $D_\mu\Phi \to 0$ as $\rho \to \infty$. Therefore, the string tension of a local string is finite and given by setting to $n = 1$

$$\mu = 2\pi\eta^2 g(\beta), \tag{2.79}$$

where $\beta = (m_s/m_v)^2 = \lambda/g^2$ and $g(\beta)$ satisfies $g(1) = 1$.

String dynamics

Although the dynamics of the Nielsen-Olesen vortex depends on the underlying scalar and gauge field, the internal structure of the vortex could be neglected so that we can regard the string as a one-dimensional object for scales much larger than the characteristic thickness of the string. The dynamics of such a string is given by generalizing that of a relativistic point particle. Here, we introduce a variable τ that parametrizes the world-line of the particle and describe the particle with using four functions $X^\mu(\tau)$ for $\mu = 0, ..., 3$. For this parametrization of the world-line, we impose invariance since our way of parametrization is arbitrary. Under transformation $\tau \to \tilde{\tau}(\tau)$, $X^\mu(\tau) \to \tilde{X}^\mu(\tilde{\tau})$ such that $\tilde{X}^\mu(\tilde{\tau}) = X^\mu(\tau)$, and we require an action governing $X^\mu(\tau)$ to be invariant. The action of a point-like massive particle in a curved space with a metric $g_{\mu\nu}$ is given by

$$S_{pp} = -m\int ds, \tag{2.80}$$

where $ds^2 = -g_{\mu\nu}(X)dX^\mu(\tau)dX^\nu(\tau)$. This action is apparently invariant since ds is the invariant length. We can write Eq. (2.80) as

$$S_{pp} = -m\int d\tau \left(-g_{\mu\nu}\dot{X}^\mu\dot{X}^\nu\right)^{\frac{1}{2}}, \tag{2.81}$$

with using $dX^\mu(\tau) = \dot{X}^\mu d\tau$, where the dot denotes the derivative with respect to τ. The square root could be removed by introduction of an auxiliary field $e(\tau)$ and then it leads to

$$S_{pp} = \frac{1}{2}\int d\tau \left(e^{-1}g_{\mu\nu}\dot{X}^\mu\dot{X}^\nu - em^2\right). \tag{2.82}$$

This action is invariant under transformation $\tau \to \tilde{\tau}(\tau)$ associated $X^\mu(\tau) \to \tilde{X}^\mu(\tilde{\tau})$ and $e(\tau) \to \tilde{e}(\tilde{\tau})$ that leads to

$$\begin{aligned} \tilde{X}^\mu(\tilde{\tau}) &= X^\mu(\tau), && (2.83) \\ \tilde{e}^\mu(\tilde{\tau})d\tilde{\tau} &= X^\mu(\tau)d\tau. && (2.84) \end{aligned}$$

Notices that Eq. (2.82) exhibits a well-defined massless limit, whereas it is not the case for Eq. (2.80).

The dynamics of the particle is generalized to that of a string by parametrization of the world-sheet by a space-like parameter σ in addition to a time-line one τ. Then, the position of the string in space-time is now represented by the four functions $X^\mu(\tau,\sigma)$, and we describe the position of the point of the world-sheet in space-time as $x^\mu = X^\mu(\tau,\sigma)$. The point-particle action is generalized to the Nambu-Goto action given by

$$S_{NG} = -\mu \int d^2\zeta\sqrt{-h}, \tag{2.85}$$

where $\zeta^a = (\tau,\sigma)$ for $a = 1,2$ respectively corresponding to τ and σ. Here, $h = \det h_{ab}$, where

$$h_{ab} = g_{\mu\nu}(X)\partial_a X^\mu \partial_b X^\nu \tag{2.86}$$

is the induced metric which is the metric induced on this surface by the embedding in the background space-time through the functions $X^\mu(\tau,\sigma)$. Under transformation of the world-sheet $\zeta \to \tilde{\zeta}(\zeta)$, the four functions X^μ transform as scalars,

$$X^\mu(\zeta) \to \tilde{X}^\mu(\tilde{\zeta}) = X^\mu(\zeta). \tag{2.87}$$

Consequently, h_{ab} transforms as a metric tensor on the world-sheet, and therefore the Nambu-Goto action is invariant. In the same way of the point-particle case, the square root in the Nambu-Goto action (2.85) could be removed by introducing an auxiliary field γ_{ab}, which is a tensor in this case, with Lorentzian signature $(-,+,+,+)$. In fact, the Nambu-Goto action is equivalent to the Polyakov action which is given by

$$S_P = -\frac{\mu}{2}\int d^2\zeta\sqrt{-\gamma}\gamma^{ab}g_{\mu\nu}(X)\partial_a X^\mu \partial_b X^\nu, \tag{2.88}$$

where $\gamma = \det \gamma_{ab}$. This could be derived from variation with respect to γ_{ab}, that gives $\gamma_{ab} = \kappa h_{ab}$, where κ is an arbitrary constant. We can get back to the Nambu-Goto action by substituting this relation into Eq. (2.88) due to cancellation of κ between $\sqrt{-\gamma}$ and γ^{ab} and $h^{ab}g_{\mu\nu}\partial_a X^\mu \partial_b X^\nu = h^{ab}h_{ab} = 2$. In the Polyakov formulation, the theory is invariant under transformation (2.87), whereas γ_{ab} transforms as a metric below,

$$\gamma_{ab}(\zeta) \to \tilde{\gamma}_{ab}(\tilde{\zeta}) = \gamma_{cd}(\zeta)\frac{\partial\zeta^c}{\partial\tilde{\zeta}^a}\frac{\partial\zeta^d}{\partial\tilde{\zeta}^b}. \tag{2.89}$$

Further, in this formulation, there is an invariance under Weyl transformation, in which the world-sheet coordinates ζ^a are not changed, whereas

$$\gamma_{ab} \to e^{2\omega(\zeta)}\gamma_{ab}. \tag{2.90}$$

The use of the Weyl symmetry (2.90) allows us to set $\kappa = 1$, and therefore the equation of motion is derived by variation of the action (2.88) with respect to X^μ which is given by

$$\partial_a\left(\sqrt{-h}h^{ab}\partial_b X^\mu\right) = 0. \tag{2.91}$$

Eq. (2.91) generally depends on X^μ non-linearly since h_{ab} is itself a functional of X^μ expressed by Eq. (2.86). However, this equation could be simplified by using the two-dimensional diffeomorphism invariance and fixing the gauge. The two-dimensional diffeomorphism invariance provides us two gauge conditions which it is convenient to require

$$h_{01} = 0 \tag{2.92}$$

and

$$h_{00} + h_{11} = 0. \tag{2.93}$$

Consequently, h_{ab} can be written by

$$h_{ab} = e^{\phi}\eta_{ab}, \tag{2.94}$$

that means the world-sheet metric conformally flat. Therefore, this gauge is called the conformal gauge. We find from this gauge choice that $-h = e^{2\phi}$ and $h^{ab} = e^{-\phi}\eta^{ab}$. Thus, the conformal factor is canceled in the combination $\sqrt{-h}h^{ab}$ in Eq. (2.91), and we obtain a simple linear equation

$$\left(-\partial_\tau^2 + \partial_\sigma^2\right) X^\mu = 0, \tag{2.95}$$

which is the Klein-Gordon equation in two-dimensional flat space. In the case of $g_{\mu\nu} = \eta_{\mu\nu}$, furthermore, the gauge conditions (2.92) and (2.93) give respectively

$$\eta_{\mu\nu}\partial_\sigma X^\mu \partial_\tau X^\nu = 0, \tag{2.96}$$

$$\eta_{\mu\nu}\left(\partial_\sigma X^\mu \partial_\sigma X^\nu + \partial_\tau X^\mu \partial_\tau X^\nu\right) = 0, \tag{2.97}$$

by using Eq. (2.86). These two equations do not include the second derivative with respect to τ and thus constrain the initial values of $\partial_\tau X^\mu$ and $\partial_\sigma X^\mu$ which are conserved by time evolution.

Let us now consider a transformation $\zeta^a \to \tilde{\zeta}^a(\zeta)$ (i.e. $\tau \to \tilde{\tau}(\tau,\sigma)$ and $\sigma \to \tilde{\sigma}(\tau,\sigma)$) to further simplify the dynamics of the string since only the conditions (2.92) and (2.93) can not take degrees of freedom of the gauge away completely. The transformation of the metric h_{ab} is the same as that of γ_{ab} in Eq. (2.89). We obtain

$$\partial_\tau\tilde{\tau}\partial_\sigma\tilde{\tau} = \partial_\tau\tilde{\sigma}\partial_\sigma\tilde{\sigma} \tag{2.98}$$

by using Eqs. (2.92) and (2.93) and requiring that $\tilde{h}_{01} = 0$, and

$$(\partial_\tau\tilde{\tau})^2 + (\partial_\sigma\tilde{\tau})^2 = (\partial_\tau\tilde{\sigma})^2 + (\partial_\sigma\tilde{\sigma})^2 \tag{2.99}$$

by requiring $\tilde{h}_{00} + \tilde{h}_{11} = 0$. We can obtain a solution of Eqs. (2.98) and (2.99) by using $\tilde{\sigma}(\tau,\sigma)$ and $\tilde{\tau}(\tau,\sigma)$ which satisfy conditions

$$\partial_\tau\tilde{\sigma} = \partial_\sigma\tilde{\tau}, \tag{2.100}$$

$$\partial_\sigma\tilde{\sigma} = \partial_\tau\tilde{\tau}. \tag{2.101}$$

Differentiating the first equation with respect to σ and τ and using the second one gives respectively

$$\left(-\partial_\tau^2 + \partial_\sigma^2\right)\tilde{\tau} = 0, \tag{2.102}$$

$$\left(-\partial_\tau^2 + \partial_\sigma^2\right)\tilde{\sigma} = 0. \tag{2.103}$$

A function $\tilde{\tau}$ satisfies Eq. (2.102) whereas is arbitrary, so then we fix the gauge $X^0(\tau,\sigma) = 0$ with using it since X^0 also satisfies Eq. (2.95). The gauge fixing is now complete since the the derivative of the function $\tilde{\sigma}$ is fixed by fixing $\tilde{\tau}(\tau,\sigma)$. In this gauge choice, therefore, X^0 is no longer the dynamical variable, and use of the notation $X^0 \equiv t$ gives $\tau = t$. Hence, the string is now given by a vector $\mathbf{X}(t,\sigma)$ and Eqs. (2.95) – (2.97) are rewritten as

$$\begin{aligned}\ddot{\mathbf{X}} - \mathbf{X}'' &= 0, & (2.104)\\ \dot{\mathbf{X}} \cdot \mathbf{X}' &= 0, & (2.105)\\ \dot{\mathbf{X}}^2 + \mathbf{X}'^2 &= 0, & (2.106)\end{aligned}$$

where the dot and prime denote the derivatives with respect to t and σ, respectively. The general solution to the wave equation (2.104) is described as a superposition of left- and right-moving waves,

$$\mathbf{X}(\tau,\sigma) = \frac{1}{2}\left[\mathbf{a}(\sigma-\tau) + \mathbf{b}(\sigma+\tau)\right], \qquad (2.107)$$

where $\mathbf{a}$ and $\mathbf{b}$ are arbitrary vector functions with one variable. The constrains (2.105) and (2.106) give

$$\mathbf{a}'^2 = \mathbf{b}'^2 = 1. \qquad (2.108)$$

The energy-momentum tensor of the string is obtained with using the Polyakov action (2.88),

$$\begin{aligned}T^{\mu\nu}(x) &= \frac{2}{\sqrt{-g}}\frac{\delta S}{\delta g_{\mu\nu}(x)}\\ &= -\mu\int d^2\zeta\sqrt{-h}h^{ab}\frac{1}{\sqrt{-g}}\delta^{(4)}(x-X)\partial_a X^\mu \partial_b X^\nu, \qquad (2.109)\end{aligned}$$

where the equation of motion $\gamma^{ab} = h^{ab}$ has been used after taking variation with respect to $g_{\mu\nu}$. In flat space, the conformal gauge (2.94) leads to

$$T^{\mu\nu}(x) = \mu\int d^2\zeta\delta^{(4)}(x-X)\left[\partial_\tau X^\mu \partial_\tau X^\nu - \partial_\sigma X^\mu \partial_\sigma X^\nu\right]. \qquad (2.110)$$

Further imposing $X^0(\tau,\sigma) = \tau$ that fixes the residual gauge freedom, the energy density $\rho(x) = T^{00}$ is represented as

$$\begin{aligned}\rho(t,\mathbf{x}) &= \mu\int d\sigma d\tau\delta^{(3)}[\mathbf{x}-\mathbf{X}(\tau,\sigma)]\delta(t-\tau)\\ &= \mu\int d\sigma\delta^{(3)}[\mathbf{x}-\mathbf{X}(t,\sigma)]. \qquad (2.111)\end{aligned}$$

Therefore, the total energy is given by

$$\begin{aligned}E &= \int dx^3\rho(x)\\ &= \mu\int d\sigma. \qquad (2.112)\end{aligned}$$

In this gauge, we see that σ means a measure of length on the string, given by $d\sigma = dE/\mu$. The momentum is similarly given by

$$\begin{aligned} P^i &= \int dx^3 T^{0i} \\ &= \mu \int d\sigma \dot{X}^i. \end{aligned} \tag{2.113}$$

Now, let us consider a closed loop. Eq. (2.112) indicates that the parameter σ ranges from 0 to L, where $L = E/\sigma$ is called the invariant length of the loop. For a closed loop, a periodic boundary condition is required given by $\mathbf{X}(t, \sigma + L) = \mathbf{X}(t, \sigma)$. In terms of $\mathbf{a}$ and $\mathbf{b}$ introduced in Eq.(2.107), the boundary condition could be written as

$$\begin{aligned} -\mathbf{a}(\sigma + L - t) + \mathbf{a}(\sigma - t) &= \mathbf{b}(\sigma + L + t) - \mathbf{b}(\sigma + t) \\ &\equiv \boldsymbol{\Delta}. \end{aligned} \tag{2.114}$$

The vector $\boldsymbol{\Delta}$ is independent of σ due to invariance under transformation in the world-sheet. The momentum (2.113) is given by

$$\begin{aligned} \mathbf{P} &= \frac{\mu}{2} \int_0^L d\sigma \left[\partial_t \mathbf{a}(\sigma - t) + \partial_t \mathbf{b}(\sigma + t)\right] \\ &= \frac{\mu}{2} \int_0^L d\sigma \left[-\partial_\sigma \mathbf{a}(\sigma - t) + \partial_\sigma \mathbf{b}(\sigma + t)\right] \\ &= \frac{\mu}{2} \left[-\mathbf{a}(L - t) + \mathbf{a}(-t) + \mathbf{b}(L + t) - \mathbf{b}(t)\right] \\ &= \mu \boldsymbol{\Delta}. \end{aligned} \tag{2.115}$$

In the center-of-mass frame of the string defined as $\mathbf{P} = 0$, $\boldsymbol{\Delta} = 0$ and we find from Eq. (2.114) that $\mathbf{a}$ and $\mathbf{b}$ are independently periodic

$$\mathbf{a}(\sigma + L - t) = \mathbf{a}(\sigma - t), \tag{2.116}$$

$$\mathbf{b}(\sigma + L + t) = \mathbf{b}(\sigma + t). \tag{2.117}$$

As can be seen from this formalism, cusps emerge in the generic motion of a string. From Eq. (2.107), in fact, we obtain

$$(\partial_t \mathbf{X})^2 = \frac{1}{4}(-\mathbf{a}' + \mathbf{b}')^2. \tag{2.118}$$

This equation shows that the world-sheet moves at the speed of light at a point such that $\mathbf{a}' = -\mathbf{b}'$ using Eq. (2.108). As can be seen from Eq. (2.108), the functions $\mathbf{a}'(\sigma - t)$ and $\mathbf{b}'(\sigma + t)$ sweep on the unit sphere because of $0 \leq \sigma \leq L$, and Eqs. (2.116) and (2.117) indicate that they are closed curves on the sphere. Moreover, these periodic boundary conditions (2.116) and (2.117) imply that

$$\int_0^L d\sigma \mathbf{a}' = \int_0^L d\sigma \mathbf{b}' = 0, \tag{2.119}$$

therefore, these curves can not be restricted to a single sphere. This means that these curves swept by $\mathbf{a}'(\sigma - t)$ and $-\mathbf{b}'(\sigma + t)$ will generally intersections which are points on the world-sheet that travel at the speed of light. The intersection point of the string travels at the speed of light only for an instant. When this is caused, the spatial configuration of the string forms a cusp. Here, we take the point of the world-sheet that travels at the speed of light corresponding to $\tau = \sigma = 0$ as the origin of the world-sheet coordinates. We also choose $\mathbf{x} = 0$ at $\tau = 0$ and $\mathbf{a} = \mathbf{b} = 0$ as the origin of the spatial coordinates, and use the gauge $t = \tau$ again. The functions $\mathbf{a}(\sigma_-)$ and $\mathbf{b}(\sigma_+)$ could be expanded in power of $\sigma_\pm \equiv \sigma \pm t$ around the point $t = \sigma = 0$ (i.e. $\sigma_- = \sigma_+ = 0$) which are given

$$\begin{aligned} \mathbf{a}(\sigma_-) &= \mathbf{a_0}'\sigma_- + \frac{1}{2}\mathbf{a}_0''\sigma_-^2 + \frac{1}{6}\mathbf{a}_0'''\sigma_-^3 + \dots , && (2.120) \\ \mathbf{b}(\sigma_+) &= \mathbf{b_0}'\sigma_+ + \frac{1}{2}\mathbf{b}_0''\sigma_+^2 + \frac{1}{6}\mathbf{b}_0'''\sigma_+^3 + \dots , && (2.121) \end{aligned}$$

and, therefore, we obtain

$$\begin{aligned} \mathbf{a}'(\sigma_-) &= \mathbf{a_0}' + \mathbf{a}_0''\sigma_- + \dots , && (2.122) \\ \mathbf{b}'(\sigma_+) &= \mathbf{b_0}' + \mathbf{b}_0''\sigma_+ + \dots . && (2.123) \end{aligned}$$

The condition that the curves swept by $\mathbf{a}'(\sigma - t)$ and $-\mathbf{b}'(\sigma + t)$ cross at $\sigma = \tau = 0$ gives $\mathbf{a}_0' = -\mathbf{b}_0'$. Therefore, at $t = 0$, Eq. (2.107) leads to

$$\mathbf{X}(0, \sigma) = \frac{1}{4}\left(\mathbf{a}_0'' + \mathbf{b}_0''\right)\sigma^2 + \frac{1}{6}\left(\mathbf{a}_0''' + \mathbf{b}_0'''\right)\sigma^3 + \dots . \qquad (2.124)$$

In the case of $(\mathbf{a}_0'' + \mathbf{b}_0'') \neq 0$, we take axes such that $(\mathbf{a}_0'' + \mathbf{b}_0'')$ points along the x axis, and then, in the (x, y) plane, we have

$$\begin{aligned} X_x(0, \sigma) &\simeq c_x\sigma^2, && (2.125) \\ X_y(0, \sigma) &\simeq c_y\sigma^3, && (2.126) \end{aligned}$$

where $c_x = (1/4)|\mathbf{a}_0'' + \mathbf{b}_0''|$ and $c_y = (1/6)(\mathbf{a}_0'' + \mathbf{b}_0'')_y$ with the assumption of $c_y \neq 0$. The shape of the string can be written by $X_x^3(0, \sigma) \propto X_y^2(0, \sigma)$ near $\sigma = 0$. The velocity of the string at this point is orthogonal to the direction of the cusp which can be seen by substituting Eqs. (2.122) and (2.123) into Eq. (2.108) and imposing that it be satisfied order by order in σ that gives

$$\begin{aligned} &|\mathbf{a}_0'| = |\mathbf{b}_0'| = 1, && (2.127) \\ &\mathbf{a}_0' \cdot \mathbf{a}_0'' = \mathbf{b}_0' \cdot \mathbf{b}_0'' = 0 && (2.128) \end{aligned}$$

Therefore, the direction of the cusp given by $(\mathbf{a}_0'' + \mathbf{b}_0'')$ is orthogonal to the that of the velocity given by $(1/2)(-\mathbf{a}_0' + \mathbf{b}_0') = \mathbf{b}_0'$ because of $\mathbf{a}_0' = -\mathbf{b}_0'$

Here, we note that the configuration of the cusp is generated due to the zero-thickness approximation implicit in the Nambu-Goto action. For the Nielsen-Olesen vortex, the inner structure smooths the configuration on the scales m_s^{-1} and m_v^{-1} and makes the velocity smaller that the speed of light. However, the scale of this smoothing is much smaller than typical length of the cosmic strings with the horizon-scale in which we are interested. Thus, the Nambu-Goto approximation is a realistic description of the dynamics of the cusp. Actually, there is a kink which is another significant structure that can develop on cosmic strings. Since we work on cusps, however, we do not mention it in detail.

2.2.1 GW bursts from cusps and their signal in pulsar timing

Cusps on the cosmic strings can generate GW bursts so strong which potentially could be detected individually as well as their stochastic GWB. The spectral shape of GWs from a cusp was first investigated in [33] and found to follow a simple power law $\propto |f|^{-4/3}$. The strain amplitude in the frequency domain $\tilde{h}(f) = \int dt e^{2\pi i f t} h(t)$ is given in terms of the string tension $G\mu$ and the loop size l as

$$\tilde{h}(f) = \frac{G\mu l}{[(1+z)fl]^{1/3} r(z) f}\,, \tag{2.129}$$

where $r(z)$ is the distance to the GW source at redshift z. For a field theoretical string, the tension value is close to the square of the energy scale of the spontaneously super-symmetry breaking.

The string loop cannot emit GWs of wavelength larger than its size l. Thus, the spectrum peaks at $f = f_l \equiv (l/2)^{-1}$ and is cut off below this frequency. This lowest frequency, determined by the loop size, also gives the duration of the GW event as $T_l = l/2 = f_l^{-1} \equiv W/2$, where W is the duration of the GW burst. Thus, searching bursts for different durations W corresponds to searching for cosmic string loops of different loop size.

The GW from a cusp is linearly polarized and, for a plus-polarized event, the time-domain waveform is given by

$$h_+(t) = \begin{cases} A_{\rm fit}\left[|t-t_0|^{1/3} - \left(\tfrac{1}{2}W\right)^{1/3}\right] & (t_0 - \tfrac{1}{2}W \le t < t_0 + \tfrac{1}{2}W) \\ 0 & \text{(otherwise)}, \end{cases} \tag{2.130}$$

$$h_\times(t) = 0, \tag{2.131}$$

where $A_{\rm fit}$ is the amplitude, t_0 is the epoch when the burst peak reaches the Earth. Cosmic string loops are considered to generate cusps efficiently ($\mathcal{O}(1)$ per oscillation period) and the GW burst is highly beamed along the direction of cusp velocity. The direction varies depending on the string configuration and is considered to be random each time [19]. The directions of acceleration and velocity of the cosmic string are, respectively, along the polarization basis vector $\hat{m}$ and the one of GW propagation $\hat{\Omega}$ defined below [34]. Note that $A_{\rm fit}$ has dimensionality of sec$^{-1/3}$. We define the dimensionless amplitude, which corresponds to the peak amplitude at $t = t_0$, as

$$A_{\rm peak} \equiv h_+(t_0) = \left(\frac{1}{2}W\right)^{1/3} A_{\rm fit}. \tag{2.132}$$

Let us define $\tilde{A}_f \equiv \frac{G\mu \cdot l^{2/3}}{(1+z)^{1/3} r(z)}$ so that the Fourier amplitude can be written in the simple form $h(f) = \tilde{A}_f |f|^{-4/3}$. Then, taking the inverse Fourier transform, we find that the strain amplitude using the physical parameters is

$$h(t) = \sqrt{\frac{3}{2\pi}}\Gamma(-\tfrac{1}{3})\tilde{A}_f |t|^{1/3}\,. \tag{2.133}$$

The coefficient $\sqrt{\frac{3}{2\pi}}\Gamma(-\frac{1}{3})\tilde{A}_f$ corresponds to $A_{\rm fit}$ in Eq. (2.130). This function implies $h(t=0) = 0$, but the offset of the amplitude can change since the full waveform is the sum of Eq. (2.133) and a slowly varying component due to the low modes of the string. However, only the relative difference

Δh is important for PTA observations, and the offset does not matter. In fact, we add the offset $(W/2)^{1/3}A_{\rm fit}$ in Eq. (2.130) in order to set $h(t = t_0 \pm W/2) = 0$, but it is absorbed when we fit the pulse frequency and it does not affect the post-fit residuals.

The important feature is that the function is spiky at $t = 0$. (In Eq. (2.130), we generalize the position of the spike by adding t_0.) This sharp spike in $h(t)$ leaves the feature in the timing residual as shown in Fig. 2.6. Finally, considering that the time scale of the GW event is given by $T_l = f_l^{-1}$, the peak amplitude, Δh, can be written in terms of the Fourier amplitude as

$$A_{\rm peak} \sim \sqrt{\frac{3}{2\pi}}\Gamma(-\tfrac{1}{3})\tilde{A}_f T_l^{1/3} = \sqrt{\frac{3}{2\pi}}\Gamma(-\tfrac{1}{3})\tilde{h}(f_l)f_l\,. \tag{2.134}$$

This corresponds to the dimensionless amplitude in Eq. (2.132).

Note that Eq. (2.129) has a high frequency cut-off if the observer does not lie exactly along the direction of the cusp velocity. This cut-off rounds off the spike in the time-domain waveform and reduces the amplitude of the timing residual. Since the timing residual is the cumulative of Δh as in Eq. (2.44), the shape of the timing residual is not changed much except for the amplitude. Thus, it does not affect the analysis performed in the previous section, though the effect on the amplitude should be taken into account when we consider constraints on string parameters.

Here we roughly estimate how much the timing residual is reduced. According to [34], the spike is smoothed by a time interval of order $|t - t_0| \sim \theta^3 T_l$, where θ is the angle (in radians) between the direction of emission and the cusp velocity. Thus, the peak amplitude is reduced by a factor of $(1 - \theta^3)^{1/3}$. In the Fourier space, it means that modes with frequencies higher than $|f| \sim (\theta^3 T_l)^{-1}$ exponentially decay. Here, we find that, for $\theta \gtrsim 1$, even the lowest frequency $f_l = T_l^{-1}$ is smoothed out, so that the maximum angle we can observe the GW is $\theta \sim 1$. In other words, the GW burst from a cusp is highly beamed in the angle of $\theta < 1$. Taking an average in the solid angle of $\Omega = 2\pi(1-\cos[1])$, we find that the typical smoothing time scale is $|t - t_0| = \frac{T_l}{\Omega}\int_0^{2\pi} d\phi \int_0^1 d\theta \sin\theta \cdot \theta^3 \simeq 0.39 T_l \simeq 0.2W$, and the amplitude is reduced by a factor of $\beta = \frac{1}{\Omega}\int_0^{2\pi} d\phi \int_0^1 d\theta \sin\theta (1 - \theta^3)^{1/3} \simeq 0.81$.

One may think that we can observe a GW burst with a width larger than the observation time, $W > T_{\rm obs} \simeq 4400$ days (12 years), if the spiky shape lies within the observation period. However, such bursts are typically smoothed out by this high-frequency cut-off as the spiky feature is rounded off for $|t - t_0| < 0.2W$, which means that we do not see the typical cusp-origin GW shape in the range of observation period if $W > 5T_{\rm obs}$.

The analytic expressions of the pre-fit timing residual induced by the GW burst from a cosmic string cusp are derived by substituting Eq.(2.130) into Eq.(2.44) using $A_{\rm fit}$,

$$r(t) \;=\; F^+(\hat{\Omega},\hat{p})\begin{cases} 0 & (t < t_0 - \frac{W}{2}) \\[2ex] A_{\rm fit}\left[\frac{3}{4}\left\{\left(\frac{W}{2}\right)^{4/3} \mp |t - t_0|^{4/3}\right\} - \left(\frac{W}{2}\right)^{1/3}\left\{t - \left(t_0 - \frac{W}{2}\right)\right\}\right] & (t_0 - \frac{W}{2} \le t < t_0 + \frac{W}{2}) \\[2ex] -\frac{1}{4}\left(\frac{1}{2}\right)^{1/3} A_{\rm fit} W^{4/3} & (t \ge t_0 + \frac{W}{2}) \end{cases} \tag{2.135}$$

Regarding the sign $\mp$ in the second line, $-$ should be applied to the epoch before t_0 and $+$ afterwards. In Fig. 2.6, we show examples of the waveform and simulated timing residuals (without the antenna pattern, after fitting the pulsar parameters). The timing residuals are generated by injecting a GW signal using Eq.(2.135) with the amplitude $A_{\rm peak} = 10^{-12}$ at the center of the observational span, MJD 55200, adding Gaussian white noise of 1 μsec. The widths of the bursts are taken as 1000 (left panel) and 4000 days (right panel), which corresponds to $A_{\rm fit} = 2.85 \times 10^{-15}$ and 1.80×10^{-15}, respectively. Timing residuals induced by a cosmic string GW burst have different shapes depending on the epoch and the width of the burst, but they are deterministic, allowing us to perform a matched filter search.

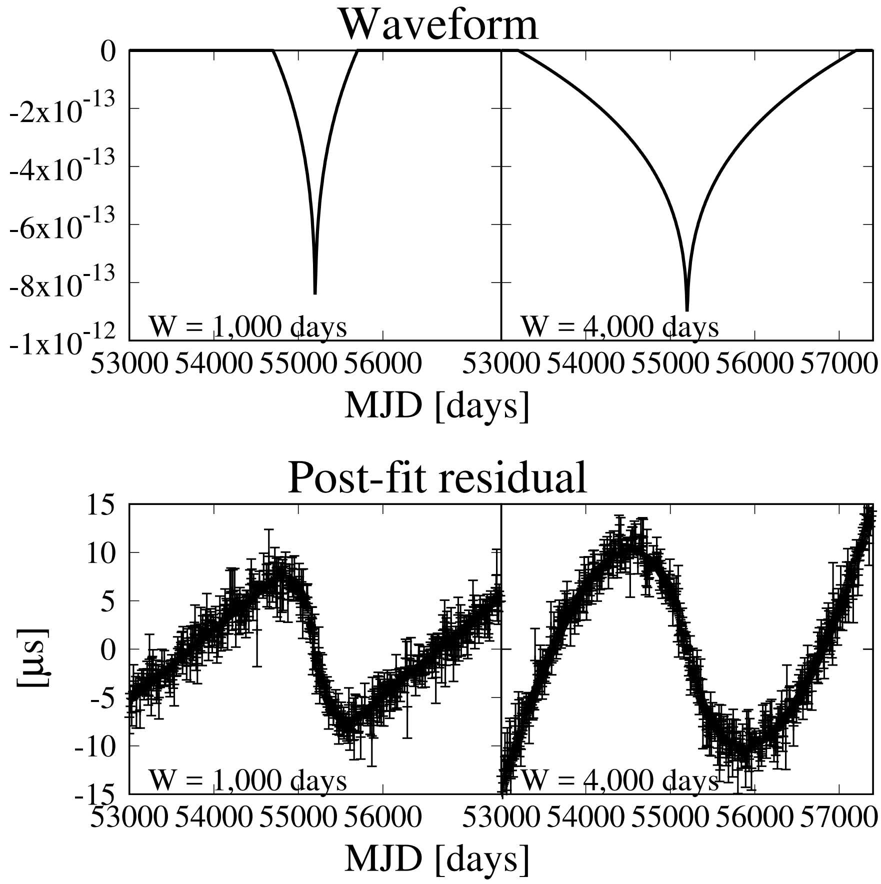

Figure 2.6: Waveforms of the GW burst from a cosmic string cusp (top panels) and post-fit timing residuals with Gaussian white noise of 1 μsec (bottom panels). Here, the GW amplitude is set to $A_{\rm peak} = 10^{-12}$ and the peak is at MJD 55200. In the bottom panel, pulsar parameters such as the pulse period and spin-down rate are fitted.

We have incorporated the effect of the GW burst from a cosmic string into the TEMPO2 timing model. This allows us to fit the GW burst from a cosmic string and to simulate residuals (or ToAs). The new timing model parameters are $(A_{\rm fit}, t_0, W, \alpha_s, \delta_s, \zeta)$. TEMPO2 uses a linear least-squares-fitting algorithm. If the burst epoch, width, polarization angle and source position are known, we can obtain the amplitude of the GW burst as a part of the standard TEMPO2 timing fit. However, if these parameters are not known, then a non-linear fitting routine is needed to determine the values.

We have found that this parametrization is convenient for simulating timing residuals caused by the GW burst from a cosmic string. However, in the search procedure, we found that it is useful to provide a second parametrization of the GW burst. In this parametrization, we describe the GW burst using two orthogonal components, A_1 and A_2 where $A_1 = A_{\rm fit}\cos(2\zeta)$ and $A_2 = A_{\rm fit}\sin(2\zeta)$. Here, ζ is the principal polarization angle. These A_1 and A_2 correspond to two GW polarization modes and this parametrization enables us to search for all GW polarizations. This formulation has the advantage that A_1 and A_2 enter the timing model linearly and can be fitted with linear least squares. We emphasize that, even with this parametrization, the position of the source and epoch and width of the event cannot be obtained using a linear-fitting routine. We therefore fit A_1 and A_2 for different sky locations, epochs and widths.

Users of the TEMPO2 software package can employ the following parameters in their parameter files: GWCS_A1, GWCS_A2, GWCS_POSITION, GWCS_EPOCH and GWCS_WIDTH for the cosmic string A_1, A_2, sky position, burst epoch and width, respectively. The PTASIMULATE software package to simulate PTA-style data sets can also be used to simulate cosmic string burst events as described in this paper.

2.2.2 Event rate of GW bursts from cosmic string cusps

Here we outline the calculation of event rate, which follows the method in [107] (see also [71, 72]). For string network evolution, we use the velocity-dependent one-scale model where all loops are assumed to be formed with the same size. Given that the cosmic string is extremely thin, with the diameter scale of the same order of magnitude as that of a proton and therefore much smaller than any cosmological scale, the cosmic strings are considered one-dimensional objects and studied in the zero-width, or Nambu-Goto approximation. This action is classically equivalent to Polyakov action for the bosonic superstring theory. These cosmic strings are often called Nambu-Goto strings. In our model, the string network of infinite strings is characterized by a correlation length ξ. The total length L of infinite strings in volume V is given by $L = V/\xi^2$, and the average string energy density is given by $\rho = \mu/\xi^2$. Defining $\gamma \equiv \xi/t$, the equation for energy conservation gives

$$\frac{t}{\gamma}\frac{d\gamma}{dt} = -1 + \nu + \frac{\tilde{c}pv}{2\gamma} + \nu v^2, \tag{2.136}$$

while the equations of motion for the Nambu-Goto string yields an equation for the evolution of the typical root-mean-square velocity v of infinite strings,

$$\frac{dv}{dt} = (1 - v^2)H(\frac{k(v)}{\nu\gamma} - 2v), \tag{2.137}$$

where $k(v) = \frac{2\sqrt{2}}{\pi}\frac{1-8v^6}{1+8v^6}$, $H \equiv \dot{a}/a$ is the Hubble expansion rate, and the scale factor a is parametrized as $a(t) \propto t^\nu$. The third term in the right-hand side of Eq.(2.136) represents the loss of energy from infinite strings by the production of loops. The constant parameter $\tilde{c}$ represents the efficiency of loop formation and is set to be $\tilde{c} = 0.23$. The reconnection probability p, which could be much less than 1 for cosmic superstrings, decreases the loop formation rate and reduces the value of γ for smaller p. The above sets of equations have asymptotic solutions. For $p = 1$, we obtain $\gamma_r = 0.27$ for the radiation-dominated era and $\gamma_m = 0.62$ for the matter-dominated era.

The string loops are formed by the reconnection of long strings with themselves, that oscillate relativistically and eventually lose their energy to GWs. We parametrize the initial loop size as $\alpha = l_b/t_b$, where b denotes the time of loop formation. After their birth, loops shrink by GW emission and the loop size at time t is given by

$$l(t) = \alpha t_b - \Gamma G\mu(t - t_b), \tag{2.138}$$

where Γ is a numerical constant which represents the efficiency of GW emission and we take $\Gamma = 50$. The number density of loops created at time t_b is given by

$$\frac{dn}{dt_b} = \frac{C}{\alpha p^2 t_b^4}\,, \tag{2.139}$$

where the coefficient C is typically determined by the number of infinite strings in the string network. In this paper, we take $C = 1/\gamma^2$, which gives $C_r = 1/\gamma_r^2 = 13.7$ for the radiation-dominated era and $C_m = 1/\gamma_m^2 = 2.63$ for the matter-dominated era. From Eq. (2.138), we obtain

$$t_b = \frac{l + \Gamma G\mu t}{\alpha + \Gamma G\mu}, \tag{2.140}$$

and

$$\frac{dt_b}{dl} = \frac{1}{\alpha + \Gamma G\mu}. \tag{2.141}$$

Using Eqs. (2.139) and (2.141) and taking into account the fact that the number density decreases as $\propto a^{-3}$ by the expansion of the Universe, we find the number density of loops with length between l and $l + \mathrm{d}l$ at time t is given as

$$\frac{dn}{dl}(t) = \frac{C}{\alpha p^2}\frac{1}{(\alpha + \Gamma G\mu)t_b^4}\left(\frac{a(t_b)}{a(t)}\right)^3 . \tag{2.142}$$

The rate of GWs coming towards us is obtained by multiplying the number of cusp events per time $2N_c/[(1+z)l]$. We assume that cusps happen once every oscillation period, namely $N_c = 1$. We also take into account the beaming effect $\frac{1}{4}\theta_m^2$, where $\theta_m \equiv [(1+z)fl]^{-1/3}$ is the maximum angle between the line of sight and the direction of a cusp velocity to detect a GW of frequency f. Multiplying by the volume $\frac{dV}{dz} = \frac{4\pi a(z)^2 r(z)^2}{H(z)(1+z)}$, the number of GW events between z and $z + dz$ is given by

$$\frac{dR}{dzdl} = \frac{1}{4}\theta_m(f,z,l)^2\frac{2N_c}{(1+z)l}\frac{dn}{dl}\frac{dV}{dz}\Theta(fl(1+z) - 2)\,, \tag{2.143}$$

where the Heaviside step function Θ represents a low-frequency cut-off below $f_l = 2/l$ at the emission. From Eq. (2.129), we find

$$l = \left(\frac{\tilde{h}(f)r(z)}{G\mu}(1+z)^{1/3}f^{4/3}\right)^{3/2}, \tag{2.144}$$

and

$$\frac{dl}{d\tilde{h}} = \frac{3l}{2\tilde{h}}\,. \tag{2.145}$$

Using Eqs. (2.142) and (2.145), we can rewrite Eq. (2.143) as

$$\begin{aligned}\frac{dR}{dzd\tilde{h}} &= \frac{3}{4}\theta_m(f,z,l)^2\frac{N_c}{(1+z)\tilde{h}}\frac{C}{\alpha p^2}\frac{1}{(\alpha+\Gamma G\mu)t_b^4} \\ &\quad\times\left(\frac{a(t_b)}{a(t)}\right)^3\frac{dV}{dz}\Theta(fl(1+z)-2)\,. \end{aligned} \tag{2.146}$$

2.3 Observation data set

We use the same PPTA data set as [95]. The observing systems and data processing techniques are similar to the first PPTA data release (DR1) as described in [83]. In brief, the data set includes 26 millisecond pulsars observed at intervals of 2 to 3 weeks between 2004 and 2016 using the Parkes telescope. The data set is available from the CSIRO pulsar data archive[1] at `https://doi.org/10.25919/5bc67e4b7ddf2`.

Before the GW search, we fitted the pulsar ToAs with a timing model and formed timing residuals using the standard TEMPO2 software package [52]. Typical parameters of this fit include the pulsar sky location, spin frequency and spin-down rate, dispersion measure, proper motion, parallax and (when applicable) binary orbital parameters. Additionally, constant offsets or jumps are fitted among ToAs collected with different receiver/backend systems.

The timing residuals contain unmodelled low-frequency noise, called “red noise”, which affects the estimation of the pulsar parameters and subsequently our search for the cosmic string signals. We have updated the noise modelling of the data set of [95], as follows. We use a frequentist-based method to estimate the red noise properties of the data set [25]. For each pulsar, we use the SPECTRALMODEL plugin to look for evidence of non-white noise. We assume that red noise is the stochastic process described by the power law

$$P_r(f) = P_0\left[1+(f/f_c)^2\right]^{-\frac{c}{2}}\,, \tag{2.147}$$

where P_0 is the amplitude at a corner frequency f_c and c is the power-law exponent. When such noise is detected, we obtain a self-consistent estimate of the covariance matrix for the low-frequency noise using the iterative procedure discussed by [25]. An initial estimate of the red noise spectrum is obtained and fitted with a model. The latter is used to estimate the covariance matrix of such noise. Adding the white-noise component of the variance as a diagonal matrix, we obtain the complete covariance matrix which is then used to estimate the power spectrum with a generalized least-squares fit. An improved model is fitted to this power spectrum and the process is iterated until a self-consistent solution is obtained.

Table 2.1 describes our red-noise models. In contrast to the analysis of [95], we include red-noise models for PSRs J1713+0747, J1732−5049, J1857+0943 and J2241−5236. Our red-noise model obtained by the Frequentist analysis is consistent with the Bayesian noise analysis in [95].

2.4 Detection algorithm

The timing residual of each pulsar induced by the GW burst is determined by specifying the source parameters: A_1, A_2, position, epoch and width. For a given position, epoch and width, we jointly fit

---

[1] data.csiro.au

Table 2.1: Red noise properties for the PPTA data set used in this work.

	This work			[95]		
Pulsar Name	c	$f_c(\mathrm{yr}^{-1})$	$P_0(\mathrm{yr}^{-3})$	c	$f_c(\mathrm{yr}^{-1})$	$P_0(\mathrm{yr}^{-3})$
J0437−4715	3.5	0.08	2.66×10^{-27}	3.5	0.08	2.37×10^{-27}
J0613−0200	2	0.08	4.31×10^{-26}	2.5	0.08	1.30×10^{-26}
J0711−6830	5	0.08	2.08×10^{-25}	4	0.08	3.98×10^{-26}
J1017−7156	6	1.0	7.24×10^{-28}	6	1.0	9.54×10^{-28}
J1022+1001	2	0.08	1.66×10^{-26}	2	0.08	3.04×10^{-26}
J1024−0719	6	0.08	3.03×10^{-24}	3	0.08	4.30×10^{-25}
J1045−4509	3	0.3	7.24×10^{-26}	3	0.3	7.44×10^{-27}
J1125−6014	1	0.08	6.02×10^{-27}	3	0.2	5.79×10^{-27}
J1446−4701	–	–	–	–	–	–
J1545−4550	4	0.2	1.16×10^{-26}	3	0.1	1.66×10^{-26}
J1600−3053	2	0.08	1.19×10^{-27}	2	0.08	1.05×10^{-27}
J1603−7202	2.5	0.08	3.58×10^{-26}	3	0.08	8.39×10^{-26}
J1643−1224	2	0.5	1.04×10^{-26}	1.5	0.08	3.43×10^{-26}
J1713+0747	2	0.5	6.46×10^{-29}	–	–	–
J1730−2304	1.5	0.08	4.93×10^{-27}	2	0.08	2.17×10^{-26}
J1732−5049	0.5	0.2	4.32×10^{-27}	–	–	–
J1744−1134	3	0.4	9.86×10^{-28}	6	1.0	2.55×10^{-28}
J1824−2452A	4	0.1	1.98×10^{-23}	4	0.1	1.22×10^{-23}
J1832−0836	–	–	–	–	–	–
J1857+0943	4	0.5	9.25×10^{-27}	–	–	–
J1909−3744	2.5	0.08	1.06×10^{-27}	2.5	0.7	7.54×10^{-28}
J1939+2134	4	0.08	2.42×10^{-25}	4	0.08	2.50×10^{-25}
J2124−3358	4	1.0	5.14×10^{-27}	5	1.0	5.64×10^{-27}
J2129−5721	2	0.2	4.80×10^{-27}	2	0.08	1.37×10^{-26}
J2145−0750	1.5	0.08	7.58×10^{-27}	1	0.08	5.13×10^{-27}
J2241−5236	6	0.8	1.07×10^{-28}	–	–	–

A_1 and A_2 with the pulsar parameters (spin-down, astrometry, orbital configuration, etc.) by adding the GW burst response to the TEMPO2 timing model and subsequently minimizing the whitened timing residuals. To account for the correlations in the pre-fit timing residuals caused by unmodelled red noise, we use the algorithm referred to as generalized least squares described in [25]. To determine the sky position, epoch and width, we search over a regular four-dimensional grid whose spacing we describe below.

At each position, epoch and width, TEMPO2 returns the parameter vector $\mathbf{A} = [A_1; A_2]$ and their covariance matrix, C_0. From them, we require a detection statistic which provides an optimal estimate of the amplitude of the GW burst. We then use that statistic to locate the GW burst in the grid of possible positions, epochs and widths. While this approach is not as computationally efficient as a non-linear fit, it provides an opportunity to study the statistics of the noise by examining the response over the entire four-dimensional grid.

If the pulsars are uniformly distributed in the sky and have the same ToA precision then A_1 and A_2 become orthogonal (independent) and equally sensitive. For this ideal case, $D = A_1^2 + A_2^2$ is an optimal detection statistic. However, A_1 and A_2 are correlated. To construct the optimal detection statistic, we must determine U^{-1}, which is the transformation matrix that whitens and normalizes $\mathbf{A}$, i.e. $\mathbf{A}_{\rm w} = \mathsf{U}^{-1}\mathbf{A}$. By multiplying U^{-1}, the components of $\mathbf{A}_{\rm w}$ become two uncorrelated random variables with unit variance. This reduces the problem to the one for which we know that the optimal solution is $D = A_{\rm w1}^2 + A_{\rm w2}^2$. This is analogous to the way we use the Cholesky decomposition to deal with red noise in TEMPO2 (see [25]). The solution is given by

$$D = \mathbf{A}_{\rm w}^{\rm t}\mathbf{A}_{\rm w} = \mathbf{A}^{\rm t}\mathsf{C}_0^{-1}\mathbf{A}\,, \tag{2.148}$$

where the superscript t indicates the transposed matrix. In the absence of the GW burst, D is the sum of the squares of two independent standard Gaussian random variables, and therefore it follows a χ^2 distribution with two degrees of freedom.

We adopt $D_{\rm max}$, which is the maximum D over different epochs, widths and sky positions, as our final detection statistic. Here, we carry out simulations to determine the false alarm probability of $D_{\rm max}$.

To estimate the values of D that can occur without the presence of the GW burst, we simulate 100 realizations of the data set using the measured noise models. We estimate the probabilities of D for various epochs from MJD 53500 to 57000 at intervals of 500 (8 patterns) and width of 50 and 100 days (2 patterns). Fig. 2.7 shows the probability distributions of maximum D in the sky, and we found they are less than $\sim$15.

However, there are particular epochs and widths that lead to higher detection statistics when a signal is absent. As an example, in Fig. 2.8, we show the probability distribution of the maximum detection statistic $D_{\rm max}$ in the search over the sky for the fixed width of 75/150 days and the epoch at MJD 54750/53750, respectively, obtained from 1000 realizations of the simulated data sets (the choice of these values is described in section 2.5). This figure indicates that a high detection statistic of $D_{\rm max} = 40$ can occur, by chance, with a probability of $\sim 10^{-3}$.

2.5 Results

We apply our detection algorithm to the PPTA data set to search for the GW burst from a cosmic string. For each sky position, epoch and width, we perform a global fit for A_1 and A_2 while simultaneously fitting the parameters specific to each pulsar. First, we fit the cosmic string amplitudes (A_1 and A_2) over 1034 sky positions, nine epochs (MJD 53000, 53500, 54000, 54500, 55000, 55500, 56000, 56500 and 57000) and 10 widths (20, 50, 100, 200, 500, 1000, 2000, 4000 and 8000 days). Fig. 2.9 shows the maximum detection statistics in the sky as a function of the width for nine epochs. We find that the detection statistics tends to become larger as the width gets narrower. The statistics for the epoch of MJD 53500 is given by the solid line, where we find a large $D_{\rm max}$ of 31.2 at the width of 100 days.

As $D_{\rm max}$ suggests a significant detection, we have investigated the data in detail. By checking the timing residuals of all pulsars around MJD 53500, we identified a “bump” in the timing residuals of PSR J1939+2134 as shown in Fig. 2.10. As shown in Fig. 2.11, most pulsars are located in the place where they are not sensitive to this quadrupole pattern. Thus, a $D_{\rm max}$ of 31.2 would

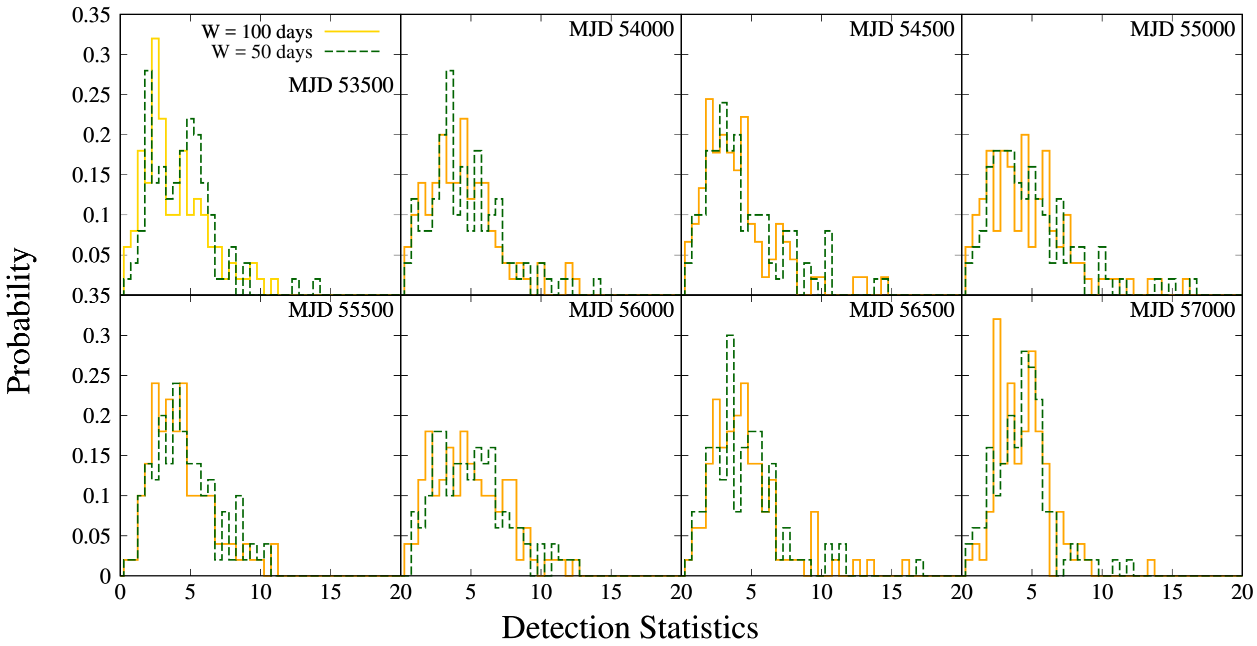

Figure 2.7: Probability distributions of maximum D in the sky obtained from 100 realizations of simulated timing residuals. The red and blue lines show the distributions for the width of 100 and 50 days, respectively. Upper panels: epoch = MJD 53500, 54000, 54500 and 55000. Lower panels: epoch = MJD 55500, 56000, 56500 and 57000.

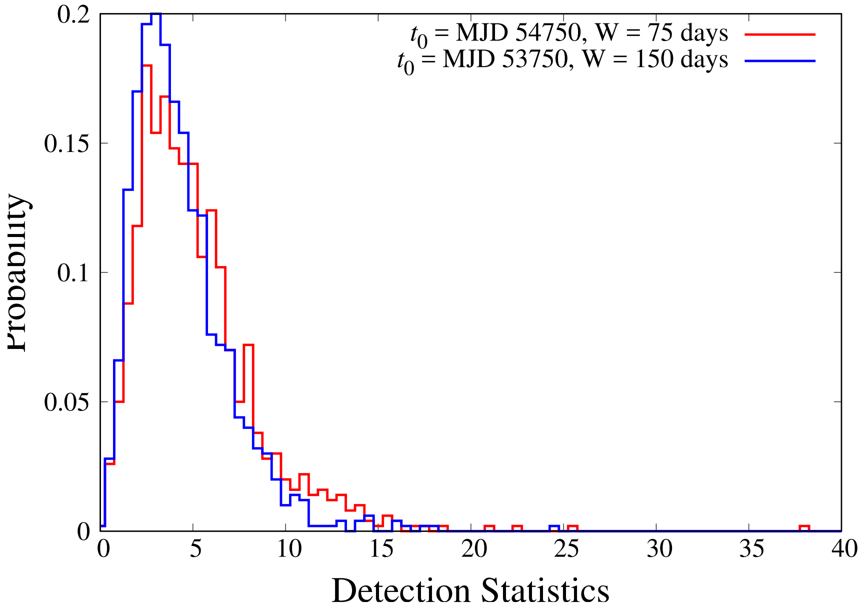

Figure 2.8: Probability distributions of maximum D in the sky obtained from 1000 realizations of simulated timing residuals. Red and blue lines represent the distributions for an epoch of 54750 and 53750, and a width of 75 and 150 days.

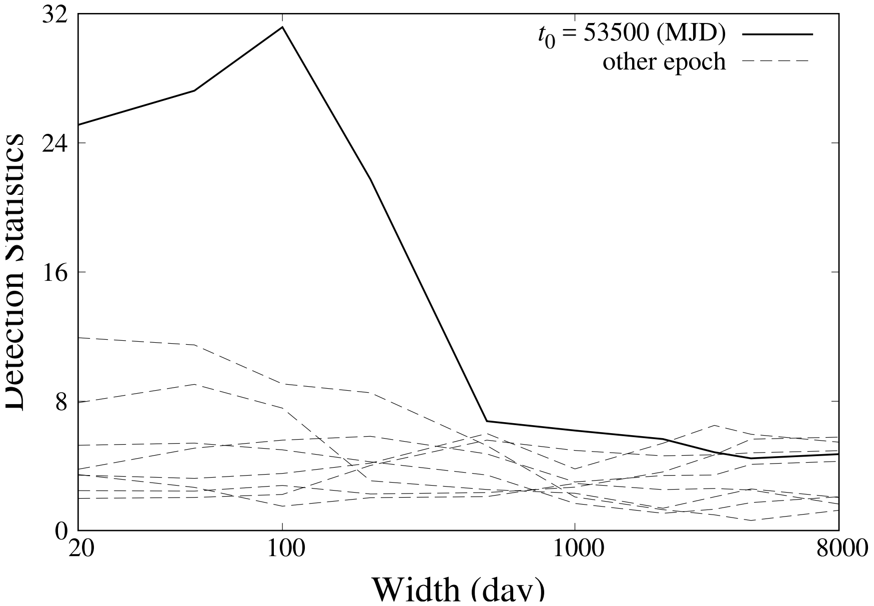

Figure 2.9: Detection statistics obtained from the PPTA data set against widths for nine epochs. Solid and dashed line show the statistics for the epoch of MJD 53500 and other eight epochs, respectively.

primarily be caused by the single feature in the residuals of PSR J1939+2134. The timing residuals for PSR J1939+2134 is known to be significantly affected by red noise and the ToA precision is high. Thus, it is challenging to get a precise red and white noise model for this pulsar. We therefore expect this to be a false detection caused by incomplete modelling of the PSR J1939+2139 residuals. Note that this quadrupolar signature implies a clear signal in the Northern-hemisphere IPTA pulsars, that are not observed by the PPTA (we consider this further in the discussion section). Hereafter, we continue our analysis by removing PSR J1939+2134 in our data set.

After we remove PSR J1939+2134 from the sample, we reprocess the data using a finer grid with 1034 sky positions, 18 epochs and 23 widths. Fig. 2.12 shows the maximum detection statistics in the sky as a function of the width. In analogy with Fig. 2.9, the detection statistics increase as the width decreases, while the maximum detection statistic is 19.8 in this case. Here, we discuss the statistical significance of the observed detection statistics. Even when there is no GW signal, we could get a large detection statistic when the number of trials m is large. The probability of getting a false-positive signal once every m trials in the absence of signals, called the family-wise error rate (FWER), is given by $1-(1-s)^m$, where s is the significance level. In our case, the number of trials m is 18 epochs $\times$ 23 widths $=414$ and the corresponding FWER is 0.9999999994 for $s=0.05$, which means that we would detect a false signal almost certainly by simply testing the significance for each detection statistic even if there were no signal. Next, we perform the Fisher's product test to combine each significance and test the global significance of a set of the observed detection statistics. In the absence of signals, the test statistic

$$F=-2\sum_i^m \ln p_i, \tag{2.149}$$

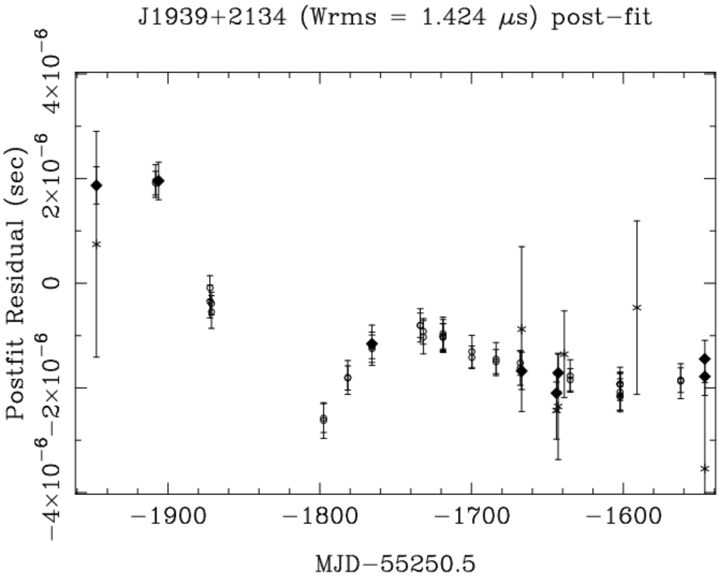

Figure 2.10: Timing residuals of PSR J1939+2134 around MJD 53500. A bump-like structure can be seen that mimics a cosmic string burst event.

follows a χ^2 distribution with $2m$ degrees of freedom under this assumption that the tests are independent, where p_i is the p-value. Although the observed detection statistics show a small correlation with respect to the width, let us here assume that the detection statistics are independent of the epoch and width, and all of their probability distributions are the same except the epochs of MJD 54750 and 53750. This would be a reasonable assumption since the simulated distributions look similar as seen in Fig. 2.7. Under the assumption, we calculate p-values for the epochs of MJD 54750 and 53750 using the simulated probability distributions, shown in Fig. 2.8, and for other epochs using the summed distribution of Fig. 2.7. We obtain $F = 751.9$ and its p-value for the χ^2 distribution is 0.97. Consequently, we conclude that there is no significant event in our data. Note that this conclusion is conservative because we utilize the probability distributions for the widths of 100 and 50 days to determine the p-values for other, longer widths.

Using the value of $D_{\rm max}$ and the covariance matrix, we can determine the sensitivity of the data set to the GW burst. For a GW burst with amplitude $h^{\rm CS,fit}$ with random polarization, the expected values are $\langle A_1^2\rangle = \langle A_2^2\rangle = (h^{\rm CS,fit})^2/2$ and $\langle A_1 A_2\rangle = 0$, and we obtain

$$\langle D\rangle = \left(h^{\rm CS,fit}\right)^2 (S_{11} + S_{22})/2, \tag{2.150}$$

where $\mathsf{S} = \mathsf{C}_0^{-1}$ and C_0^{-1} can be obtained directly from fitting the PPTA data release. Thus, the GW burst amplitude corresponding to a detection threshold $D^*_{\rm max}$ is

$$h^{\rm CS,fit} = \left(2D^*_{\rm max}/[S_{11} + S_{22}]\right)^{1/2}. \tag{2.151}$$

Here, $h^{\rm CS,fit}$ corresponds to $A_{\rm fit}$ in Eq. (2.130) when the GW is plus-polarized. As mentioned in

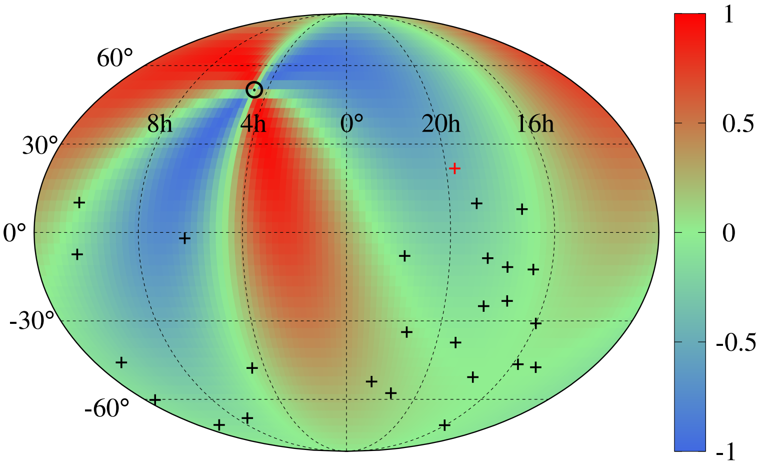

Figure 2.11: Distribution of the measured quadrupole pattern in the sky and the source position, represented as the black circle, in the equatorial coordinates. Red and black crosses indicate the position of PSR J1939+2134 and the other PPTA pulsars, respectively.

section 2.2.1, this has a dimension of $\mathrm{sec}^{-1/3}$, and the dimensionless GW amplitude is given by

$$h^{\mathrm{CS,peak}} = \left(\frac{1}{2}W\right)^{1/3} h^{\mathrm{CS,fit}}. \tag{2.152}$$

As an example, in Fig. 2.13, we show the sensitivity map for the epoch of MJD 54750 and width of 75 days. The covariance matrix is calculated at each sky position and is converted to the value of $h^{\mathrm{CS,fit}}$ using Eq. (2.151) with $D^*_{\mathrm{max}} = 19.8$. We find that the PPTA pulsar timing array is more sensitive for a GW burst in the Southern area as pulsars are concentrated in the Southern hemisphere.

The constraints on $h^{\mathrm{CS,peak}}$ can be provided as a function of the epoch, width and sky position. Since only the width has a physical meaning, which corresponds to the loop size of the cosmic string, in Fig. 2.14, we show the maximum value of $h^{\mathrm{CS,peak}}$ as a function of the width, searched over different epochs and sky positions. We find that the constraint on $h^{\mathrm{CS,peak}}$ gets stronger as W increases. The reason is that timing residuals induced by the GW burst become larger for a longer event, since a timing residual is given by the time integration of Δh.

2.6 Discussion

In this section, we discuss the physical implication of the above results. Using the theoretical estimate on the event rate given in section 2.2.2, we translate the upper limit on the GW amplitude obtained in the previous section to the constraint on the cosmic string tension. We then provide implications for observations by IPTA and SKA.

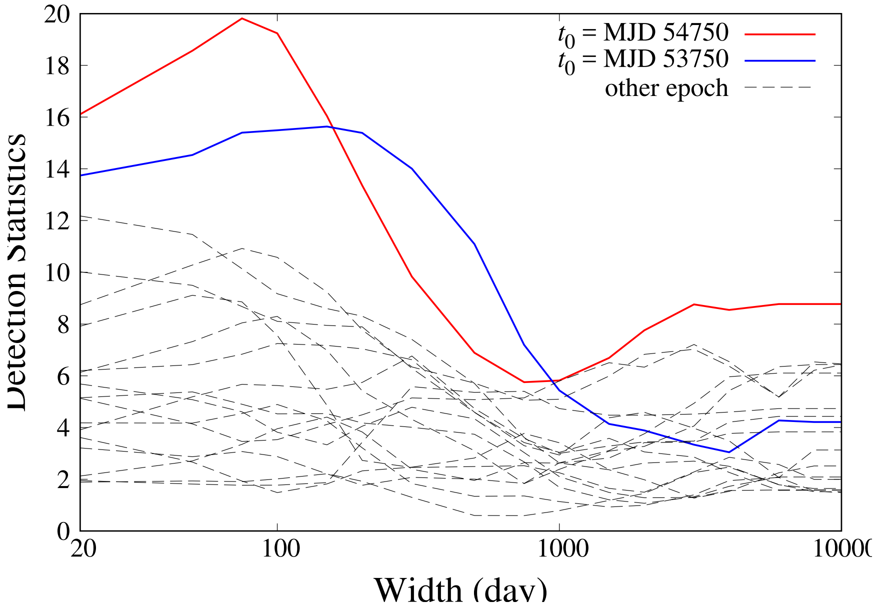

Figure 2.12: Detection statistics obtained from the PPTA data set without PSR J1939+2134 against widths for 18 epochs. Red solid, blue solid and black dashed lines show the statistics for the epochs of MJDs 54750, 53750, and other 16 epochs, respectively.

2.6.1 Constraint on the cosmic string tension

Here we translate the upper limit on the peak amplitude shown in Fig. 2.14 to the constraint on the cosmic string tension. As derived in section 2.2.2, the event rate of GW bursts from cosmic string cusps emitted in the redshift between z and $z + dz$ whose Fourier amplitude is between $\tilde{h}$ and $\tilde{h} + d\tilde{h}$ can be written using various parameters as

$$\begin{aligned} \frac{dR}{dz d\tilde{h}} &= \frac{3}{4}\theta_m(f,z,l)^2 \frac{N_c}{(1+z)\tilde{h}} \frac{C}{\alpha p^2} \frac{1}{(\alpha + \Gamma G\mu) t_b^4} \\ &\times \left(\frac{a(t_b)}{a(t)}\right)^3 \frac{dV}{dz} \Theta(fl(1+z) - 2)\,, \end{aligned} \tag{2.153}$$

where $\theta_m(f,z,l) \equiv [(1+z)fl]^{-1/3}$, N_c is the number of cusps per oscillation period of the string loop $T_l = l/2$, C is the parameter characterizing the number of string loops, α characterises the loop size at formation, p is the probability of recconection when two strings intersect, Γ represents the efficiency of GW emission from the loop, t_b is the time when the loop is formed and given by $t_b = \frac{l + \Gamma G\mu t}{\alpha + \Gamma G\mu}$. In the following analysis, we use the values commonly used in the literature, $N_c = 1$, $p = 1$, $C_r = 13.7$ (C for the radiation-dominated era), $C_m = 2.63$ (C for the matter-dominated era), and $\Gamma = 50$. Recent simulations suggest the large initial loop size of $\alpha \sim 0.1$, while it could be much smaller $\alpha \sim \Gamma G\mu$ if the gravitational backreaction accounts the loop formation. Thus, we investigate the constraints on tension for different values of α. In the second line, $a(t)$ or $a(z) = [1+z]^{-1}$ is the scale factor of the expanding Universe and the volume of the Universe is given as $\frac{dV}{dz} = \frac{4\pi a(z)^2 r(z)^2}{H(z)(1+z)}$, where $H(z)$ is the Hubble expansion rate and given by $H(z) = H_0\sqrt{\Omega_r(1+z)^4 + \Omega_m(1+z)^3 + \Omega_\Lambda}$

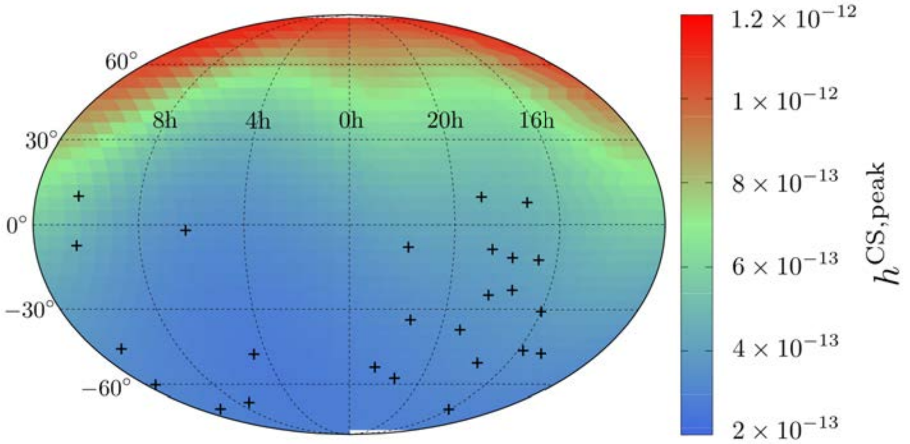

Figure 2.13: Sensitivity of the PPTA data set for $h^{\mathrm{CS,peak}}$ for the epoch of 54750 and width of 75 days. Black crosses represent the positions of the pulsars without PSR J1939+2134.

with $H_0 = 100h$ km/s/Mpc. They can be calculated once we set the cosmological parameters and we use $h = 0.678$, $\Omega_m = 0.308$, $\Omega_r h^2 = 4.15 \times 10^{-5}$, and $\Omega_\Lambda = 1 - \Omega_m$ [94]. The Heaviside step function Θ represents a low-frequency cut-off below $f_l = (l/2)^{-1}$ at the emission.

Then the number of GWs coming to the Earth today above the strain amplitude $\tilde{h}_{\mathrm{lim}}$ is given by

$$N_{\mathrm{GW}} = T_{\mathrm{obs}} \int_{\tilde{h}_{\mathrm{lim}}}^{\infty} d\tilde{h} \int_0^{\infty} dz \frac{dR}{dz d\tilde{h}}, \tag{2.154}$$

where we take the observation time to be $T_{\mathrm{obs}} = 12$ years. Considering no detection of cosmic string GW bursts with amplitude above $\tilde{h}_{\mathrm{lim}}$, the parameter space giving $N_{\mathrm{GW}} > 2.996$ is excluded at the 95% level for a random Poisson process. We have provided upper bounds on the time-domain peak amplitude $h^{\mathrm{CS,peak}}$ for different width W in Fig. 2.14. This can be translated to the Fourier strain amplitude $\tilde{h}_{\mathrm{lim}}$, using Eq. (2.134), as

$$\tilde{h}_{\mathrm{lim}}(f_l) \sim \frac{h^{\mathrm{CS,peak}}(W = 2f_l^{-1})}{\beta\sqrt{\frac{3}{2\pi}}\Gamma(-\frac{1}{3})f_l}\,, \tag{2.155}$$

where we have added the suppression factor $\beta = 0.81$ in order to take into account the effect of the high-frequency cut-off. In the following, we place an upper limit on the cosmic string tension $G\mu$ using Eqs.(2.154) and (2.155).

Fig. 2.15 shows the constraint on the string tension $G\mu$ for different initial loop sizes α, obtained using $h^{\mathrm{CS,peak}}$ for different widths W. We see that the constraint improves for larger W for the following two reasons. First, the bound on $h^{\mathrm{CS,peak}}$ is more constraining for larger W, as shown in Fig. 2.6. Second, loops with larger size have a larger GW amplitude and a smaller number density. The former makes detection easier and the latter makes it more difficult. Taking into account both effects, we find that the former effect dominates and larger loops, namely larger W, are easier to

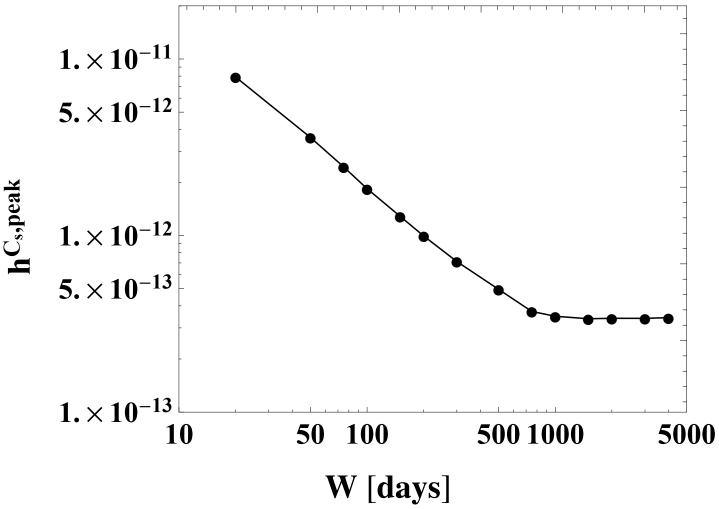

Figure 2.14: Constraint on the GW amplitude as a function of the width W. The maximum value of $h^{\mathrm{CS,peak}}$ is searched over epochs and sky positions by fixing the width.

detect and give better constraints. We also see that the constraint is stronger for smaller initial loop sizes. As the lifetime of the loop is given by $\frac{\alpha t_b}{\Gamma G\mu}$ and is shorter when α is smaller, GWs are associated with loops coming from the matter-dominated era, for small α, while for large α, the loops live longer and are generated earlier in the radiation-dominated era. Due to the difference in the expansion rate, we have a larger number of loops for those generated in the matter-dominated era, which makes the constraint stronger.

The parameters such as N_c, C, and p^2 in Eq. (2.153) change the overall number of GW bursts and affect the upper bound. The number of cusps per oscillation period N_c is typically considered to be of order 1. The coefficient in the loop number density C is determined by the number of long strings inside the horizon and by the efficiency of energy loss to loops. This value can vary in the range $\mathcal{O}(1-10)$. For example, we use $C_r = 13.7$ and $C_m = 2.63$, while the LIGO paper [5] uses $C_r = 1.6$ and $C_m = 0.48$ (for Model 1). Lastly, the reconnection probability p can vary a lot, as it may get suppressed up to $\mathcal{O}(10^{-3})$ in the case of superstrings [56], while field theoretic strings have $p \sim 1$. In order to see how the constraints are affected by those factors, we define the combination of the parameters as[2]

$$C' = \left(\frac{N_c}{1}\right)\left(\frac{C_r}{13.7}\right)\left(\frac{1}{p^2}\right) \quad \text{or} \quad \left(\frac{N_c}{1}\right)\left(\frac{C_m}{2.63}\right)\left(\frac{1}{p^2}\right) \tag{2.156}$$

and, in Fig. 2.16, we show how the upper bound on $G\mu$ changes when C' has different values by fixing $W = 4000$ days, which gives the strongest constraint in Fig. 2.15. We find that the upper bound on $G\mu$ gets better for larger C' as it becomes easier to detect GWs when the number density increases. The jump in the curve, most prominent for $\alpha = 10^{-1}$, corresponds to whether the loops are produced in the radiation or matter era.

---

[2] Here, we assume that C_r and C_m are changed by the same factor.

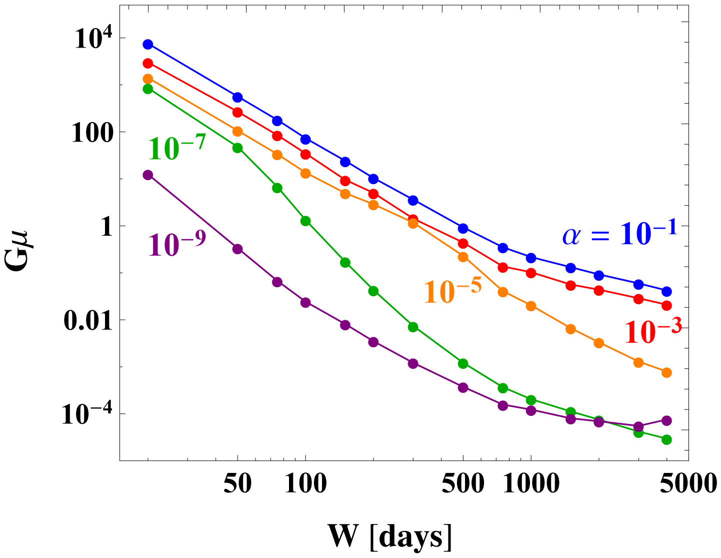

Figure 2.15: Constraint on $G\mu$ obtained for different widths W. We show the cases for different initial loop sizes $\alpha = 10^{-1}, 10^{-3}, 10^{-5}, 10^{-7}, 10^{-9}$. Here we assume $p = 1$.

Finally, in Fig. 2.17, we present the constraint in the $G\mu - \alpha$ plane, compared with constraints by other types of observations; cosmic microwave background (CMB) [93] and a stochastic GWB[3]. Although the stochastic background provides better constraint on the string parameters, we stress that the burst GW search provides independent constraints.

2.6.2 Prediction for the IPTA data set

As mentioned in section 2.5, we find a large detection statistic $D = 31.2$ for $W = 75$ days at MJD 53500. If it is caused by the GW burst, the effect should appear in the timing residuals for pulsars in the Northern hemisphere. Here we provide a prediction for the IPTA pulsars. Table 2.2 shows the expected effect of the GW burst, which yields $D = 31.2$ with $W = 75$ days at MJD 53500, in IPTA pulsars that are not observed by the PPTA but are observed by the NANOGrav and EPTA. The second and third columns in the table represent the values of the antenna pattern function and the weighted RMS of the residuals (obtained from [75]), respectively. The fourth column is the antenna pattern normalized by σ_{w}, which describes how strong the GW signal can be seen against the timing noise. We find that the strongest effect of the GW burst should appear in PSR J1012+5307. In order to verify whether $D = 31.2$ is a GW signal or not, IPTA data, especially PSR J1012+5307, will be valuable to study.

---

[3] We derived the shaded area using the upper limit on the stochastic GWB for different spectral index given in [11]; $A_{\mathrm{GWB}} = 1.45 \times 10^{-15}$ for $\gamma = 13/3$ and it scales as $\propto 10^{-0.4\gamma}$, where the characteristic strain amplitude is parametrized as $h_c(f) = A_{\mathrm{GWB}} \left(\frac{f}{\mathrm{yr}^{-1}}\right)^{\alpha}$ and $\gamma = 3 - 2\alpha$.

Table 2.2: Expected sensitivities of IPTA pulsars for the GW burst causing $D = 31.2$. The second and third columns represent the values of the antenna pattern function and the weighted RMS of the residuals [75]. The forth column is the antenna pattern normalized by σ_{w}, which describes the relative sensitivity to the GW signal.

Pulsar Name	$\sum_A F^A(\hat{\Omega}, \hat{p})$	σ_{w} (μs)	Sensitivity ($\mu\mathrm{s}^{-1}$)
J0030+0451	0.38	1.5	0.25
J0034−0534	0.46	4.4	0.10
J0218+4232	0.06	6.7	0.01
J0610−2100	−0.41	5.2	−0.08
J0621+1002	−0.80	7.2	−0.11
J0751+1807	−0.62	3.3	−0.19
J0900−3144	−0.41	2.8	−0.15
J1012+5307	0.79	1.6	0.49
J1455−3330	0.04	3.8	0.01
J1640+2224	0.02	2.0	0.01
J1721−2457	−0.03	25.7	0.00
J1738+0333	−0.11	2.6	−0.04
J1751−2857	−0.05	2.4	−0.02
J1801−1417	−0.10	2.0	−0.05
J1802−2124	−0.08	2.9	−0.03
J1804−2717	−0.06	4.4	−0.01
J1843−1113	−0.15	1.0	−0.15
J1853+1303	−0.30	1.1	−0.27
J1910+1256	−0.32	1.4	−0.23
J1911+1347	−0.33	5.2	−0.06
J1911−1114	−0.17	0.7	−0.25
J1918−0642	−0.21	1.5	−0.14
J1955+2908	−0.49	5.0	−0.10
J2010−1323	−0.16	2.0	−0.08
J2019+2425	−0.49	8.8	−0.06
J2033+1734	−0.44	13.3	−0.03
J2229+2643	−0.45	3.8	−0.12
J2317+1439	−0.10	1.0	−0.10
J2322+2057	−0.19	7.0	−0.03

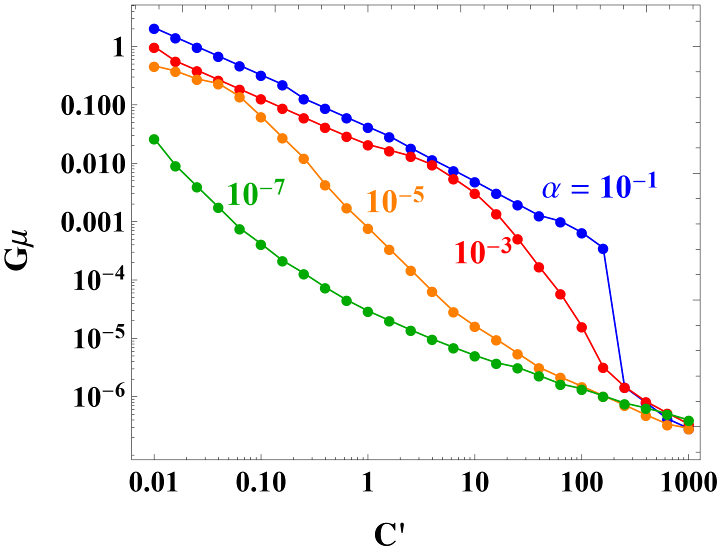

Figure 2.16: Dependence of the upper bound of $G\mu$ on the coefficient of loop number density C' for $W = 4000$ days.

2.6.3 Implications for the SKA

In Fig. 2.17, we also show the prediction for the SKA, plotted assuming that the SKA can reach $h^{\mathrm{CS,peak}} = 10^{-16}$. We see that we can improve the constraint dramatically up to $G\mu \sim 10^{-10}$ with the SKA (dashed light-blue line) and, if string loops are clustered in the dark-matter halo of our galaxy [24], we may even be able to reach down to $G\mu \sim 10^{-12}$ for large α (dotted dark-blue line). Usually, stochastic background searches provide better constraints on the string parameters at the PTA frequency. However, if the string tension is low, $10^{-15} < G\mu < 10^{-8}$, the loop lives longer and the old loops tend to cluster, enhancing the local number density of loops up to $\sim 10^5$. Thus, we can access the parameter space of small $G\mu$ with the improved sensitivity of the SKA, which may enhance the possibility of single burst detection. A tight bound on the string tension by the SKA would be extremely useful to test models of cosmic superstrings such as the KKLMMT scenario, where the tension is predicted to be in the range $10^{-12} < G\mu < 10^{-6}$ [60, 100, 61].

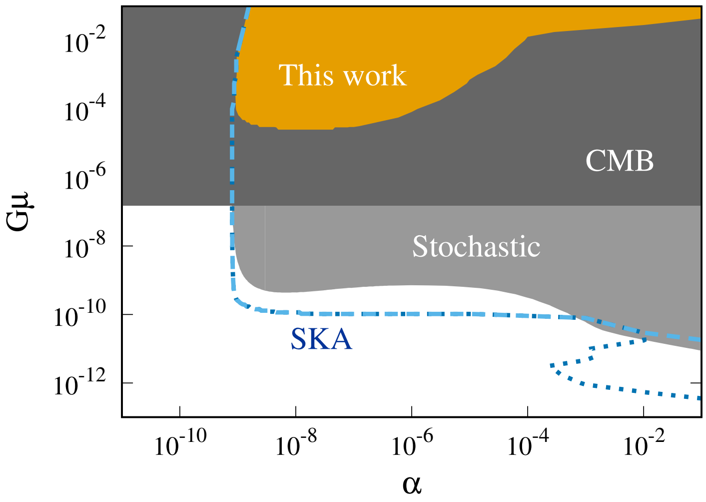

Figure 2.17: Constraint in the $G\mu - \alpha$ plane obtained by this work (orange) compared with a stochastic background search by PTA (light gray) and the CMB (dark gray). The dashed line (light blue) is the accessible parameter space predicted for the SKA. The dotted line (dark blue) is also prediction for the SKA with the clustering of cosmic string loops in our galaxy's halo.

Chapter 3

New detection method for ultra-low-frequency gravitational waves with pulsar spin-down rate statistics

3.1 Final parsec problem

In the PTA frequency range, GW sources are considered to be mainly inspiraling SMBH binaries and their incoherent superposition, the GWB. This frequency range of $10^{-9} - 10^{-7}$ Hz corresponds to the sub-pc orbital radii (e.g., 6.31×10^{-3} pc for an equal-mass of $10^{8} M_{\odot}$ binary at 10^{-8} Hz), so that only the binaries in the late stage of the evolution can be probed with PTAs. In the early stage of the evolution, the orbit of a SMBH binary shrinks as the angular momentum is extracted by scattering of stars and the friction of surrounding gas. However, when the orbital radius becomes a few pc, the transfer of angular momentum by stars and gas is no longer effective so that it exceeds the Hubble time for two SMBHs to merge by only GW emission [78, 84]. This is called "the final parsec problem" and, therefore, it is important to observe pc-scale binaries in the earlier stage. M87 is one of candidates for host galaxies which have SMBH binaries with large orbits [14]. However, GWs from the binary in M87 have too low frequency to be detected with PTAs.

In [115], then, we proposed a new detection method for a single GW with a ultra-low frequency ($\lesssim 10^{-9}$ Hz). In a observational time span of order 10 years, the amplitude of ultra-low frequency GWs does not appear like a wave but evolve linearly as a function of time. Such GWs are absorbed by the pulsar spin-down rate in the pulsar parameter fitting since both have the same time dependences on the arrival time of pulses, so that such GWs are undetectable by the conventional PTA. However, the bias on the spin-down rate induced by ultra-low frequency GWs depends on the relative direction of the pulsar and GW source in the sky and, fixing the direction of the GW source, the bias shows a quadrupole pattern in the sky. The basic idea of the method is to divide the pulsars according to the position in the sky and see the difference in the statistics of the spin-down rates. Because the quadrupole pattern in the sky is critical for the method, it cannot be applied to the detection of stochastic GW background directly.

In this chapter, we estimate the expected sensitivity of our method quantitatively by simulating the spin-down rate statistics of millisecond pulsars considering future pulsar surveys by the SKA.

Assuming the position of a GW source and the polarization angle of the GWs, pulsars are divided into two groups according to their position in the sky. If the GW is strong enough, the difference in the spin-down rate distribution of the two groups exceeds the statistical fluctuation. This is the signal of a ultra-low frequency GW.

3.2 Detection principle

Let us consider the case that the period of GWs is much longer than the observational time span (about 10 years) and, the GW amplitude changes linearly with time. In this work, we neglect the second term ("pulsar term") assuming it has a random phase relative to the first term ("Earth term") for different pulsars and behaves as a random noise with zero mean so that the effect of pulsar term reduces for a large number of pulsars. As we discuss further in section 3.4, this treatment is valid for GW frequency of $\gtrsim 10^{-13}$ Hz. Then, we can write Eq. (2.48) as

$$\Delta h_A(t, \hat{\Omega}, \theta) = \dot{h}_A(\hat{\Omega}, \theta) t. \tag{3.1}$$

Substituting Eq. (2.48) into Eq. (2.44), the timing residual induced by linearly-changing GWs becomes

$$r_{\mathrm{GW}}(t) = \frac{1}{2} \sum_{A=+,\times} F^A(\hat{\Omega}, \hat{p}) \dot{h}_A(\hat{\Omega}, \theta) t^2. \tag{3.2}$$

However, such a timing residual is absorbed in the linear-fitting for the timing model of the evolution of the pulse phase in the form of a polynomial of time. Thus, even if such GWs exist, they just contribute to the correction of the quadratic part of the series. Consequently, $\dot{p}/p$ after the polynomial-fitting becomes

$$\frac{\dot{p}}{p} = \frac{\dot{p}_0}{p} + \alpha(\hat{\Omega}, \hat{p}, \theta), \tag{3.3}$$

where p is the pulse period, $\dot{p}$ and $\dot{p}_0$ are the observed and intrinsic spin-down rates respectively, and $\alpha(\hat{\Omega}, \hat{p}, \theta)$ is a bias factor due to ultra-low frequency GWs which is given by

$$\alpha(\hat{\Omega}, \hat{p}, \theta) = \sum_{A=+,\times} F^A(\hat{\Omega}, \hat{p}) \dot{h}_A(\hat{\Omega}, \theta). \tag{3.4}$$

In principle, we cannot separate the GW effect from the intrinsic $\dot{p}_0/p$ for a single pulsar. Therefore, such low-frequency GWs cannot be detected by the conventional PTA method.

However, it should be noted that the value of the bias factor, $\alpha(\hat{\Omega}, \hat{p}, \theta)$, depends on the source position, the GW polarization angle and the pulsar position, and can be either positive or negative. In fact, the distribution of $\alpha(\hat{\Omega}, \hat{p}, \theta)$ is a quadrupole pattern, as seen in Fig. 3.1. If we divide pulsar samples into two groups according to the sign of the bias factor at the pulsar position, GWs will induce a systematic difference in the spin-down rate distribution of the two groups. Thus, even though the GW signal cannot be extracted from individual pulsars, it will be possible if we utilize the statistics of spin-down rates. However, we note that this method is possible only for a single GW source. In case of multiple sources with comparable $\dot{h}$ values or GWB, the pattern of $\alpha(\hat{\Omega}, \hat{p}, \theta)$ in the sky is much more complicated and the detection of such GWs would be very hard. Hereafter, we consider only a case of a single source.

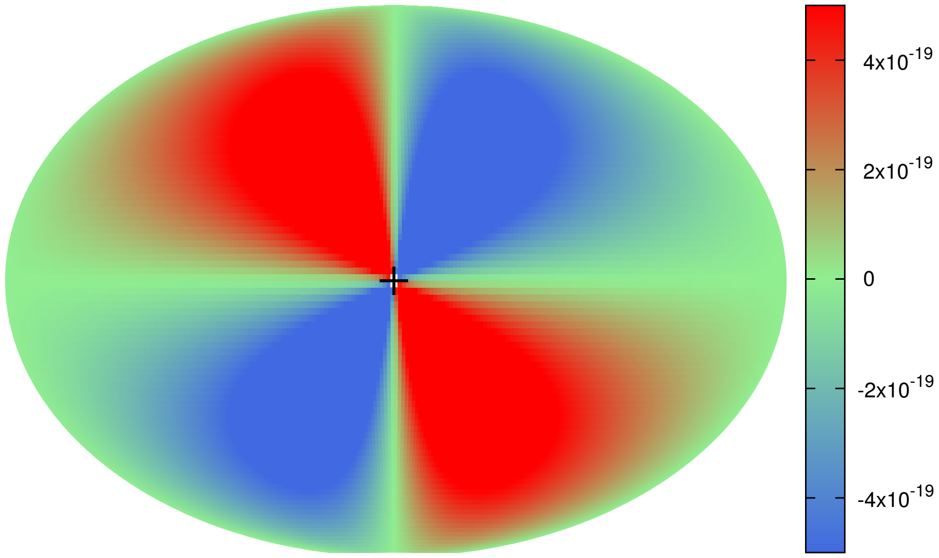

Figure 3.1: Bias factor $\alpha(\hat{\Omega}, \hat{p})$ in the sky for $\dot{h}_+ = 0$ s^{-1} and $\dot{h}_\times = 10^{-18}$ s^{-1}. The symbol "+" in the figure represents the source position.

Fig. 3.2 shows the histogram of $\log_{10} \dot{p}/p$ [sec^{-1}] of 148 observed MSPs with $p < 30$ ms. Here, MSPs in globular clusters are excluded since they would have been biased significantly by the gravitational potential and complicated dynamics inside the cluster. Further, one MSP with a negative spin-down rate ($\dot{p}/p = -10^{-21.2}$ [sec^{-1}]) is not included. Also, one MSP with an extremely large spin-down rate ($\dot{p}/p = 10^{-11.5}$ [sec^{-1}]) is excluded as an outlier. We can see that the value of $\log_{10} \dot{p}/p$ [sec^{-1}] ranges from -18.5 to -16 for "normal" MSPs. Here, we note that the observed spin-down rates are biased by various factors other than GWs: the Shklovskii effect [106], acceleration along the line of sight by gravity inside a globular cluster [92] and the Galactic differential rotation [32, 97], acceleration toward the Galactic disk [89] and low-frequency components of "pulsar timing noise" (or "red noise") often approximated as a power law of the form $S(f) \propto f^{-\lambda}$, where $\lambda \geq 1$ is the noise index [66, 67]. Although the biases from the Galactic differential rotation and acceleration toward the disk could have spatial correlations in the sky, these effects are less significant ($\Delta(\dot{p}/p) \lesssim 10^{-19}$ for MSPs at ≤ 10 kpc) [89] and will be removed if the distance to MSPs is measured precisely in the future. We also note that red noise could have a spatial correlation in the case the noise originates in a spatially correlated process such as errors in solar-systems ephemerides [21], or possibly low-frequency components of a GWB [104]. The effects of these biases will be studied elsewhere in the future.

Fig. 3.3 shows a schematic view of the expected systematic difference in the distribution of spin-down rates of two groups mentioned above. In this figure, GWs with $\dot{h} = 10^{-18}$ s^{-1} is assumed and

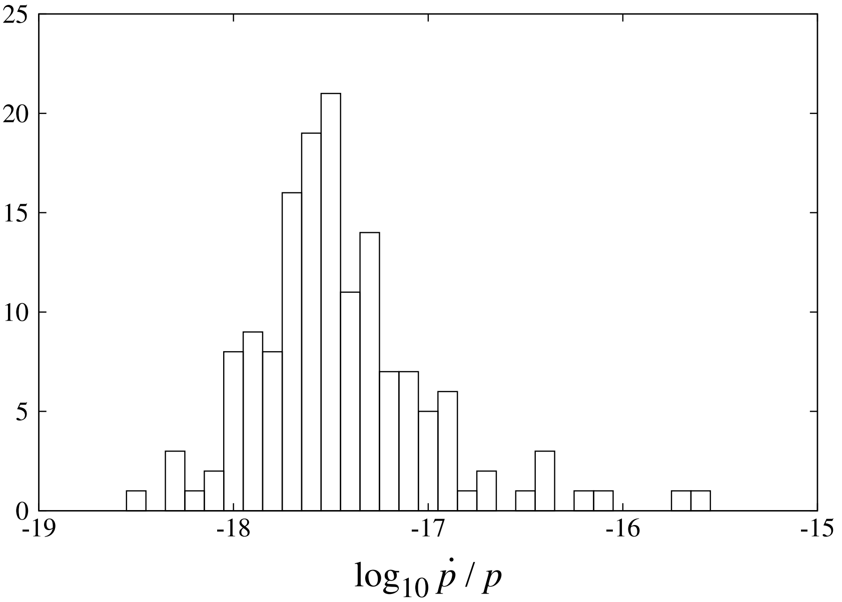

Figure 3.2: Histogram of $\log_{10} \dot{p}/p$ [sec^{-1}] of 149 observed pulsars with $p < 30$ ms. Here pulsars in globular clusters and two ones with negative and extremely large spin-down rates ($\dot{p}/p = -10^{-21.2}$, $10^{-11.5}$ [sec^{-1}]) are not included.

thus pulsars with an intrinsic spin-down rate of this order or smaller ($\dot{p}_0/p \lesssim 10^{-18}$ s^{-1}) are significantly affected while those with a much larger value of $\dot{p}_0/p$ are not affected. Overall, the presence of GWs are reflected in the extension of the left-hand-side tail of the observed $\dot{p}/p$ distribution: a short (long) tail for the positive (negative) $\alpha(\hat{\Omega}, \hat{p}, \theta)$ group. In this paper, we characterize this feature with the skewness of the $\log_{10} \dot{p}/p$ distribution and consider the difference in the skewnesses of the two regions as a statistical measure which reflects the value of $\dot{h}$.

3.3 Simulation results

In this section, we show results of a series of simulations to evaluate the sensitivity for ultra-low frequency GWs from a single source. The precision of the determination of the source position and GW polarization angle is also investigated.

First, in our simulations, a number of MSPs are located randomly in the sky with an isotropic probability distribution. However, it should be noted that the MSP distribution will not be isotropic but concentrated on the Galactic plane, because the overwhelming majority of the observed MSPs are expected to be Galactic. This means that the sensitivity of the method will be depended on the GW source position. Then the spin-down rate $\log_{10} \dot{p}/p$ is given to each of the MSPs according to a Gaussian probability distribution function with the mean and variance of -17.5 and 0.21, respectively, which are taken from the known MSP samples (Fig. 3.2). Given the direction and polarization angle of assumed GWs, the observed spin-down rates are biased by a factor of $\alpha(\hat{\Omega}, \hat{p}, \theta)$ depending on the MSP position. After application of the bias factor, we examine the biased spin-down rates and

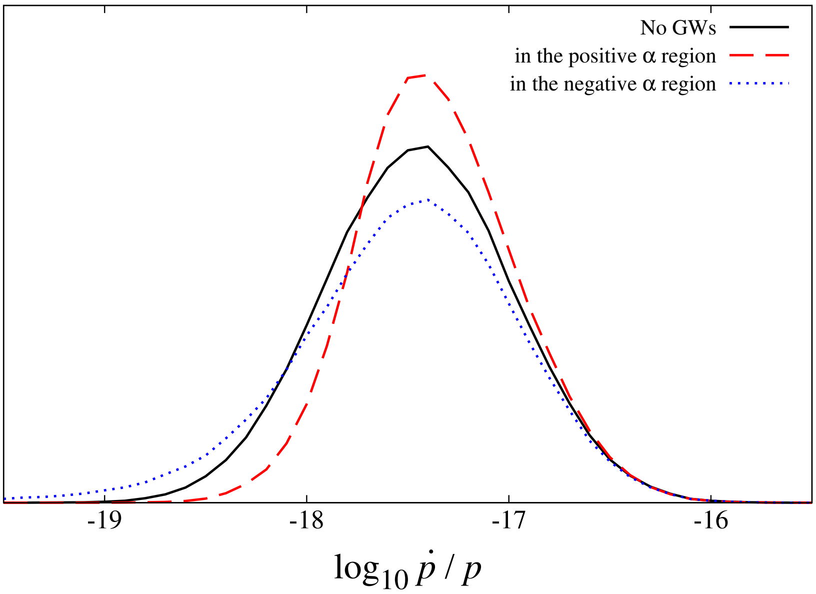

Figure 3.3: Schematic view of the expected systematic difference in the distribution of spin-down rates ($\dot{p}/p$) of two groups in the presence of ultra-low frequency GWs with $\dot{h} = 10^{-18}$ s^{-1}. The black line is the assumed intrinsic distribution, which is Gaussian with the mean value and variance which are the same values as the observed ones (Fig. 3.2). The dashed (red) and dotted (blue) lines show the expected observable distributions in the positive and negative $\alpha(\hat{\Omega}, \hat{p})$ regions (the red and blue regions in Fig. 3.1), respectively.

remove any MSPs with negative $\dot{p}$ from the rest of the analysis. In each realization, we create the mock MSP catalogs according to the method described above, and then we perform GW search based on the idea described in the previous section as follows.

Assuming the position and polarization angle of GWs, the sky is divided into two regions according to the sign of $\alpha(\hat{\Omega}, \hat{p}, \theta)$. Then a histogram of observed values of $\log_{10} \dot{p}/p$ is obtained for each region and the difference of skewness between the two histograms is computed, which is defined as

$$\Delta S = S_{\alpha+} - S_{\alpha-}, \tag{3.5}$$

where $S_{\alpha+}$ and $S_{\alpha-}$ represent the skewness of the $\log_{10} \dot{p}/p$ distributions in the positive and negative $\alpha(\hat{\Omega}, \hat{p}, \theta)$ regions, respectively. The skewness is given by

$$S_{\alpha+(-)} = \frac{1}{\sigma^3_{+(-)} N_{+(-)}} \sum_{i}^{N_{+(-)}} \left(\log_{10} \left(\frac{\dot{p}}{p} \right)_i - \mu_{+(-)} \right)^3, \tag{3.6}$$

where $i = 1, \cdots, N_{+(-)}$ is the number of MSP in the positive (negative) $\alpha(\hat{\Omega}, \hat{p}, \theta)$ region, and $\mu_{+(-)}$

and $\sigma^2_{+(-)}$ are the mean value and variance of the $\log_{10}\dot{p}/p$ distribution in each region, respectively,

$$\mu_{+(-)} = \frac{1}{N_{+(-)}}\sum_{i}^{N_{+(-)}}\log_{10}\left(\frac{\dot{p}}{p}\right)_i , \tag{3.7}$$

$$\sigma^2_{+(-)} = \frac{1}{N_{+(-)}}\sum_{i}^{N_{+(-)}}\left(\log_{10}\left(\frac{\dot{p}}{p}\right)_i - \mu_{+(-)}\right)^2 . \tag{3.8}$$

If we choose correct source position and GW polarization angle, we would obtain nonzero value of ΔS. We obtain a probability distribution of the skewness difference ΔS for a fixed $\dot{h}$ value from 10,000 realizations. It should be noted that the simulation results are independent of the type of GW sources, if GWs come from a single source. Also, because MSPs are distributed isotropically, our result does not depend on the source position and GW polarization angle.

Let us begin with the results of our fiducial simulations with 3,000 MSPs. This number of MSPs is expected by a future pulsar survey with SKA2 [62]. Considering a situation where we have specific targets such as Sgr A* and M87, we set the GW source position to the correct values. In addition, the GW polarization angle is also set to the correct value. This is not practical and we discuss this later in this section. Then the bias factor $\alpha(\hat{\Omega}, \hat{p}, \theta)$ is fixed and mock MSPs are divided into two groups. Fig. 3.4 shows the probability distribution of the skewness difference. A large $\dot{h}$ value leads to a large skewness difference and the average values are 0.20, 0.54 and 0.84 for $\dot{h} = 10^{-19}$, 3×10^{-19} and 10^{-18}, respectively, while the standard deviations are 0.11, 0.14 and 0.16, respectively. On the other hand, in the absence of GWs, the average value of skewness difference is zero and the standard deviation is 8.2×10^{-2}. A hypothesis of no GWs is rejected for the skewness difference larger than 0.17 at 98% confidence. Thus, GWs of $\dot{h} \gtrsim 3 \times 10^{-19}$ would be detected with 3,000 MSPs in the absence of other noise contributions.

Figs. 3.5 and 3.6 show the probability distributions of the skewness difference for 1,000 and 10,000 MSPs, respectively. The number of MSPs is expected to reach 1,000 by an SKA1 survey. Although 10,000 MSPs are not realistic even with the SKA2, we consider this case in order to investigate the ultimate capability of this method. As the number of MSPs increases (decreases), the standard deviation of the probability distribution decreases (increases) and the sensitivity for GWs is estimated to be about $\dot{h} \sim 10^{-18}$ with 1,000 MSPs and $\dot{h} \sim 10^{-19}$ with 10,000 MSPs. Thus, the sensitivity improves almost proportionally to the number of MSPs.

3.3.1 Effect of the intrinsic skewness of the spin-down rate distribution

In the above analyses, we assumed the intrinsic $\log_{10}\dot{p}_0/p$ distribution is Gaussian. However, as we show below, the $\log_{10}\dot{p}_0/p$ distribution of known MSPs is not Gaussian. To test the Gaussian, we use the Jarque-Bera test. The test statistic JB is defined as

$$JB = \frac{N}{6}\left[S^2 + \frac{1}{4}(K-3)^2\right], \tag{3.9}$$

where K is the sample kurtosis and N is the number of samples. If the sample distribution is Gaussian, this test statistic follows the χ^2 distribution with 2 degrees of freedom, and the critical value for 99.5% confidence is 10.6. From the known MSP samples in Fig. 3.2, we obtain $S = 1.2$ and

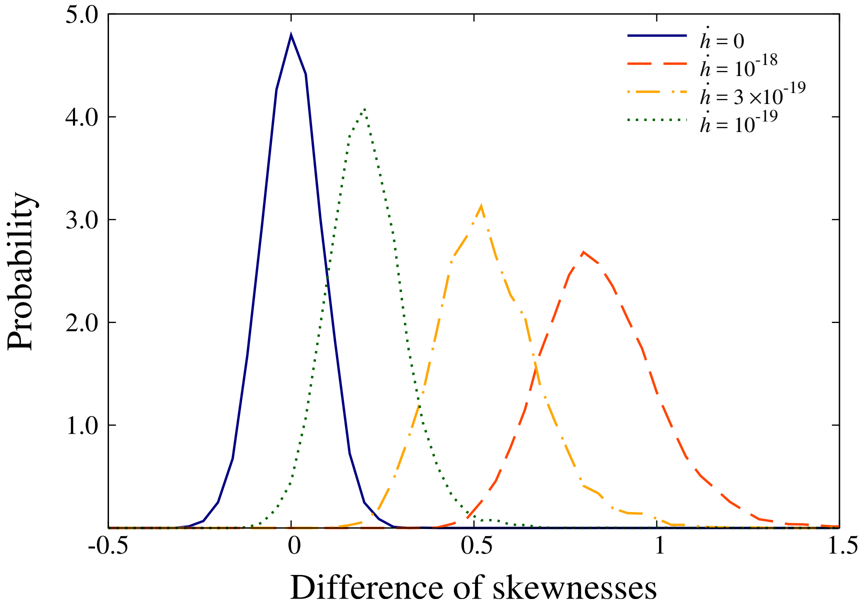

Figure 3.4: Probability distribution of the skewness difference of the $\log_{10}\dot{p}/p$ distributions between the positive and negative $\alpha(\hat{\Omega},\hat{p})$ groups in the case of 3,000 MSPs. The vertical axis represents the probability per unit skewness difference. The navy line is one in the absence of GWs. The red, orange and green lines correspond to the cases with $\dot{h} = 10^{-18}$, 3×10^{-19} and 10^{-19} s^{-1} respectively.

$K = 5.9$, which leads to $JB = 84.2$ and rejects the Gaussian with more than 99.9% confidence (for the interpretation of the $\log_{10}\dot{p}_0/p$ distribution, see [64]).

Thus, we study the effect of non-Gaussian of intrinsic $\log_{10}\dot{p}_0/p$ distribution. To do this, we utilize a generalized normal distribution given by

$$f(x) = \frac{\phi(y)}{\alpha - \kappa(x-\xi)}, \tag{3.10}$$

where $\phi(y)$ is the standard normal distribution and y is given by

$$y = \begin{cases} -\frac{1}{\kappa}\log\left[1 - \frac{\kappa(x-\xi)}{\alpha}\right] & (\kappa \neq 0) \\ \frac{x-\xi}{\alpha} & (\kappa = 0). \end{cases} \tag{3.11}$$

Here, ξ, α and κ are the location, scale and shape parameters, respectively, and the mean value μ, variance σ^2 and skewness S are expressed by these parameters,

$$\mu = \xi - \frac{\alpha}{\kappa}\left(e^{\kappa^2/2} - 1\right), \tag{3.12}$$

$$\sigma^2 = \frac{\alpha^2}{\kappa^2}e^{\kappa^2}\left(e^{\kappa^2} - 1\right), \tag{3.13}$$

$$S = \frac{3e^{\kappa^2} - e^{3\kappa^2} - 2}{(e^{\kappa^2} - 1)^{3/2}}\mathrm{sign}(\kappa). \tag{3.14}$$

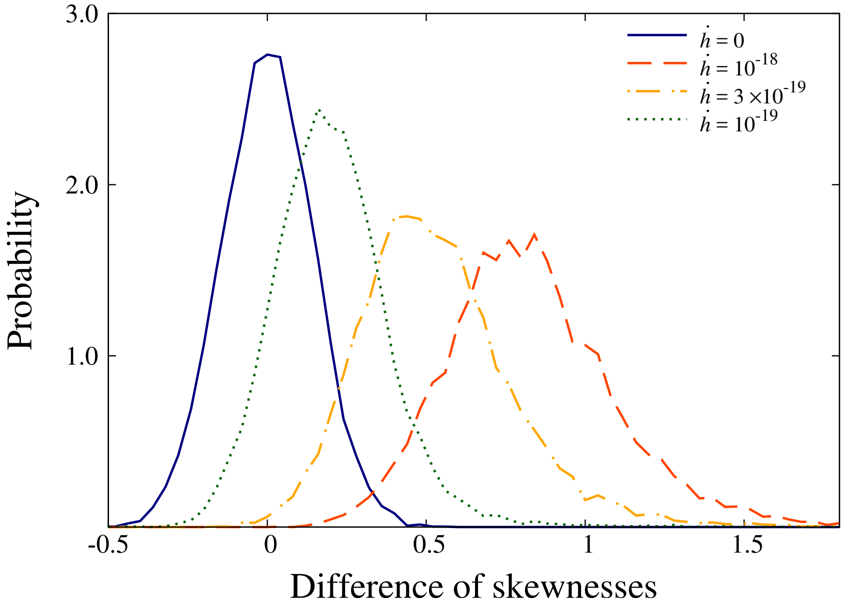

Figure 3.5: Probability distribution in the case of 1,000 MSPs. The line types are the same as Fig. 3.4.

Assuming that the intrinsic $\log_{10} \dot{p}_0/p$ distribution follows the generalized Gaussian distribution, we perform the same simulations as above with 3,000 MSPs. Fig. 3.7 shows the probability distribution of the skewness difference for the intrinsic skewness of -1.2, 0 (Gaussian) and 1.2. In the absence of GWs, the intrinsic skewness increases the standard deviation of the probability distribution of the skewness difference. On the other hand, in the presence of GWs ($\dot{h} = 10^{-18}$ s^{-1}), the intrinsic skewness not only widens but also shifts the probability distribution. As can be seen, a positive intrinsic skewness enhances the skewness difference. This is because the median of the intrinsic $\log_{10} \dot{p}_0/p$ distribution is smaller than the average and the number of MSPs with a small value of $\log_{10} \dot{p}_0/p$ increases for a fixed value of the average. Thus a positive intrinsic skewness, which is indicated by the known MSP samples, enhances the detectability of GWs. Contrastingly, a negative intrinsic skewness would reduce the detectability.

3.3.2 Precision of the determination of GW polarization angle

In the simulations shown above, we assumed the correct GW polarization angle is known. If we assume a wrong value of polarization angle, the skewness difference will be reduced. To see this, we perform simulations where the assumed polarization angle is deviated by 1°, 10° and 30° from the correct one. Fig. 3.8 shows the resultant probability distribution of the skewness difference in the case of 3,000 MSPs and $\dot{h} = 10^{-18}$ s^{-1}. From the figure, we see that, if the deviation is more than 10°, the skewness difference becomes significantly small. In a practical situation, we need to calculate the skewness differences varying the polarization angle while fixing the target position. Then, a polarization angle which gives the maximum skewness difference can be used as an estimate of the correct polarization angle. Fig. 3.9 shows the probability distribution of the deviation angle which

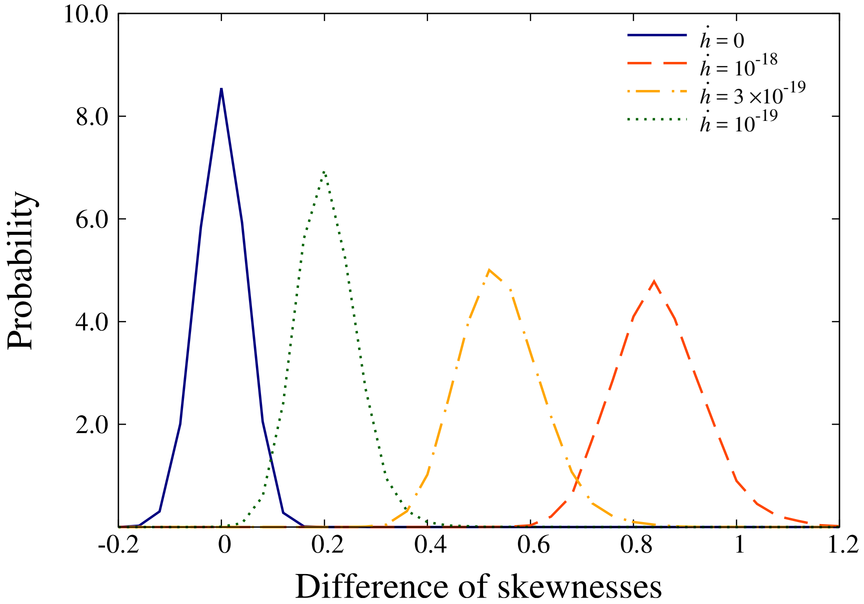

Figure 3.6: Probability distribution in the case of 10,000 MSPs. The line types are the same as Fig. 3.4.

gives the maximum skewness difference for 1,000, 3,000 and 10,000 MSPs and $\dot{h} = 10^{-18}$ s^{-1}. The mean is located at 0°, that is, the estimation is not biased. On the other hand, the standard deviation decreases as the number of MSPs increases: 42°, 32° and 19° (1σ) for 1,000, 3,000 and 10,000 MSPs, respectively. This can be regarded as the precision of determination of the polarization angle.

3.4 Discussion and Summary

In this paper, we evaluated the potential of the new detection method for ultra-low frequency GWs ($\lesssim 10^{-10}$ s^{-1}) from a single source proposed in [115]. This method is based on the statistics of observed spin-down rates of MSPs and GW signal appears as the difference of skewness between the spin-down rate distributions of two MSP groups which are constructed according to the MSP position in the sky. We applied the method to the mock samples of MSPs to estimate the sensitivity. As a result, we found that GWs of $\dot{h} = 3 \times 10^{-19}$ s^{-1} is detectable if we have 3,000 MSPs and the sensitivity is roughly proportional to the number of MSPs.

Let us see more details assuming that the GW source is a SMBH binary. The amplitudes of GWs for a circular binary are given by [46]

$$h_A = h_0 \left(\hat{u}_i \hat{u}_j - \hat{r}_i \hat{r}_j \right) e_{A,ij}, \tag{3.15}$$

where, h_0 is written by

$$h_0 = \frac{2\,(G\mathcal{M})^{5/3}(\pi f_{\rm GW})^{2/3}}{c^4 R}, \tag{3.16}$$

where G is the gravitational constant, c is the speed of light, $\mathcal{M} = (m_1 m_2)^{3/5}/(m_1 + m_2)^{1/5}$ is the chirp mass of the binary where m_1 and m_2 are the component masses, R is the distance to the source

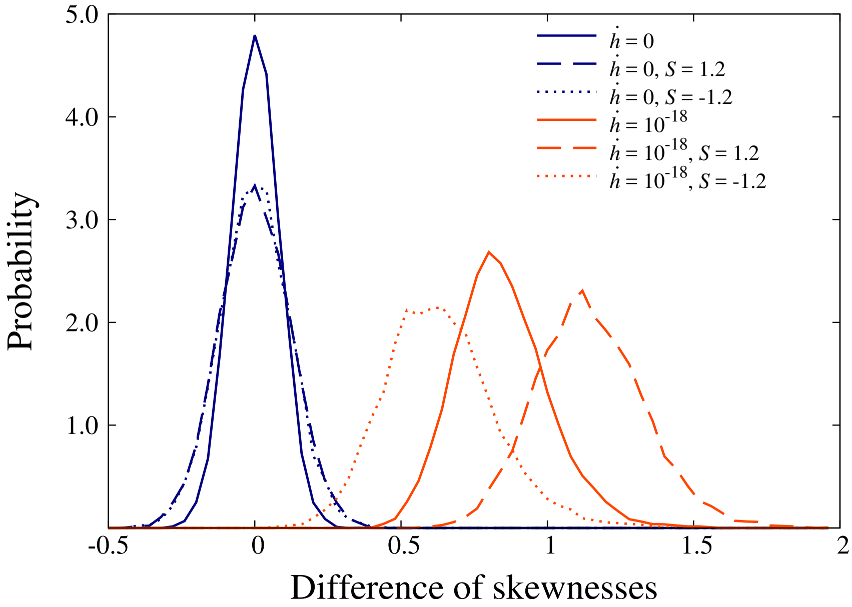

Figure 3.7: Probability distribution of the skewness difference for non-Gaussian intrinsic $\log_{10} \dot{p}_0/p$ distribution with 3,000 MSPs. The navy and red lines are ones with no GWs and $\dot{h} = 10^{-18}$ s^{-1}, respectively. The solid, dashed and dotted lines correspond to the cases with intrinsic skewness of 0 (Gaussian), 1.2 and -1.2, respectively.

and $f_{\rm GW}$ is the GW frequency. Here, $\hat{r}$ and $\hat{u} = \dot{\hat{r}}$ are the relative position and velocity vectors for the two black holes in the orbit described by the orbital phase ϕ which is the angle measured from $\hat{m}$. The time derivatives of the amplitudes is given by

$$\dot{h}_A = -\frac{1}{2}\dot{h}_0 \left(\hat{r}_i \hat{u}_j + \hat{u}_i \hat{r}_j\right) e_{A,ij}, \tag{3.17}$$

where $\dot{h}_0 = 2\pi f_{\rm GW} h_0$ and this value could be obtained from the current method. Further, the inclination ι, the orbital phase ϕ, and λ which is the angle between the line of nodes and $\alpha(\hat{\Omega}, \hat{p}, \theta) = 0$ are related as,

$$\left(1 + \cos^2 \iota\right) \sin 2\phi \cos 2\lambda - 2 \cos \iota \cos 2\phi \sin 2\lambda = 0. \tag{3.18}$$

Let us discuss more details of the pulsar term. As mentioned in section 3.2, we neglected the pulsar term in our simulations. This is because, if the pulsar term for many different pulsars has a random phase, it contributes to the noise and does not induce a bias so that the effect is reduced statistically for a large number of pulsars. Here, we evaluate a frequency range where this assumption is valid. Following [103], in the case the GW source is a SMBH binary, at the leading order, the GW frequency evolution due to radiation reaction is given by

$$\frac{df_{\rm GW}}{dt} = \frac{96}{5}\pi^{8/3}\left(\frac{G\mathcal{M}}{c^3}\right)^{5/3} f_{\rm GW}^{11/3}. \tag{3.19}$$

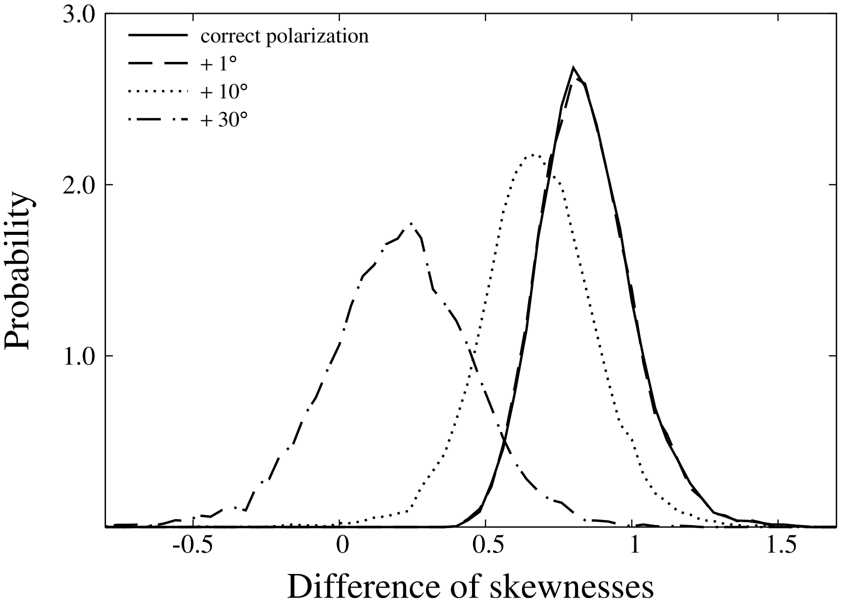

Figure 3.8: Probability distribution of the deviation angle which gives the maximum skewness difference in the case of 3,000 MSPs and $\dot{h} = 10^{-18}$ s^{-1}. The solid, dashed and dotted lines correspond to the deviation of 1°, 10° and 30°, respectively.

Then, the variation of the GW frequency during the pulse propagation time is

$$\begin{aligned}\Delta f_{\rm GW} &= \int_{t-\tau}^{t} \frac{df_{\rm GW}}{dt} dt \\ &\sim \frac{df_{\rm GW}}{dt}\tau \\ &\approx 6.3 \times 10^{-16} \mathcal{M}_{8.5}^{5/3}\, f_{100\ {\rm yr}}^{11/3}\, \tau_{5\ {\rm kpc}} \quad {\rm Hz}\ , \end{aligned} \tag{3.20}$$

where

$$\mathcal{M}_{8.5} = \frac{\mathcal{M}}{10^{8.5}\ M_\odot}\ , \tag{3.21}$$

$$f_{100\ {\rm yr}} = \frac{f_{\rm GW}}{(100\ {\rm yrs})^{-1}}\ , \tag{3.22}$$

$$\tau_{5\ {\rm kpc}} = \frac{\tau}{5\ {\rm kpc}/c\ {\rm sec}}\ . \tag{3.23}$$

This implies that the GW frequency changes little during the pulse propagation time for $\leq 10^{-10}$ Hz. The Earth and pulsar terms have the same frequency and their phase difference is given by $2\pi f_{\rm GW}\tau$. In order for the pulsar term of many different pulsars to have a random phase, the phase difference should be rather large, $2\pi f_{\rm GW}\tau \gtrsim \mathcal{O}(0.1)$ for a typical distance L. With $L \sim 5$ kpc in the SKA era and assuming that the angle between the directions to the pulsar and GW source is not so small, the phase difference becomes large for $\gtrsim 10^{-13}$ Hz. Thus, the pulsar term contributes to a random noise

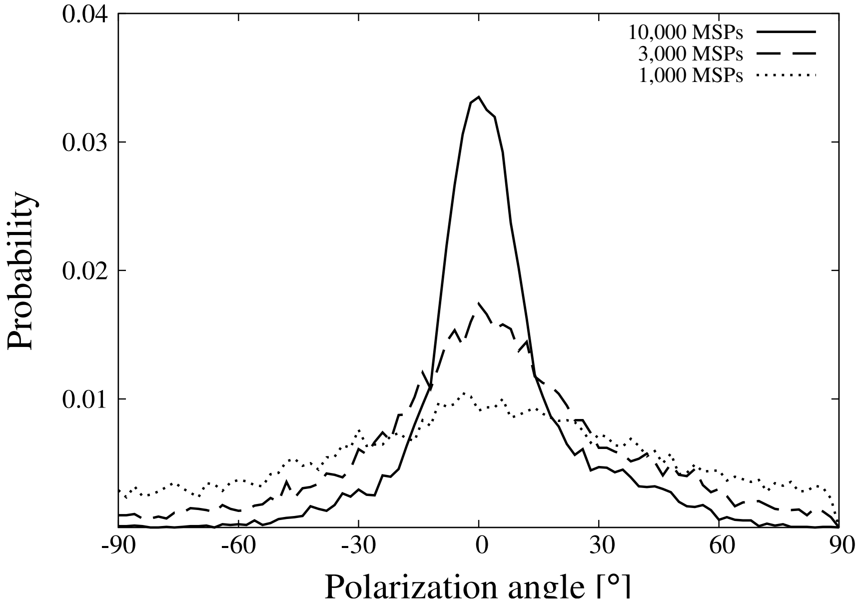

Figure 3.9: Precision of the determination of GW polarization angle in the case of $\dot{h} = 10^{-18}$ s^{-1}. The numbers of MSPs are 10,000 (solid), 3,000 (dashed) and 1,000 (dotted).

for $10^{-13} - 10^{-10}$ Hz. However, the effect of the pulsar term can not be neglected when the directions to the pulsar and GW source coincide, since $\tau = 0$ and the Earth and pulsar terms cancel out. This effect is known as the "surfing effect" [20] and important when $2\pi f_{\rm GW}\tau \ll 1$. This condition can be rewritten, using the angle from the pulsar direction to the GW source $\delta\zeta$,

$$1 - \cos(\delta\zeta) \ll \frac{c}{\pi f_{\rm GW} L}. \tag{3.24}$$

For $f_{\rm GW} \sim$ (a few $\times$ 100 yrs)$^{-1}$ $\approx$ 10^{-10} Hz and $L = 5$ kpc, the surfing effect is effective for an area of ~ 127.7 deg^2. Because this is only $\sim 0.3\%$ of the entire sky, this effect is not so significant for this configuration. For lower frequency, however, the effect is more significant and a "hole" appears around the GW source in the bias map (Fig. 3.1). Assuming the same typical distance of 5 kpc, this hole covers $\sim 10\%$, 50% and 80% of the sky for GW frequencies of $\sim 3.2 \times 10^{-12}$, 7.35×10^{-13} and 5.0×10^{-13} Hz, respectively. This would effectively reduce the number of MSPs contributing to the experiment and some reduction of the overall sensitivity.

For lower frequencies $\ll 10^{-13}$ Hz, the pulsar term can no longer be regarded as random noise. In this case, Eq. (2.48) can be written as

$$\begin{aligned} \Delta h_A(t, \hat{\Omega}) &= \dot{h}_A t \left(1 - e^{2i\pi f_{\rm GW}\tau}\right) \\ &\simeq \dot{h}_{Af^2} t \left(1 + \hat{\Omega}\cdot\hat{p}\right)^2, \end{aligned} \tag{3.25}$$

where $\dot{h}_{Af^2} = 2\pi^2 f_{\rm GW}^2 L^2/c^2 \; \dot{h}_A$. In the second step, we have used Taylor expansion assuming

$2\pi f_{\rm GW}\tau \ll 1$. Then the bias factor is given by

$$\alpha(\hat{\Omega},\hat{p}) = \frac{1}{2}\sum_{A=+,\times} \hat{p}^i\hat{p}^j e^A_{ij}\left(1+\hat{\Omega}\cdot\hat{p}\right)\ \dot{h}_{Af^2}. \tag{3.26}$$

Therefore, we may be able to extract the information of the degenerated value $f^2_{\rm GW}\dot{h}_A$ if the distance to the pulsar is measured precisely. Although the effect would be very small as it has additional factor $(f_{\rm GW}L/c)^2 \ll 1$, it would be a unique method to probe GWs at such low frequency. The quantitative estimation of sensitivity for such GWs should be studied elsewhere in the future.

One should also take into account the observational error in $\log_{10}(\dot{p}/p)$ which propagates to the uncertainty in the skewness difference. The uncertainty of ΔS can be estimated by considering error propagation and given by

$$\sigma^2_{\Delta S} = \sigma^2_{S_{\alpha+}} + \sigma^2_{S_{\alpha-}}, \tag{3.27}$$

where $\sigma_{S_{\alpha+(-)}}$ is uncertainty of the skewness in each region and given by

$$\begin{aligned}\sigma^2_{S_{\alpha+(-)}} &= \left(\frac{3}{N_{+(-)}\sigma^3_{+(-)}}\right)^2 \\ &\times \sum_i^{N_{+(-)}}\left(\left(\log_{10}\left(\frac{\dot{p}}{p}\right)_i - \mu_{+(-)}\right)^2 - \sigma^2_{+(-)}\right)^2 \sigma^2_{\log_{10}(\dot{p}/p)_i},\end{aligned} \tag{3.28}$$

where $\sigma^2_{\log_{10}(\dot{p}/p)_i}$ is uncertainty in $\log_{10}(\dot{p}/p)$, which is typically $\mathcal{O}(0.01)$. Taking $\sigma^2_{\log_{10}(\dot{p}/p)_i} = 0.01$ leads to the uncertainty in the skewness difference of $\sim 5\times10^{-2}$. This is much smaller than the value of skewness difference which we are interested here.

Let us consider some specific targets. A SMBH with mass of $4.0\times10^6 M_\odot$ is known to reside in Sgr A* and the possibility of the existence of another SMBH has been discussed (e.g. [90]). If they are forming a binary and emitting GWs of a frequency (100 yrs)$^{-1}$, for example, the mass of the second SMBH must be greater than $10^{15}M_\odot$ to be detectable by the current method with 3,000 MSPs. A more interesting target is M87 which has a SMBH with mass of $6.6\times10^9 M_\odot$. Constraints on the amplitude of GWs emitted by a milli-pc scale SMBH binary in M87 and other galaxies in the PTA frequency bands has been already studied [102]. While, a possibility of another SMBH outside the AGN has been indicated also for M87 [14] and [115] discussed GWs from such a potential pc-scale SMBH binary. There, we found that $\dot{h}$ can be as large as 10^{-18} s^{-1} when the second SMBH mass is $6.6\times10^8 M_\odot$, the eccentricity of the orbit is greater than 0.8 and the black holes are located near the perihelion.

Acknowledgements

I have been supported by many people to get a Ph.D. I have worked in a blessed environment and had a lot of great opportunities.

First, I would like to express my deepest gratitude to my supervisor, Associate Professor Keitaro Takahashi at Kumamoto University. I couldn't accomplish my studies without his support and instruction. He has always been willing to guide and discuss with me, and gave me numerous opportunities such as to attend conferences and study abroad.

I also have been supported by people at CSIRO in Australia when I visited and stayed there. I have special thanks for my co-supervisor Dr. George Hobbs. He worked and discussed with me as much as possible even thought my ability in English is poor.

I also would like to thank Japanese collaborators, including Dr. Sachiko Kuroyanagi who has worked with me on the cosmic string project.

It was great that I have been attached to the cosmology group in Kumamoto University. I have had wonderful colleagues; Shinsuke Ideguchi, Hayato Shimabukuro, Shintaro Yoshiura, Yoshimitsu Miyashita, Hiroki Kumamoto, Kenji Kubota, Shinnosuke Hisano, Shoichiro Tanaka, Taisuke Nakashima, Masaki Suzuki, Tomonosuke Kikunaga, Yuta Shiohira and Akira Kuchinomachi. Thanks to them I could spend an enjoyable university life.

Finally and most importantly, thank you to my family for their understanding on my decision to go the doctoral course and financial support.

Bibliography

[1] Abbott, B. P., Abbott, R., Adhikari, R., et al., 2009, 09, Phys. Rev. D, 80, 062002

[2] Abbott, B. P., Abbott, R., Abbott, T. D., et al., 2016, Phys. Rev. D, 93, 122008

[3] Abbott, B. P., Abbott, R., Abbott, T. D., et al. 2016, Phys. Rev. Lett., 116, 061102

[4] Abbott, B. P., et al. , 2016, Phys. Rev. Lett, 116. 13

[5] Abbott, B. P., Abbott, R., Abbott, T. D., et al. 2018, Phys. Rev. D, 97, 102002

[6] Abbott, B. P., Abbott, R., Abbott, T. D., et al. 2017, Phys. Rev. Lett., 119, 161101

[7] Abolfathi B. et al. 2018, ApJS, 235, 42

[8] P. A. R. Ade et al. [Planck Collaboration], Astron. Astrophys. **571**, A25 (2014)

[9] Aggarwa,l K., et al., 2019, ApJ, 880, 116

[10] Anholm M., Ballmer S., Creighton J. D. E., Price L. R., Xavier S., 2009, Phys. Rev. D, 79, 084030

[11] Arzoumanian, Z., Baker, P. T., Brazier, A., et al. 2018, ApJ, 859, 47

[12] Babak, S., et al., 2016, MNRAS, 455, 1665

[13] Banerji M. et al. 2010, MNRAS, 406, 342

[14] Batcheldor D., Robinson A., Axon D. J., Perlman E. S., Merritt D., 2010 ApJ, 717, L6

[15] Berti E. et al. 2015, Class. Quantum Gravity, 32, 3001

[16] Bertotti, B., Carr B. J. & Rees M. J., 1983, MNRAS, 243, 945

[17] Bethapudi S., Desai S., 2018, A&C, 23, 15

[18] Bilous A. et al. 2016, A & A, 591, 134

[19] Blanco-Pillado J. J. , Olum K. D., 1999, Phys. Rev. D 59, 063508

[20] Braginsky, V. B., Kardashev, N. S., Polnarev, A. G. & Noviko, I. D., 1990, Nuovo Cimento B, 105, 1141

[21] Champion, D. J. et al, 2010, ApJ, 720, L201

[22] D. F. Chernoff, arXiv:0908.4077 [astro-ph.CO].

[23] D. F. Chernoff and S. H. Henry Tye, doi:10.1142/9789814678506_0007

[24] D. F. Chernoff and S.-H. H. Tye, JCAP **1805**, no. 05, 002 (2018) doi:10.1088/1475-7516/2018/05/002 [arXiv:1712.05060 [astro-ph.CO]].

[25] Coles W., Hobbs G., Champion D. J., Manchester R. N., Verbiest J. P. W., 2011, MNRAS, 418, 561

[26] Collister A. A. & Lahav O. 2004, PASP, 116, 345

[27] Condon J. J., Cotton W. D., Greisen E. W., Yin Q. F., Perley R. A., Taylor G. B. & Broderick J. J. 1998, Astron. J., 8065, 1693

[28] Connor L. & van Leeuwen J. 2018, AJ, 156, 256

[29] Cordes J. M. et al. 2006, ApJ, 637, 446

[30] Cybenko G. 1989, Mathematics of control. Signals and Systems, Vol. 2 pp. 303-314

[31] Dai S., Johnston S., Bell M. E., Coles W. A., Hobbs G., Ekers R. D & Lenc E. 2016, MNRAS, 462, 3115

[32] Damour, T. & Taylor, J. H., 1991, ApJ, 366, 501

[33] Damour T., & Vilenkin A., 2000, Phys. Rev. Lett. 85, 3761

[34] T. Damour and A. Vilenkin, Phys. Rev. D **64**, 064008 (2001)

[35] de Gasperin F., Intema H. T. & Frail D. A. 2018, MNRAS, 474, 5008

[36] Detweiler S., 1979, ApJ, 234, 1100

[37] Dvali G. & Vilenkin A., 2004, J. Cosmol. Astropart. Phys., 03

[38] Eatough R. P. et al. 2010, MNARS, 407, 2443

[39] Edwards R. T., Hobbs G. B., Manchester R. N., 2006, MNRAS, 372, 1549

[40] Flesch E. 2015, PASA, 32, 10

[41] Folkes S. R., Lahav O. & Maddox S. J. 1996, MNRAS, 283, 651

[42] Foster R. S., Backer D. C., 1990, ApJ, 361, 300

[43] Frail D. A. et al. 2018, MNRAS, 475, 942

[44] George D. & Huerta E. A. 2018, Phys.Lett.B, 778, 64

[45] Goldreich P. & Julian W. H., 1969, ApJ, 157, 869

[46] Gopakumar, A. & Iyer, B. R., 2002, Phys. Rev. D, 65, 084011

[47] Guo P., Fuqing D., Wang P., Yao Y. & Xin X. 2017, preprint (arXiv:1711.10339)

[48] Han J. L., Ferriere K. & Manchester R. N. 2004, ApJ, 610, 820

[49] Harding, A., K. 2013, Frontier of Physics, 8, 679

[50] Hellings R. W., Downs G. S., 1983, ApJL, 265, L39

[51] Hewish A., Bell S. J., Pilkington J. D. H., Scott P. F. & Collins R. A. 1968, Nature, 217, 709

[52] Hobbs G. B., Edwards R. T., Manchester R. N., 2006, MNRAS, 369, 655

[53] Hornik K. 1991, Neural Networks, Vol. 4, pp 251 - 257

[54] Intema H. T., Jagannathan P., Mooley K. P. & Frail D. A. 2017, A&A, 598, A78

[55] Ivezić, Ž., Menou, K., Knapp, G. R., et al. 2002, AJ, 124, 2364

[56] M. G. Jackson, N. T. Jones and J. Polchinski, JHEP **0510**, 013 (2005) doi:10.1088/1126-6708/2005/10/013 [hep-th/0405229].

[57] Jankowski, F., van Straten, W., Keane, E. F., et al. 2018, MNRAS, 473, 4436

[58] Jenet F. et al. 2009, preprint (arXiv:0909.1058)

[59] Jenet, F., A,. & Romano, J., D. 2015, AmJPh, 83, 635

[60] N. T. Jones, H. Stoica and S. H. H. Tye, JHEP **0207**, 051 (2002) doi:10.1088/1126-6708/2002/07/051 [hep-th/0203163].

[61] Jones N. T., Stoica T. & Tye S. H. H., 2003, Phys. Lett. B 563, 6

[62] Keane E. F. et al. 2015, preprint (arXiv:1501.00056)

[63] Kibble T. W. B., 1976, J. Phys. A, 9, 1387

[64] Kiziltan, B. & Thorsett, S. E., 2010, ApJ, 715, 335

[65] Kopeikin, S. M., 1997, Phys. Rev. D, 56, 4455

[66] Kopeikin, S. M., 1999, MNRAS, 305, 563

[67] Kopeikin, S. M. & Potapov, V. A., 1999, MNRAS, 355, 395

[68] Kramer M., Champion D. J., 2013, Class. Quantum Gravity, 30, 4009

[69] Kramer M., Stapper B., 2015, preprint (arXiv:1507.04423)

[70] Kramer M. et al. 2006, Science, 314, 97

[71] Kuroyanagi S., Miyamoto K., Sekiguchi T., Takahashi K., Silk J., 2012, Phys. Rev. D, 86, no. 2, 023503

[72] Kuroyanagi S., Miyamoto K., Sekiguchi T., Takahashi K., Silk J., 2013, Phys. Rev. D, 87, no. 2, 023522

[73] S. Kuroyanagi, K. Takahashi, N. Yonemaru and H. Kumamoto, Phys. Rev. D **95**, no. 4, 043531 (2017)

[74] Lattimer J. M. & Prakash M. 2004, Science, 304, 536

[75] Lentati, L., Shannon, R. M., Coles, W. A., et al. 2016, MNRAS, 458, 2161

[76] Lentati, L., Taylor, S. R., Mingarelli, C. M. F., et al. 2015, MNRAS, 453, 2576

[77] Levin L., et al., 2018, Pulsar Astrophysics the Next Fifty Years, 171, IAUS..337

[78] Lodarto, G., Nayakshin, S., King, A. R. & Pringle, J. E., 2009, MNRAS, 398, 1392

[79] Lynch, R. S., Boyles, J., Ransom, S. M., et al. 2013, ApJ, 763, 81

[80] Maan Y. et al. 2018, ApJ, 864, 16

[81] Manchester R. N., Hobbs G. B., Teoh A. & Hobbs M. 2005, AJ, 129, 1993

[82] Manchester R. N. et al. 2001, MNRAS, 328, 17

[83] Manchester R. N. et al., 2012, PASA, 30, 17

[84] Milosavljević, M. & Merritt, D., 2001, ApJ, 563, 34

[85] Moore C. J., Cole R. H., Berry C. P. L., 2015, CQGra, 32, 015014

[86] Morello V. et al. 2014, MNRAS, 443, 1651

[87] Murphy T. et al. 2017, PASA, 34, 20

[88] Naim A., Lahav O., Sorde L. Jr. & Storrie-Lombardi M. C. 1995, MNRAS, 275, 567

[89] Nice, D. J. & Taylor, J. H., ApJ, 441, 429

[90] Oka, T., Mizuno, R., Miura, K. & Tatekawa, S., 2016, ApJ, 816, L7

[91] Olmez S., Mandic V. and Siemens X., Phys. Rev. D **81**, 104028 (2010) doi:10.1103/PhysRevD.81.104028 [arXiv:1004.0890 [astro-ph.CO]].

[92] Phinney, E. S., 1993, ASPC, 50, 141

[93] Planck Collaboration, Ade, P. A. R., Aghanim, N., et al., 2014, A&A, 571, A25

[94] Planck Collaboration, Ade, P. A. R., Aghanim, N., et al., 2016, A&A, 594, A13

[95] Porayko N. K., Zhu X.-J., et al. in prep

[96] Potapov, V. A., Ilyasov, Yu. P., Oreshko, V. V. & Rodin, A. E., 2003, Astron. Lett., 29, 241

[97] Rong, J., Xiao, N. & Tan, L., 1999, Science in China Series, A-Math, 42, 444

[98] Rumelhart D. E., Hinton G. E. & Williams R. J. 1986, Nature, 323, 533

[99] Samui S. & Samui Pal S. 2017, New Astron., 51, 169

[100] Sarangi S.& Tye S. H. H., 2002, Phys. Lett. B 536, 185

[101] Schnizeler D. H. F. M. 2012, MNRAS, 427, 664

[102] Schutz, K. & Ma, C., 2016, MNRAS, 459, 1737

[103] Sesana, A., & Vecchio, A., 2010, Phys. Rev. D, 81, 104008

[104] Shannon R. M. et al., 2015, Science, 349, 1522

[105] Shimabukuro H. & Semelin B. 2017, MNARS, 468, 3869

[106] Shklovskii, I. S., 1970, Soviet Astronomy, 13, 562

[107] Siemens X., et al., 2006, Phys. Rev. D 73, 105001

[108] Smits, R., Kramer, M., Stappers, B., et al. 2009, A&A,, 493, 1161

[109] Storrie-Lombardi M. C., Lahav O., Sorde L. Jr. & Storrie-Lombardi L. J. 1992, MNRAS, 259, 8

[110] Vanzella E., Cristiani S., Fontana, A. et al. 2004, A&A, 423, 761

[111] Vilenkin A. & Shellard E. P. S., 1994, "Cosmic Strings and Other Topological Defects", Cambridge University Press, Cambridge, England

[112] Wang, H., Zhu, W., Guo, P., et al. 2019, Science China Physics, Mechanics, and Astronomy, 62, 959507

[113] Wang J.-B., Hobbs G. B., Coles W. et al., 2015, MNRAS, 446, 1657

[114] Weisberg, J., M., & Taylor, J., H. 2005, ASPC, 328, 25

[115] Yonemaru, N., Kumamoto, H., Kuroyanagi, S., Takahashi, K. & Silk, J., 2016, PASJ, 68, 106

[116] Zhu, W. W., Berndsen, A., Madsen, E. C., et al. 2014, ApJ, 781, 117

[117] Zhu X.-J., Hobbs G. B. et al., 2014, MNRAS, 444, 3709